Università degli Studi di Padova

Dipartimento di Ingegneria Industriale
Corso di Laurea Magistrale in Ingegneria Energetica

Reconstruction of the two-dimensional energy flux profile of a particle beam using thermographic measurements

---

Relatore:
Prof. Paolo Bettini

Laureanda:
Giorgia Rossi

Correlatori:
Dr. Rita S. Delogu
Dr. Gianluigi Serianni

Anno accademico 2015-2016

Abstract

The ITER tokamak is an international project, with the aim of proving the possibility to produce energy by nuclear fusion of deuterium and tritium nuclei in a reactor scale. In order to reach the necessary temperature for fusion, additional heating systems are required, like the injection of a neutral beam. To study the neutral particle beam, a diagnostic calorimeter (STRIKE) made of 1D-CFC tiles has been developed. The beam impinges on the calorimeter and thermal cameras provide images of the temperature profile on the rear side of the tiles.

A small scale version of STRIKE (mini-STRIKE) has been employed to investigate the properties of the negative ion beam test stand of the neutral beam injectors of the LHD experiment (NIFS). The thermal camera images of the tiles temperature profiles represent the experimental data analyzed in this thesis.

This thesis presents a method to reconstruct the energy flux profile impinging on the front side of the tile that produced the given temperature profile recorded by the thermal camera. This method is based on the transfer function and lies on the assumptions that the material is linear and the effect of radiation can be neglected.

In Chapter 1 an introduction to nuclear fusion and ITER experiment is given. Furthermore, the need of external heating systems is explained, focusing on NBI and LHD ion source.

Chapter 2 presents the PRIMA test facility, the calorimeter SPIDER design and the mathematical model of the method.

Chapter 3 explains in detail the method and the test made on simulated data.

In Chapter 4 the method is applied and optimized for the experimental data from the NIFS experiment. Furthermore the results of the data analysis are shown.

Conclusions and further development are finally presented in Chapter 5.

CONTENTS

LIST OF FIGURES

1 INTRODUCTION

1.1 NUCLEAR FUSION FOR ENERGY

The search for new clean and sustainable sources that could meet the rapidly growing global energy demand is one of the biggest challenges that humankind will have to face in next decades. Fossil fuels like coal, oil and gas are rapidly depleting, and their combustion generates serious environmental consequences, such as the greenhouse effect. An important worldwide research field which could provide a solution to this problem is nuclear fusion, in which two light nuclei can fuse together, forming a heavier nucleus, if they are given enough energy to overcome the Coulomb repulsion.

The research on nuclear fusion focuses on the fusion of deuterium and tritium nuclei:

$$^{2}D + {}^{3}T \rightarrow {}^{4}He\ (3.5\ MeV) + n\ (14.1\ MeV) \tag{1.1}$$

This reaction shows the highest cross section compared to other promising fusion reactions (see Fig. 1). Moreover, it has a lower activation energy than the others, and a temperature of $15\ keV (\approx 10^{8}\ K)$ is high enough for fusion to happen with a sufficiently high cross section [18].

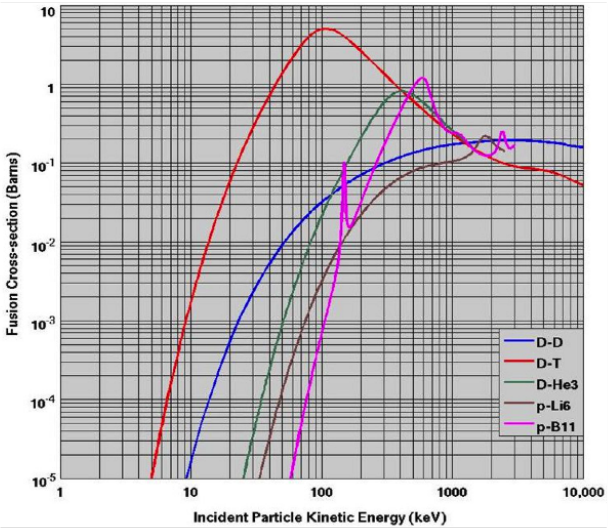

Figure 1: Cross sections of various fusion reactions as a function of the kinetic energy of an incident deuterium atom or proton on a stationary target [18]

While deuterium is available in nature (for example, it can be extracted from sea water, in which it is present in a concentration of 30 mg/l), tritium is not present in a large quantity in nature: it is not a stable isotope and has an half-life of 12.3 years. It is then necessary to create these nuclei inside the reactor, by means of the following reaction:

$$n + {}^{6}Li \rightarrow {}^{4}He\ (2.05\ MeV) + {}^{3}T\ (2.75\ MeV) \tag{1.2}$$

Lithium is widely available in the Earth's crust, as well as in the oceans.

The reaction products are neutrons with an energy of $14.1\,MeV$ and helium-4 nuclei with an energy of $3.5\,MeV$, as Eq.1.1 shows; as the reaction rate needs to be high enough to produce a certain amount of energy, high temperatures ($\sim 10\,keV$) have to be achieved. At these temperatures, the energy is sufficiently high to ionize the atoms and the matter is in a plasma state, i.e., a high-temperature, partly or fully ionized, quasi-neutral gas of charged particles (positive nuclei and negative electrons), showing a collective behavior. The main goal to achieve a nuclear fusion reaction in laboratory is to reach the balance between the energy input, represented by the energy deposited to the plasma by α particles, produced by fusion reactions and by additional heating systems, and energy losses, due to transport and radiation. The energy losses can be described by a parameter called energy confinement time τ_E:

$$\tau_E = \frac{W}{P_L} \tag{1.3}$$

where W is the total energy stored in the fusion plasma and P_L is the total power loss due to transport phenomena. In order to produce more power by nuclear fusion than the power necessary to heat the plasma, some requirements have to be fulfilled. The Lawson criterion (Eq.1.4) establishes a threshold over which this condition occurs:

$$n\tau_E \geq \frac{12 k_B T}{E_\alpha \langle \sigma v \rangle} \tag{1.4}$$

where n, τ_E, T, E_α and $\langle \sigma v \rangle$ represent the plasma density, the energy confinement time, the plasma temperature, the energy of the alpha particle released by the fusion reaction (for the D-T reaction in Eq.1.1 this energy corresponds to 3.5 MeV) and the reaction rate coefficient. For the D-T reaction of Eq.1.1, at the required temperature ($T \approx 15\,keV$), the Lawson criterion becomes:

$$n\tau_E T \geq 1.5 \cdot 10^{21}\ m^{-3} keV\, s\ . \tag{1.5}$$

There are two possible techniques to achieve a high $n\tau_E$ product. In inertial confinement, a laser is used to compress a mixture of deuterium and tritium, so that a very high density is achieved for a very short time. The other possible way is to increase the energy confinement time by magnetically confining the plasma, which is composed of charged particles and thus sensitive to magnetic fields; closed magnetic field lines give the highest confinement. Toroidal machines were built around the world to test confinement and plasma production with different magnetic topologies: the tokamak is the most used, as well as the most promising.

One of the advantages of this technology is its intrinsic safety, when compared to nuclear fission:

- There is no possibility of a runaway reaction, as the ignition and sustainment of the plasma require so much effort that any changes in the operating conditions, for example due to a black out or other glitches, would simply stop sustaining the reactions, which would then stop as well. The working pressure is also much lower than the atmospheric pressure, so that in case of leakage, air enters the system and stops the reactions, preventing any risk of explosion.

- The fuel is not highly radioactive, only tritium is radioactive but just for around 12 years.

- Radioactive pollution is still present because the materials are activated by high energy neutrons, but the lifetime of the radioactive waste is hundreds of years instead of thousands of years as for nuclear fission.

1.2 ITER PROJECT

The ITER project started at the end of 1985 thanks to an agreement between the European Union, the Soviet Union, the United States and Japan, with the aim of studying and developing fusion energy for peaceful purposes. Other signatories joined the project later on, such as the Republic of China and the Republic of Korea in 2003 and India in 2005. The ITER agreement was signed in 2006 and the location selected for building the reactor was Cadarache, in southern France [16].

ITER is a toroidal machine based on tokamak magnetic confinement technology with the aim of proving the feasibility of using nuclear fusion for energy production. The main goal of ITER is to achieve a positive balance between the produced fusion power and the input power. The fuel will be a mixture of deuterium and tritium, which are heated to a temperature of $10\,keV$ (~ 150 million °C) to form the plasma. The plasma confinement magnetic field will be generated by superconducting coils wound around the vessel, along with a contribution by the current driven in the plasma, whose other aim is to heat the plasma itself. The reactor is expected to produce a fusion power of $\sim 500\,W$ with a duration up to 500 s and a gain factor of at least 10 (i.e. the ratio between the fusion power produced by the reactor and the input auxiliary power required to sustain the reaction itself). In order to achieve the high temperatures required to start the fusion reactions, ITER will be provided with some external heating systems, since ohmic heating through plasma current is not enough to reach the required input heating power ($\sim 50\,MW$). The heating provided by ohmic effect is $\propto I_p^2 \cdot R_p$, where I_p is the plasma current and R_p is the plasma resistance: since plasma resistance decreases as temperature grows, ohmic heating becomes less effective at high temperatures.

The high conductivity may be somewhat surprising since the number density of electrons (i.e., the number of charge carriers) is typically eight orders of magnitude smaller than that found in a good electrical conductor such as copper. Even so, the electrical conductivity of a fusion plasma is about 40 times larger than that of copper. The reason is associated with the fact that at high temperatures and low densities there are rarely any Coulomb collisions between electrons and ions and thus there is very little resistance to the flow of current [13].

The ITER main parameters are summarized in Tab 1.

ITER specifications	**Value**
Fusion power	500 MW
Fusion power gain (Q)	≥ 10
Pulse duration	3600 s
Type of plasma	D-T
Plasma major radius	6.2 m
Plasma minor radius	2.0 m
Plasma current	15 MA
Toroidal field at 6.2 m radius	5.3 T
Installed auxiliary heating:	
– by neutral beam injection	33 MW
– by radio-frequency waves	40 MW
Plasma volume	830 m^3
Plasma surface area	680 m^2
Machine height	26 m
Machine diameter	29 m

Table 1: ITER parameters and operational capabilities [16]

1.3 NEUTRAL BEAM HEATING

As the previous section mentioned, external heating systems are required in order to reach the fusion temperature. These systems introduce a non-inductive current drive in the torus, which makes continuous operation possible, sustaining the poloidal field and enhancing the plasma confinement.

The plasma can be heated by two different means, as shown in Fig.2: high-frequency electromagnetic waves and neutral beam injection.

The electromagnetic waves are generated outside the torus, then coupled into the plasma. Propagating inside the plasma, the RF waves release their energy to the charged plasma particles. The two resonance frequencies ω which will be used for the ITER heating system are [16]:

- the ion cyclotron resonance, $\omega_i = \frac{eB}{m_i}$, where e is the electron charge, B the magnetic field and m_i the ion mass. This frequency is in the range of 40-55 MHz;
- the electron cyclotron resonance, $\omega_e = \frac{eB}{m_e}$, where m_e is the electron mass. The electron cyclotron frequency in ITER is 170 GHz.

The second heating method is injecting high-energy atoms (hydrogen or deuterium) into the magnetically confined plasma.

These particles have to be neutral to penetrate the magnetic field in order to reach the plasma and, once there, become ionized.

In order to have a sufficient penetration depth of the beam in the plasma, the beam energy has to be at least in the order of hundreds of keV [18]. The beam energy for ITER is required to be about 1 MeV [12], in order to ensure a high efficiency non-inductive current drive of high-energy particles (the current drive efficiency increases with particle energy) and to supply 33 MW of heating power from two heating beamlines.

The main components of a Neutral Beam Injector (NBI) are displayed in Fig. 3. On the right there is the beam source, where hydrogen or deuterium ions are created in a plasma and then accelerated to the desired energy by an extractor/accelerator system. The ion beam then goes to the *drift region* (that is the region just downstream the accelerator system), where a fraction of

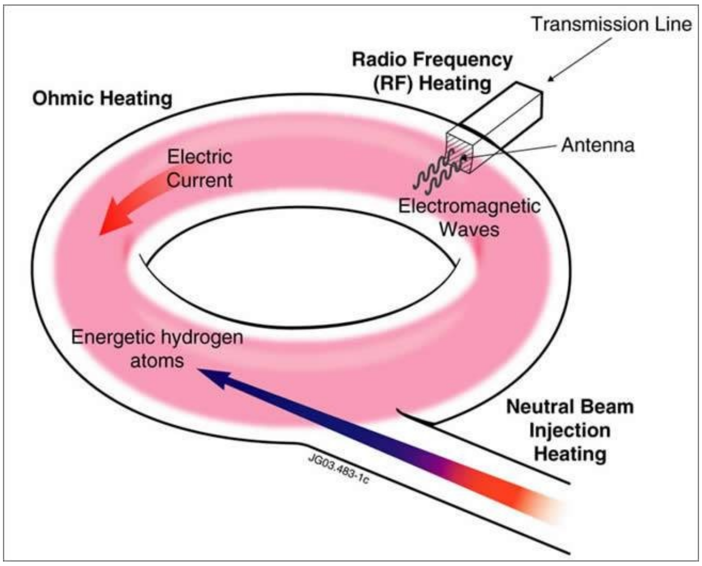

Figure 2: Sketch of the ohmic heating, the Radio Frequency (RF) heating and the neutral beam injection heating in a tokamak [16]

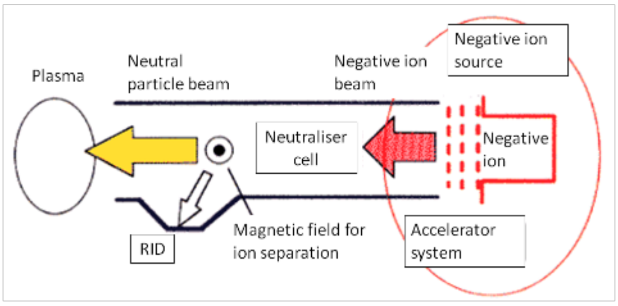

Figure 3: Sketch of the Neutral Beam Injector for the JT-60U tokamak (Japan) [17]. The main components are the negative ion source (on the right), where ions are created and accelerated by an extractor/accelerator system; the drift region downstream the source, where particles are neutralized, and the Residual Ion Dump (RID), which collects the residual ions deflected by a magnetic field (or electrostatic field in the case of ITER), before the beam reaches the plasma in the tokamak.

the accelerated ions is neutralized by means of collisions with the dedicated gas cell. A magnetic or electrostatic field (the latter is the case for ITER) is placed after the neutralizer cell, in order to deflect the non-neutralized ions, which are dumped by means of the Residual Ion Dump (RID) before reaching the plasma in the tokamak.

1.4 HYDROGEN ION SOURCE

In a neutral beam system, the ion sources provide a flux of ions to the apertures in the first grid of an electrostatic accelerator. Ions passing through the apertures are accelerated to the required energy, then neutralized to produce the neutral beam. Neutral beams can be injected through the magnetic confinement fields and into the confined plasma where they are easily ionized, and then trapped inside the confinement field. They then

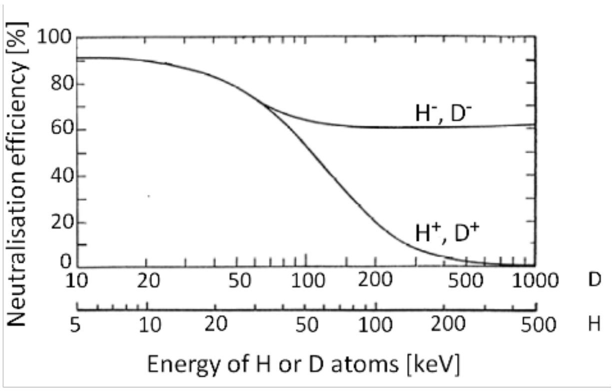

Figure 4: Neutralization efficiency of positive and negative ions as a function of their kinetic energy [18]

give their energy to the plasma via collisions. It is important that the injected beam neither pollutes nor dilutes the plasma in the fusion device.

The beam energy has to be significantly above the energy of the plasma particles it has to heat, and the beam has to penetrate sufficiently into the plasma in order that it deposits its energy in the appropriate part of the plasma. To heat the plasma, energy must be provided faster than it is being lost. As energy is lost more slowly from the centre of the fusion device than from the edge, the beam should deposit its energy nearer the centre than the edge. As the cross sections for ionizing the neutral beam decrease with the beam energy, a higher energy beam penetrates deeper into any given plasma [14].

Both accelerated positive or negative hydrogen ions can be neutralized by collisions with hydrogen molecules, but the efficiency is different for positive and negative beams, as shown in Fig. 4 at energies higher than 100 keV, the neutralization efficiency for positive ions decreases rapidly to almost zero. Negative ion beams instead have a neutralization efficiency of 60 % even at higher energies, because of the low binding energy of the electron (0.75 eV). For this reason, the negative ion source is the reference source for the ITER NBI system.

The great advantage of negative ions is that they can be easily neutralized. Unfortunately, this is also the case throughout the accelerator, while the ions are being accelerated, but when neutralization occurs in the accelerator, it is called stripping. Stripping produces neutrals from ions that have passed through only part of the optics of the accelerator, and only part of the accelerator. Therefore, the neutrals produced have less than the full energy and they usually have a high divergence compared to ions passing through the complete acceleration process. In addition, stripping produces free electrons that are accelerated through the remaining part of the accelerator. Neither the (divergent) partial energy neutrals nor the accelerated electrons can form a useful neutral beam, so stripping simply leads to losses of part of the extracted negative ions and power loading of the accelerator or other components of the neutral beam injector. Moreover, the accelerated negative ion current density has to be achieved at a low source pressure as it possible [14].

In order to enhance the H^- current density, Cesium (Cs) vapor is seeded in the ion sources and this have also the advantage to obtain low beam divergences.

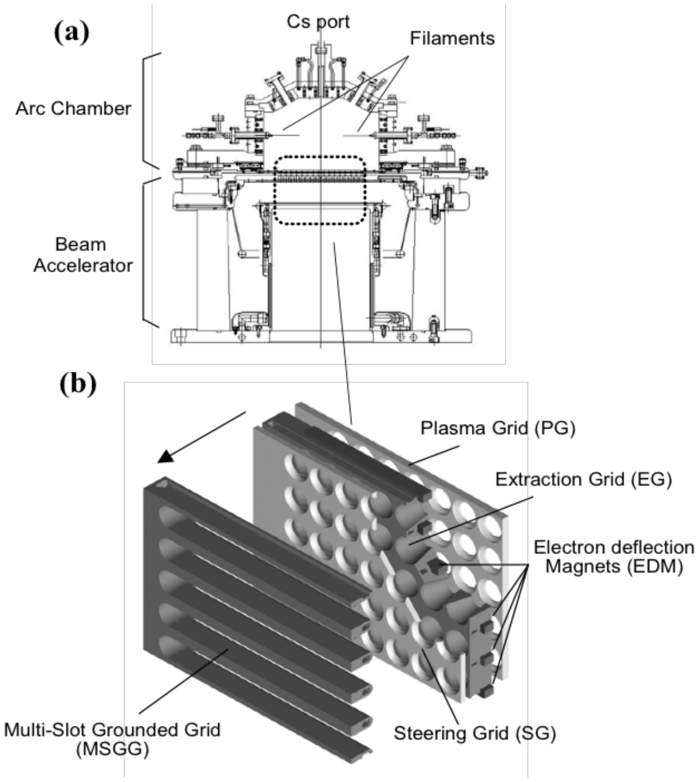

Figure 5: (a) Cross-sectional view of the beam line 1 ion source. (b) Layout of the accelerator with multi-slot grounded grid [27]

1.4.1 LHD source

In case of plasma confinement devices consisting of superconducting coils, such as the Large Helical Device (LHD), the beam injection ports are narrow and the drift tubes are long because of the thermal insulating structure for the coils. Low divergence character of neutral beams based on Cs seeded negative ion sources matched well to the condition of injection ports and the tubes. Beam parameters required for LHD-NBI are 180 keV for maximum injection energy, 5 MW of the maximum port-through power for 10 sec of pulse duration. The beam divergent angle is less than 10 mrad.

A cross-sectional schematic view of the negative ion source for LHD-NBI beam line 1 is shown in Fig. 5. The ion source is divided into two parts by an electrode called the plasma grid PG . One is an arc chamber and another is a beam accelerator. The arc chamber has a hexagonal cross section to avoid unnecessary connections of magnetic fields induced by the cusp and filter magnets. In order to enhance the production of H ions cesium vapor is introduced to the chamber from the backplate side via three cesium lines, and the vapor is spread to the sidewalls by the end nozzles [29].

The accelerator is composed by four grids, which are a PG, extraction grid EG , steering grid SG , and MSGG. Hydrogen negative ions produced inside the arc chamber are extracted by electric field called the extraction field applied between the PG and EG. The extracted H beam is accelerated by the field between the SG and MSGG; the field is called the acceleration field. The EG and SG are electrically connected. The configuration of those four grids is shown in the lower part of Fig. 5. The PG is made of a molybdenum plate with thickness of 4 mm and the grid is not cooled by water.

Inside the EG permanent magnets, which are called the electron deflection magnets EDMs, are installed to deflect the extracted electron and to avoid electron penetration into the acceleration gap. The grid is cooled by water and is made of oxygen free copper OFC. The MSGG has a large opening and the back-streaming positive ions come from the beam plasma region. The back-stream intersects the inter-aperture area of the SG along the slot direction. The SG should have resistance to the heat load and sputtering due to the back-streaming positive ions. Molybdenum, therefore, is chosen as the SG material. The grounded grid is exposed to the highest beam heat load of all the grids in the single-stage acceleration, and this is one of the reasons to change the grid apertures to slots. A single slot of the MSGG corresponds to a single row of apertures in the previous MAGG (Multi Aperture Grounded Grid). The long side of the slot is oriented in the direction of beam deflection by the EDM field, because the beam aberrations are larger than the other directions. The grid is made of OFC and consists of the water-cooled channels [29].

1.4.2 Beam physics

The optic properties of the beamlets and thus also of the complete beam depend on the space charge distribution and on the electric and magnetic fields in the extraction system.

An important parameter to describe the beam optics is the **perveance** Π, defined by the following formula [19]:

$$\Pi = \frac{I_{ext}}{V_{ext}^{3/2}} \tag{1.6}$$

where I_{ext} is the extracted current and V_{ext} is the extraction voltage.

It is also possible to define a maximum perveance Π_0, since the maximum possible extracted current I_{ext}^{max} is limited by the Child-Langmuir law, because of the space charge of the beamlet:

$$I_{ext}^{max} = \frac{4}{9}\pi\epsilon_0\sqrt{\frac{2e}{m}}\left(\frac{r}{d}\right)^2 V_{ext}^{3/2} \tag{1.7}$$

$$\Pi_0 = \frac{I_{ext}^{max}}{V_{ext}^{3/2}} = \frac{4}{9}\pi\epsilon_0\sqrt{\frac{2e}{m}}\left(\frac{r}{d}\right)^2 \tag{1.8}$$

where ϵ_0, e, m, r and d are respectively the permittivity of free space, the electron charge, the particle mass, the radius of the aperture and the distance between the plasma grid and the extraction grid. As a consequence, Π_0 depends only on the grid characteristics and on the effective mass of the ion species.

To describe the beam optics, as reference parameter the normalized perveance Π/Π_0 is applied, due to its correlation with the *beamlet divergence*, which is an index of the beamlet opening caused by the space charge expansion. Assuming that the distribution of the angles between the beam axis and the velocity vector of the beam particles after the extraction system is a Gaussian distribution with standard deviation σ, the divergence angle ϵ is defined as:

$$\epsilon = \sqrt{2}\sigma \tag{1.9}$$

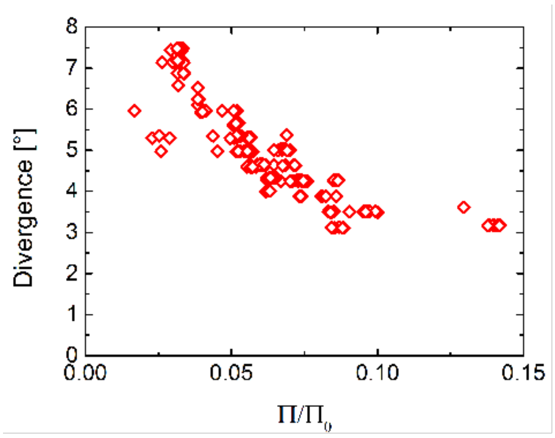

Figure 6: Typical trend of the beamlet divergence as a function of the normalized perveance [7]

Generally, the beamlet divergence ϵ depends on the perveance (hence on the extracted current and the extraction voltage) and on the ratio of the extraction to the acceleration voltage:

$$\epsilon = \epsilon \left(\Pi/\Pi_0, \frac{V_{ext}}{V_{acc}} \right) \tag{1.10}$$

The optimum normalized perveance condition is reached when the divergence is at its minimum value: with increasing Π/Π_0, the divergence decreases (this region is called *under-perveant region*) reaching it minimum, then it increases again (*over-perveant region*). In the example in Fig. 6 the typical trend of the divergence as a function of the normalized perveance is displayed. Experiments with nomalized perveance beyond the optimum value are difficult because of technical limitations which do not allow to obtain a very large extracted ion current, otherwise also the co-extracted electron current would increase too much, overcoming the safety limits on the load of the extraction grid by the co-extracted electrons.

As the extraction system can be considered as a system of electrostatic lenses, the normalized perveance is connected to the focus point of the single beamlet. This explains also the dependence of the divergence on the normalized perveance: a bad optics is correlated to a large divergence, as shown in Fig. 7.

The beamlet divergence depends also on the onset of the space charge compensation. The repulsive force caused by the negative space charge of the beamlet leads to a continuous increase of the beamlet divergence. This increase is stopped by space charge compensation downstream the extraction system, when the creation of slow positive ions in the drift region occurs mainly due to the interaction between neutrals H^0 or negative ions H^- and the background gas:

$$H^0 \text{ ionization } : H^0 + H_2 \rightarrow H^+ + e^- + H_2 \tag{1.11}$$

$$H_2 \text{ ionization } : H^0 + H_2 \rightarrow H^0 + e^- + H_2^+ \tag{1.12}$$

$$H^- \text{ double stripping } : H^- + H_2 \rightarrow H^+ + 2e^- + H_2 \tag{1.13}$$

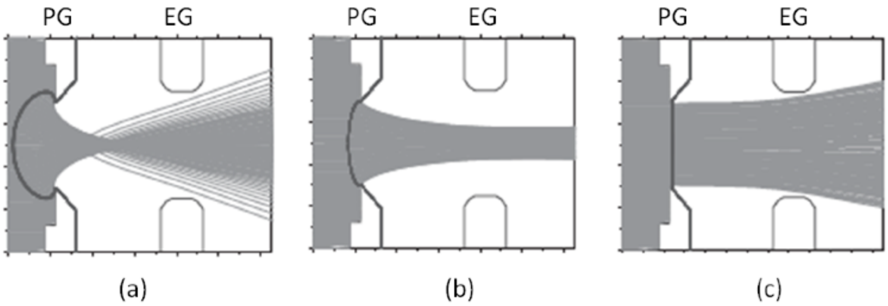

(a) (b) (c)

Figure 7: Sketch of the beamlet shape for three different cases: when the focus point is too close to the plasma grid (a) and when it is downstream the extraction grid (c), the beamlet has a bad optics and shows a big broadening. In (b) the focus point is nearby the extraction grid, and this is correlated to a good optics [3]

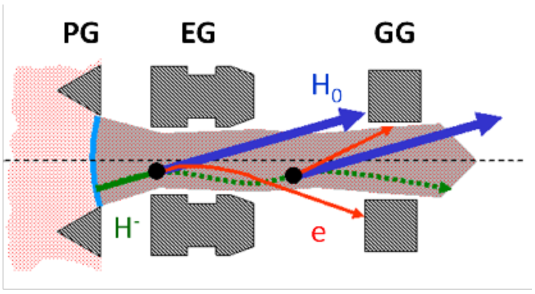

Figure 8: Sketch of the extraction system with trajectories of negative ions, stripped electrons and neutrals

An attractive force is therefore created and the beamlet broadening is reduced. The space charge compensation fully sets in at a certain distance downstream the grounded grid.

As previously said, since negative hydrogen ions have an electron binding energy of only 0.75 eV, they are easily neutralized by collisions with the residual gas not only in the drift region, but also in the extraction region before reaching their full energy. The stripping depends strongly on the gas pressure. Hence in order to minimize the stripping losses, it is necessary to minimize the pressure, and this is the reason why one requirement for the ITER NBI system is a source filling pressure below 0.3 Pa. At this pressure, the stripping losses for the ITER NBI system are foreseen to be about 30 %.

Fig. 8 represents an illustration of the extraction system, with the trajectories of negative ions, stripped particles and neutrals.

For a negative hydrogen ion beam, the stripping reactions are:

$$H^{-}\text{stripping} \ : H^{-} + H_2 \rightarrow H^{0} + e^{-} + H_2 \tag{1.14}$$

$$H^{-}\text{double stripping} \ : H^{-} + H_2 \rightarrow H^{+} + 2e^{-} + H_2 \tag{1.15}$$

The amount of stripping losses depends on:

- the particle energy, hence on the extraction and the acceleration voltage;
- the tank and the source pressure, because the stripping losses are correlated to the neutral density profile.

2 MATHEMATICAL MODEL

2.1 PRIMA

To verify NBI reliability, the PRIMA (Padova Research on ITER Megavolt Accelerator) facility is currently under construction at Consorzio RFX (Padova) in the CNR research area; it includes the full power injector MITICA (Megavolt ITER Injector & Concept Advancement) and the negative ion source SPIDER (Source for Production of Ion of Deuterium Extracted from Rf plasma) [26].

The SPIDER test bed shall test the full scale ITER HNB ion source to full ITER specification. The main objective of the SPIDER test bed is to optimize, as far as possible, the performance of the full ITER size ion source at [25]:

- full extracted current;
- full pulse length for the Hydrogen Neutral Beam (HNB) and Deuterium Neutral Beam (DNB);
- source uniformity within ±10%;
- in hydrogen and deuterium operation.

The main parameters of the SPIDER test bed are summarized in Tab. 2 [25].

The main objective of the MITICA test bed is to optimize, as far as possible, the development of the full ITER heating neutral beam injector at [25]:

- full extracted and accelerated current;
- full beam energy;
- full pulse length for the HNB (3600 seconds);
- with the required beam optics needed at ITER;
- in hydrogen and deuterium operation.

The main parameters of the MITICA test bed are summarized in Tab. 3 [25].

	Unit	**H**	**D**
Beam energy	keV	100	100
Maximum Beam Source pressure	Pa	< 0.3	< 0.3
Uniformity	%	±10	±10
Extracted current density	A/m^2	> 355	> 285
Beam on time	s	3600	3600
Co-extracted electron fraction (e^-/H^-) and (e^-/D^-)		< 0.5	< 1

Table 2: SPIDER test bed main parameters [25]

	Unit	H	D
Beam energy	keV	870	1000
Acceleration current	A	49	40
Maximum Beam Source pressure	Pa	0.3	0.3
Beamlet divergence	mrad	≤ 7	≤ 7
Beam on time	s	3600	3600
Co-extracted electron fraction (e^-/H^-) and (e^-/D^-)		< 0.5	< 1

Table 3: MITICA test bed main parameters [25]

2.2 STRIKE

One of the major goals of SPIDER [24] is to provide a uniform negative ion beam with a maximum ±10% variation of the power over the beam cross-section. Investigation of the divergence and the halo of the beam generated in the beam source, of the uniformity of the ion current and of stripping losses have to be carried out. To this end, a movable diagnostic calorimeter, STRIKE (Short-Time Retractable Instrumented Kalorimeter Experiment), is being designed [20].

2.2.1 Physical requirements

The beam consists of 1280 beamlets, arranged in 16 (4 x 4 symmetry) beamlet groups, with 5 x 16 beamlets in the horizontal and the vertical directions respectively in each group. The front side of STRIKE is directly hit by the beam and the device shall provide a measurement of the heating power associated to the beam (see Fig. 9). Because of the presence of other beam diagnostic systems and with the aim of reducing the impact on overall pumping efficiency, STRIKE shall be located at about 1 m from the beam source. The measurement of the heating power uniformity, given by the impinging ions, can be carried out by means of thermal cameras that yield direct measurement of the footprint of the beam.

The beam particles can excite the gas between the beam source and the calorimeter, including the material sublimated from the calorimeter surfaces due to heating, thus creating an optically emitting layer. Moreover, small particles can be extracted and overheated, thus emitting thermal radiation. Consequently the observation of STRIKE tiles shall be performed on the rear side.

A charged particle beam is characterized by some divergence, for instance due to the repulsion force of the particles with the same charge. Changing the measurement position of STRIKE allows a double characterization of the beam, which results in the possibility of measuring the beam divergence and the halo. The latter is possibly due to the creation, in the accelerator, of neutrals which have not been fully accelerated and are no longer controlled by the electric field.

Since the negative ion source of the neutral beam injectors for ITER requires that the co-extracted electron current is not larger than the negative ion current, uniformity of the beam power shall be compared to uniformity of the negative ion current in order to distinguish charged particles from neutrals. This will also allow the investigation of stripping losses and ionization during the collisions of D^+, D^- and D^0 with the background gas.

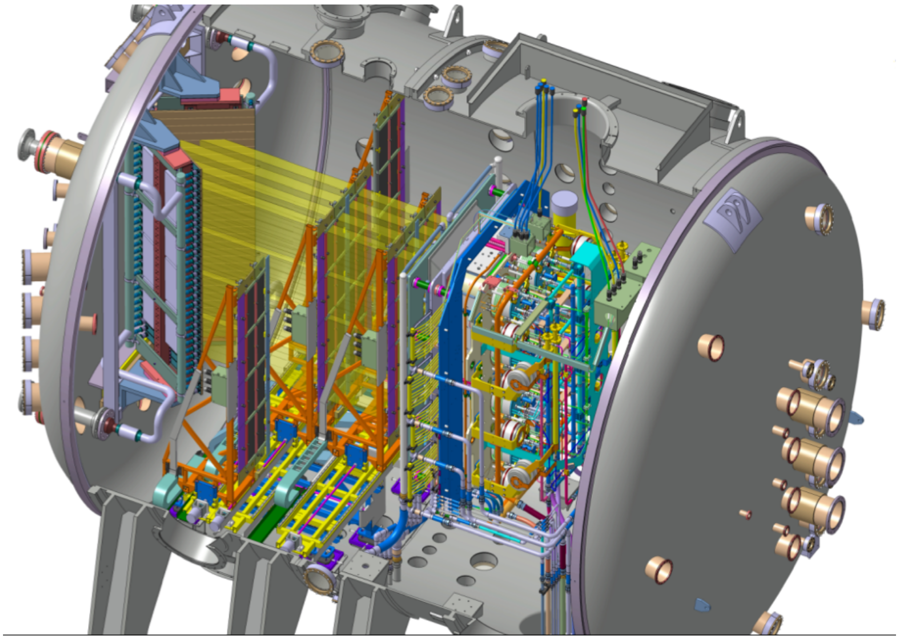

Figure 9: STRIKE calorimeter inside of SPIDER ion source

Thus, the electrical current reaching the tiles shall also be measured and electrical insulation and polarization of the tiles shall be provided to pull secondary electrons back to the calorimeter surface [23].

2.2.2 Design

In order to reproduce the geometry of the SPIDER beam, which is made of 4×4 groups of 80 beamlets each, STRIKE, represented in Fig. 10 is divided into 16 tiles directly exposed to the beam.

Since the calorimeter will be observed on the rear side and in order to preserve the image from one side to the other, special material is required, exhibiting very high thermal conductivity in the thickness direction against the other two, like one-dimensional Carbon Fibre Composite (CFC).

STRIKE consists of two panels symmetrically disposed perpendicularly to the beam. When the calorimeter panels are in the closed position, the heat generated by the particles impinging on the front side is promptly transmitted to the other side of the CFC tiles. The thermal image that appears on the rear side of the tile panels is captured by means of two thermal cameras, each one observing one half of the panel from dedicated portholes on the vessel. With proper calibration of the thermal cameras it is possible to reconstruct the tile temperature profiles. This allows a measurement of the beam uniformity. The panels in closed position shall be placed at two different axial distances from the beam source, in order to measure the beamlets divergence. Furthermore, when STRIKE is not in use, it has to be in open position, in order to let the beam pass through (in this case the beam power is exhausted on the beam dump) and to allow the operation of other diagnostic systems.

For long pulse operation of SPIDER the beam will be dumped on a surface capable of receiving the whole energy, the beam dump. In order to permit this, STRIKE shall be opened.

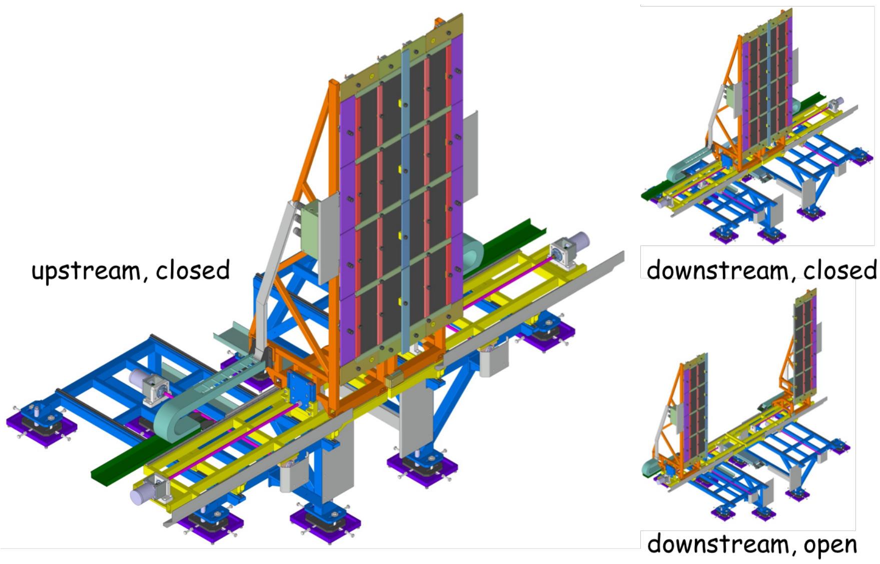

Figure 10: CAD view of STRIKE in the different possible positions

Mechanical requirements

The calorimeter shall operate in two different configurations: "open", where the beam shall not be intercepted by STRIKE, and "closed", where the entire beam power shall be intercepted. Furthermore, two axially distinct positions shall be identified for beam divergence measurement; the ratio between the axial distances of STRIKE from the ion beam origin shall be at least 2.

In order to carry out electrical measurements of current flowing in each panel element (5 A, with a safety factor of 0.3, without taking into account the contribution due to electrons), each tile shall be electrically insulated. The characteristics of beam pulses are: pulse duration 10 s, time between pulses 1200 s, beam power 5 MW, Gaussian shaped heat flux with peak value of 20 MW/m^2.

CFC tiles and panels

One-directional CFC (1D-CFC) consists of a matrix of carbon in which carbon fibers are aligned along the thickness. This fiber layout gives a high ratio (up to 20) between thermal conductivities along the thickness and in-plane directions, but reduces the structural resistance of the material significantly. CFC materials can resist temperatures up to 2700 °C (in inert gas or in vacuum) and temperature fluctuations of 1500 °C (excellent thermal shock behavior); moreover, they are distinguished by good thermal and electrical conductivity and effective chemical resistance. These features make 1D-CFC the proper material to realize STRIKE tiles, since they are subjected to cyclic thermal loads with maximum power densities up to 10 MW/m^2 considering beam optics, pulse duty cycle and tile position and orientation.

The external part of the beam is composed by low density divergent particles (halo) that are intercepted by kerbs to prevent vessel heating and damage. Since the kerbs are not the object of IR thermal measurements, a material with higher mechanical resistance (quasi-isotropic graphite) is selected.

It has been verified [20] that thermal radiation towards the vessel is sufficient to cool down the tiles, so that no active cooling is required, which would have interfered with the thermal measurements by introducing thermal gradients.

Moving and supporting system

STRIKE is composed of two independent symmetrical parts, left and right, which works in pair. Each tile has to be sustained and remotely positioned inside the vacuum vessel and kept in definite positions.

The supporting system shall neither interfere with the thermal camera view nor obscure any portion of the tiles. Thus, a wide portal structure on which the tile panel shall be installed has been developed. Having the support structure under the portal, this solution has almost no impact on the tile panels.

It has been decided to obtain the required displacements by means of two independent movements: transverse translation (open/closed) and axial translation (forward/backward).

Diagnostics

The different measurements implemented in STRIKE are: local temperature provided by thermocouples, beam footprint temperature measured by IR cameras and negative ion currents of beamlet groups [11].

The thermocouples to be installed in STRIKE are type N and present low hysteresis, constant sensitivity and high irradiation strength. Thin thermocouple cables are an important feature since they will shadow the IR camera view; moreover, the smaller the external thermocouple diameter, the shorter the response time is. Mineral insulation will be adopted in the hottest region.

In STRIKE, thermocouples shall be positioned to monitor the temperature of all elements, to provide an absolute calibration of IR cameras and to give a set of few spatially resolved measurements. Thus, each kerb is provided with a thermocouple and two sensors are located in each tile for allowing calibration of thermal cameras in positions with high and low temperatures.

The thermocouples shall be inserted only for few millimeters in the rear side of the tiles, to provide a comparison with the thermal cameras while maintaining a good thermal contact.

2.3 NIFS EXPERIMENT

The main component of STRIKE is constituted by one-directional carbon-fibre-carbon-composite (CFC) tiles, observed on the rear side by infrared cameras. Prototype tiles have been employed in 2012 in the BATMAN device at IPP-Garching (Germany) as a small scale version (mini-STRIKE) of the entire system, to study the capabilities of the diagnostic. It was verified that the system is capable of investigating the beam features even on the beamlet scale. Thus a beamlet monitor has been designed to investigate the properties of the negative ion beam test stand of the neutral beam injectors of the LHD experiment (NIFS). This beam should exhibit a spatial pattern resembling the fine structure expected in SPIDER [2].

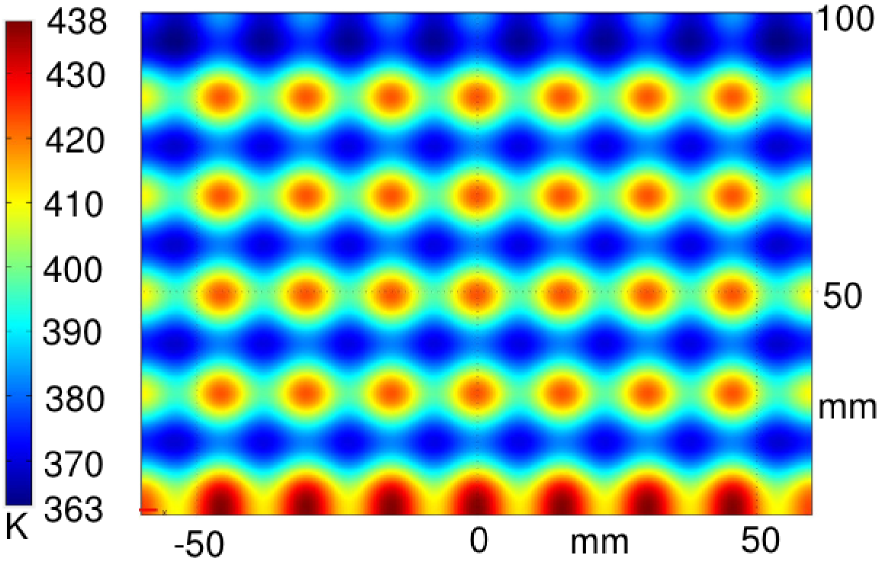

Figure 11: Simulated temperature profile on the rear side of the CFC tile after 1 s beam pulse [22]

2.3.1 Design and installation of the system

Mini-STRIKE is dedicated to measure the beam profile on the spatial scale of the single beamlets. In the system employed in BATMAN, two carbon-fibre-carbon (CFC) composite tiles were used, whose thermal behavior had been investigated in detail [21]; a copper mask was placed in front of the tiles to artificially create beamlet-like structures, providing a spatial sampling of the energy flux associated to the beam. The beamlet divergence in the test stand of the neutral beam injectors of the LHD experiment is anticipated to be in the range of few mrad [28]. As the beamlet monitor will be located around 1 m away from the grounded grid, it is then expected that the beamlets can be singularly discerned. This was verified by a dedicated series of non-linear thermal simulations, including thermal radiation, using the finite-element COMSOL code [6]. The result of the simulation after 1 s application of a beam having a divergence of 5 $mrad$ and a particle energy of 45 keV is shown in Fig. 11. The expected temperature increase is around 70 K [2].

As cooling of the CFC tiles is a very slow process (being only due to radiation), the tile temperature increases from pulse to pulse; simulations of pulses with 1 s beam-on and 180 s beam-off show that, if the starting temperature is above 600 K, thermal radiation affects the temperature in such a way that at the beginning of the following pulse the temperature is back to the same starting value. In this temperatures range it was also deduced that the expected operating conditions should not result in excessive evaporation of carbon from the CFC tiles, which might have poisoned the source; hence the distance of the beamlet monitor from the grounded grid was selected to be 0.76 m, as a compromise between diagnostic requirements and mechanical constraints. To maximize the measurement area, during the design of the beamlet monitor, particular care was devoted to leaving as free as possible the area in front of the tiles, while protecting the unavoidable supporting structures from direct exposure to the beam [2].

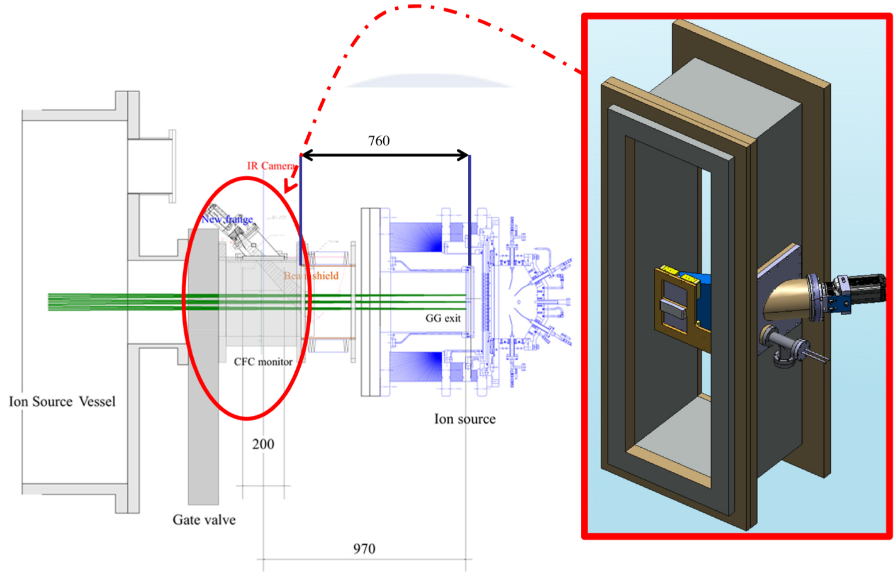

Figure 12: Layout of the beamlet monitor in the test stand beam line (the beam is sketched in green) and CAD view of the beamlet monitor inside the drift tube [22]

Fig. 12, on the left, shows a horizontal section of the layout of the beamlet monitor in the test stand beam line; mini-STRIKE is installed in the drift tube, which connects the ion source to the ion source vessel. On the right-hand side of the figure, the view cone of the camera is evidenced in blue, the infrared camera and the feed-through for thermal signals and cooling lines can be seen on the right-hand side.

The copper mask is water cooled and the temperature of the tiles is measured by means of thermocouples, providing a direct and local comparison with the infrared camera measurements; another thermocouple is fixed to the copper mask (not visible in the figure). As the cooling circuit is only around the edge of the mask, the copper part covering the gap in between the two tiles is protected from direct beam power deposition by a rectangular graphite tile (Fig. 13); the mask extends on one side to protect supporting arm, cooling pipes and thermocouple cables running towards the vacuum feed-through. The CFC tiles are perpendicular to the beam, whereas the infrared camera observes the rear side of the tiles at an angle of around 45°, depending on the position on the tile.

2.3.2 Thermal camera data

The mini-STRIKE infrared camera records with a frequency of 25 frames per second for few tens of seconds; each frame consists of a matrix of 640×480 pixels whose values correspond to the temperature. The thermal camera is absolutely calibrated, taking into account the measured emissivity very close to 1 of the CFC tile [10] as well as the object distance ($0.76\ m$). The error associated to the measured temperature is $2\ K$ or 2% (the greater error between these two values has to be considered). The camera is triggered several frames before the beam start, in order to measure the background temperature before the beam-on phase. The beam pulse lasts $0.5 - 1\ s$.

It should be noted that only few beamlets were operated during the beamlet monitor experiments. Specifically, only three rows, each consisting

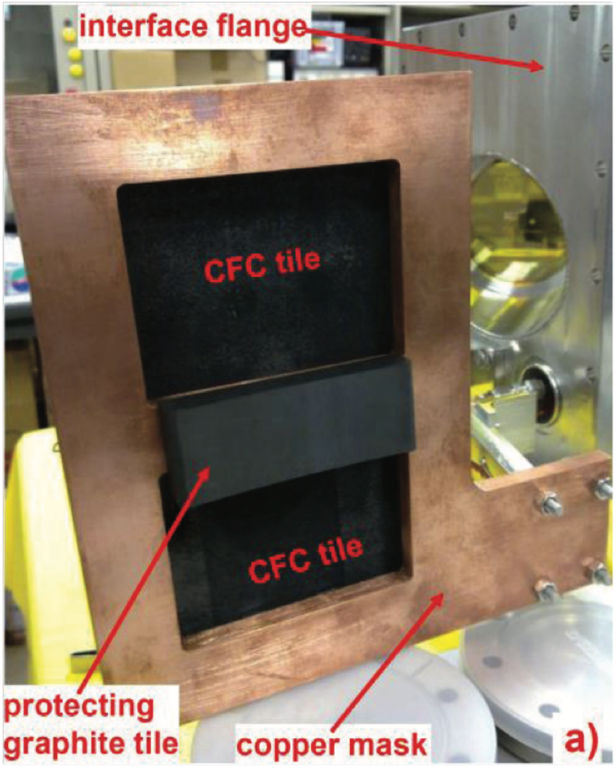

Figure 13: Front side of mini-STRIKE [2]

of 5 apertures, were left open in each of the half grids composing the whole grid of the test stand source (Fig. 14). Thus 3×5 beamlets are expected to be centered on each tile. The difference in the grid aperture shape results in different optimal conditions in terms of beamlet optics, as already verified in the past [28]; this was found also in the present experimental campaign.

The measurement campaign in the test stand of LHD neutral beam injectors is a complete test of the whole STRIKE calorimeter, though on a smaller spatial scale. The test includes data analysis. Several strategies were applied to the extraction of relevant information from the measured data, with increasing level of confidence, usefulness of the resulting data and time required to perform the analysis. A fast on-line analysis was carried out in between the beam pulses, to guide the experimentation; this analysis, performed by a Visual Basic program in the Excel environment, consists in the visualization of the temperature profiles along horizontal and vertical lines in each half-grid. This way it was demonstrated that from STRIKE, applied to the 1280 beamlets of the SPIDER device, it will be possible to extract sufficient information, like local maxima of the heat associated to the beamlets and distinguishability of neighboring beamlets (suggesting good beam optics), even using fast and simple methods, which can be implemented on-line [2].

Off-line, two more precise data analysis techniques were implemented. The programming languages used to carry out the data analysis were MATLAB and IDL. For each pulse, both programs consider the frames in which the beam is on, after subtracting the background pattern (average over several frames before the beam start). Hence only temperature increases with respect to the initial condition are considered in the following. Data manipulation begins with a correction of the perspective, which is necessary

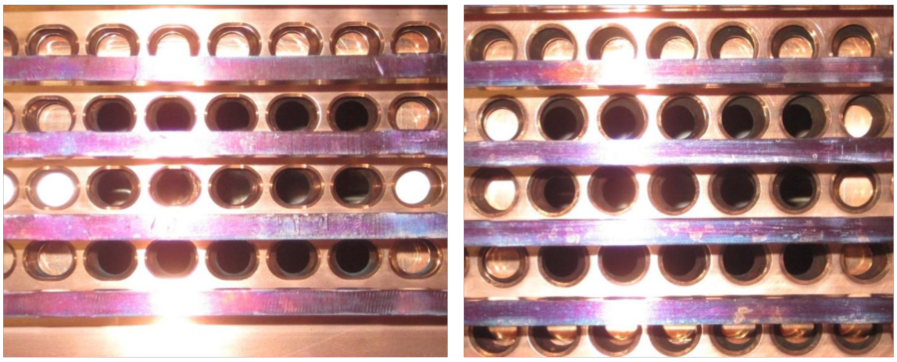

Figure 14: Active portion of the accelerator after masking several plasma grid apertures: top grid with oval apertures (left), bottom grid with circular apertures (right) [2]

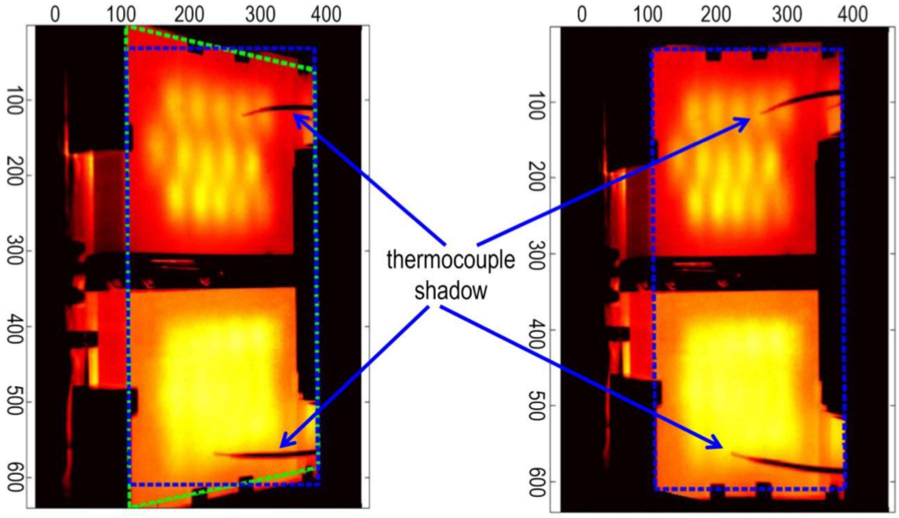

Figure 15: Original infrared image (left); same image after application of the homography (right) to recover the proper size in the horizontal direction despite the tilted observation (45°). The shadows of the thermocouples are also shown

because the viewing angle is 45° (see Fig. 12), and with the conversion of x-axis and y-axis from pixels to millimeters. In the MATLAB program the proper shape of the tile is recovered by a homography, essentially amounting to stretching the horizontal axis, which shrank during the projection of the image onto the sensor of the infrared camera (Fig. 15). After recovering the perspective, the region relevant for further analyses is selected, i.e. the region corresponding to the two tiles, upon excluding the zone in between the two tiles. Then the position of the centers of the beamlets is estimated; sometimes this requires data smoothing and in certain cases the beamlet positions obtained while analyzing the previous frame are used. At any rate, the position of the beamlets is kept fixed in the subsequent steps, in which a superposition of 15 two-dimensional, possibly elliptical Gauss curves is fit to the data [2].

When applying the first fitting method, the pixels affected by the thermocouple shadows were retained during the data analysis, which resulted in a poor reconstruction of the neighboring beamlets. Moreover, this method adopted a description of the shape of the single temperature peaks which

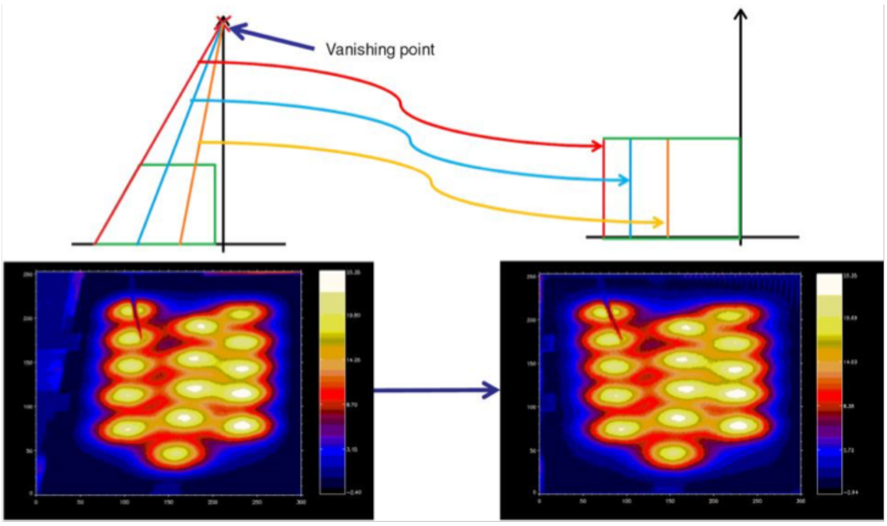

Figure 16: Second fitting method: original infrared image (left); same image after the correction of perspective (right). The image is rotated by 90° with respect to Fig. 15: the real vertical direction is along the horizontal direction [2]

had already proved to be improvable: indeed, as discussed in ref. [21], the Gauss curve is less suited to describe the temperature peak on the rear side of the tile when a localized energy flux hits the front side. Finally, a simple way of recovering the perspective is used, consisting in allowing the vertical pixel-to-mm conversion factor to depend on the horizontal direction. For all these reasons a very precise shape of the beamlets is not expected. However, this method is easy to implement and was applied to the preliminary data analyses, in between the experimental days, when not too much time could be devoted to optimizing the analysis software [2].

The second fitting method requires a longer time but has more precise results and it is the one chosen in all the following analyses. After the same preliminary steps as the previous procedure, the region relevant for the analysis is selected; in this case the shadows of the two thermocouples are excluded. To recover from the tilting of the infrared camera and considering that the infrared camera is quite close to the CFC tiles (only about 0.25 m away), a more refined procedure is applied to correct for the perspective. Specifically, some straight lines are identified in the image, which are parallel in reality but appear at varying angle in the infrared image (Fig. 16). The vanishing point, where these lines apparently coalesce if extended, is identified. Finally a bilinear function is applied to all image pixels to move them to their real position. As recovering from the projection of the scene onto the camera sensor effectively distorts the original image, the array is resampled over a rectangular arrangement of the pixels. Subsequently the bell-shaped function, which was found to fit best the thermal pattern measured on the rear side of the CFC tiles subjected to a point-like laser beam on the front side (modified two-dimensional Hubbert function [9]), is used to fit the infrared pattern, simultaneously involving all peaks of each tile in turn.

In some cases a rotation angle was also considered, for a total of a 105 parameters. The comparison of the residuals of the second fitting method with the ones of the first one shows that the two-dimensional function fits the data better than 10% and that the second method is better [2]. The estimation of the error on the fit parameters is performed by inverting the Hessian matrix of the χ^2 function; the diagonal elements of the inverse are assumed as the variances of the fit parameters.

2.4 THE TRANSFER FUNCTION

The aim of the analysis of the temperature profiles on the rear side of the CFC tiles is the reconstruction of the incident energy flux on the front side.

The tile can be modeled as a *system*: an object that from an input (the energy flux on the front side) produces an output (the temperature profile on the rear side); mathematically it is an operator that acts from an input space (the energy flux profiles set) to an output space (the temperature profiles set). Denoting with $O[\,]$ this operator and with $u(l)$ an input function in the generic variable l, its output will be $v(l) = O[u(l)]$. Let's consider the Dirac delta function $\delta(l)$ as the input. The operator O produces a function $h(l)$, called *impulse response function of the operator O*.

Linear systems represent an important class of systems whose operator is linear and the superposition principle can be applied: the net response at a given place and time caused by two or more stimuli is the sum of the responses which would have been caused by each stimulus individually.

Using Dirac delta function's properties, any input can be written as: $u(l) = \int_{\lambda \in D} u(\lambda)\delta(l-\lambda)\mathrm{d}\lambda$, where D is the domain of definition of u; applying the linear operator $O[\,]$ on this input, it is obtained:

$$v(l) = O[u(l)] = \int_{\lambda \in D} u(\lambda) O[\delta(l-\lambda)]\mathrm{d}\lambda \tag{2.1}$$

Moreover, if the operator is translation-invariant, i.e. $O[\delta(l+l_0)] = h(l+l_0)$, denoting by h the impulse response, the output becomes:

$$v(l) = \int_{\lambda \in D} u(\lambda) h(l-\lambda)\mathrm{d}\lambda \tag{2.2}$$

The output v is given by the convolution of the input with the impulse response, that is called **transfer function**.

In this case, both input and output are functions of $\{t, x, y\} \in \mathbb{R}^+ \times \mathbb{R}^2$. So the convolution equation 2.2 becomes:

$$v(t,x,y) = \int \int_{\mathbb{R}^2} \int_{\mathbb{R}^+} u(\tau,\xi,\psi) h(t-\tau, x-\xi, y-\psi)\mathrm{d}\tau \mathrm{d}\xi \mathrm{d}\psi \tag{2.3}$$

with the transfer function defined by the impulse response

$$v^{\delta}(t,x,y) = \int \int_{\mathbb{R}^2} \int_{\mathbb{R}^+} \delta(\tau,\xi,\psi) h(t-\tau, x-\xi, y-\psi)\mathrm{d}\tau \mathrm{d}\xi \mathrm{d}\psi \equiv h(t,x,y) \tag{2.4}$$

and $\delta(\tau,\xi,\psi) = \delta(\tau)\delta(\xi)\delta(\psi)$.

2.5 THE FOURIER DOMAIN

Linear operations performed in one domain (time or frequency) have corresponding operations in the other domain, which are sometimes easier to perform: e.g. convolution in the time domain corresponds to ordinary multiplication in the frequency domain.

The Fourier transform of the output $v(t, x, y)$ of the equation 2.3 will be analytically obtained considering only the spatial coordinates and maintaining time as a parameter. From now on, functions in the time domain will be noted with lowercase letters, while capital letters will indicate functions in the Fourier domain. The result is:

$$\begin{aligned}
V(t,k,j) = V_t(k,j) &= \frac{1}{(\sqrt{2\pi})^2} \int_{\mathbb{R}^2} v_t(x,y) e^{-ikx} e^{-ijy} \mathrm{d}x\mathrm{d}y \\
&= \frac{1}{2\pi} \int_{\mathbb{R}^2} \left(\int_{\mathbb{R}^2} h_t(x-\xi, y-\psi) u_t(\xi,\psi) \mathrm{d}\xi\mathrm{d}\psi \right) e^{-ikx} e^{-ijy} \mathrm{d}x\mathrm{d}y \\
&= \frac{1}{2\pi} \int_{\mathbb{R}^2} \left(\int_{\mathbb{R}^2} h_t(x-\xi, y-\psi) e^{-ikx} e^{-ijy} \mathrm{d}x\mathrm{d}y \right) u_t(\xi,\psi) \mathrm{d}\xi\mathrm{d}\psi \\
&= \frac{1}{2\pi} \int_{\mathbb{R}^2} \left(\int_{\mathbb{R}^2} h_t(p,q) e^{-ikp} e^{-ijq} \mathrm{d}p\mathrm{d}q \right) u_t(\xi,\psi) e^{-ik\xi} e^{-ik\psi} \mathrm{d}\xi\mathrm{d}\psi \\
&= H_t(k,j) \int_{\mathbb{R}^2} u_t(\xi,\psi) e^{-ik\xi} e^{-ik\psi} \mathrm{d}\xi\mathrm{d}\psi \\
&= 2\pi H_t(k,j) U_t(k,j)
\end{aligned} \tag{2.5}$$

Where the substitution $p = x - \xi$ and $q = y - \psi$ has been made.

The relation between input and output in the Fourier domain is a multiplication. The transfer function, in the Fourier domain, is determined, within a multiplication factor, by the ratio between the transform of the output and the transform of the input:

$$H_t(k,j) = V_t^{\delta}(k,j) = \frac{V_t(k,j)}{2\pi U_t(k,j)} \propto \frac{V_t(k,j)}{U_t(k,j)} \tag{2.6}$$

For any given output, knowing the transfer function of the system, it is possible to reconstruct the input that has generated it by inverting relation 2.6 and then re-inverting:

$$u_t(x,y) = \frac{1}{2\pi} \int_{\mathbb{R}^2} \frac{V_t(k,j)}{2\pi H_t(k,j)} e^{ikx} e^{ijy} \mathrm{d}k\mathrm{d}j \tag{2.7}$$

2.5.1 Inclusion of time

To include time in the analysis of the transfer function, the same integral used to transform convolution in the time domain in ordinary multiplication in the Fourier domain is calculated; but some clarifications are needed: while analyzing spatial coordinates the causality principle can be ignored, this topic can not be neglected considering time. This can be noticed in integral 2.3 where the integration domain of τ is not $\mathbb{R}$ but $\mathbb{R}^+ = [0, +\infty[$.

In order to use the Fourier notation, it is then necessary to multiply the integrand by the Heaviside function, after verifying the absolute convergence of the integral. The result is:

$$v(t,x,y) = \int \int_{\mathbb{R}^2} \int_{\mathbb{R}} h(t-\tau, x-\xi, y-\psi) u(\tau,\xi,\psi) \Theta(\tau) \mathrm{d}\tau\mathrm{d}\xi\mathrm{d}\psi \tag{2.8}$$

The result in Fourier space, using the same notation as above, is given by:

$$\begin{aligned} V(\omega,k,j) &= \frac{1}{\sqrt{2\pi}} \int_{\mathbb{R}} V(t,k,j) e^{-i\omega t} \mathrm{d}t \\ &= \frac{1}{\sqrt{2\pi}} \int_{\mathbb{R}} \left(\int_{\mathbb{R}} 2\pi H(t-\tau,k,j) U(\tau,k,j) \Theta(\tau) \mathrm{d}\tau \right) e^{-i\omega t} \mathrm{d}t \\ &= \frac{1}{\sqrt{2\pi}} \int_{\mathbb{R}} \left(\int_{\mathbb{R}} H(t-\tau,k,j) e^{-i\omega t} \mathrm{d}t \right) U(\tau,k,j) \Theta(\tau) \mathrm{d}\tau \\ &= \sqrt{2\pi} \int_{\mathbb{R}} \left(\int_{\mathbb{R}} H(s,k,j) e^{-i\omega s} \mathrm{d}s \right) U(\tau,k,j) \Theta(\tau) e^{-i\omega\tau} \mathrm{d}\tau \\ &= \sqrt{2\pi} H(\omega,k,j) \int_{\mathbb{R}} U(\tau,k,j) \Theta(\tau) e^{-i\omega\tau} \mathrm{d}\tau \\ &= 2\pi H(\omega,k,j) \hat{U}(\omega,k,j) \end{aligned} \tag{2.9}$$

The relation found in 2.9 is similar to the one derived using time as a fixed parameter; the only difference with the temporal analysis is that in that case the Fourier transform of the function has not been calculated directly, but the transform of the product of the function by the Heaviside function.

This difference is very significant from a computational point of view, as it makes the Fast Fourier Transform algorithm inapplicable to the tridimensional Discrete Fourier Transform (DFT) calculation. The time dependency of the function will not be discussed further in this work, which will use the two-dimensional Fourier transform with a set $t - t_0$. In order to set a fixed time value, it is assumed that the energy flux profile used to determine the transfer function has the same trend as the energy flux that has to be reconstruct. This assumption is used in all the experimental results analyzed (in particular, the temporal trend is supposed to be a Heaviside Θ).

2.6 LINEARITY OF THE SYSTEM

2.6.1 Heat equation

The equation that describes heat transmission in an anisotropic medium, with cartesian propagation axes, is given by [4]:

$$\rho c \frac{\partial v}{\partial t} + \frac{\partial f_x}{\partial x} + \frac{\partial f_y}{\partial y} + \frac{\partial f_z}{\partial z} = 0 \tag{2.10}$$

where $v(t,x,y,z)$, ρ and c represent the temperature, mass density and specific heat of the medium, and f_x, f_y, f_z are defined as follows:

$$f_x = -K_x(v) \frac{\partial v}{\partial x}; \qquad f_y = -K_y(v) \frac{\partial v}{\partial y}; \qquad f_z = -K_z(v) \frac{\partial v}{\partial z}. \tag{2.11}$$

$(K_x, K_y, K_z) =: \vec{K}$ are the thermal conductivity coefficients, which are assumed not explicitly dependent on position and time. Assuming that $\vec{K}$, c and ρ do not depend on temperature, the heat equation becomes:

$$\rho c \frac{\partial v}{\partial t} - K_x \frac{\partial^2 v}{\partial x^2} - K_y \frac{\partial^2 v}{\partial y^2} - K_z \frac{\partial^2 v}{\partial z^2} = 0 \tag{2.12}$$

which is linear: a linear combination of its solutions it still is a solution.

2.6.2 Thermal parameters of the tiles

1D-CFC is a very thermally anisotropic material: its thermal conductivity has two different values in orthogonal directions $K_\perp$ and $K_\parallel$, with the latter being approximately 20 times larger than the former.

The following relations between the two coefficients were measured for the STRIKE experiment tiles (with v expressed in Kelvins) [5]:

$$K_\parallel = K_z = (98.6 + 525.6e^{-(v-273.15)/782.9} + 279.4e^{-(v-273.15)/105.9}) \, \frac{W}{mK} \tag{2.13}$$

$$K_\perp = K_x = K_y = \left(\frac{K_\parallel}{20.33 - (v - 173.15)/384} \right) \frac{W}{mK} \tag{2.14}$$

The specific heat is a function of the temperature (again, with v expressed in Kelvins) [5]:

$$c = \left(1800 - 1280e^{-(v-273.15)/340} + 150e^{-(v-273.15)/40} \right) \frac{J}{kgK} \tag{2.15}$$

As equation 2.15 shows, the function is exponential, making verification of its effect necessary.

The temperature range on the tile surface in the experiments goes from $v_0 = 300K$ to $v_{max} = 350K$. The extreme values are:

- $K_\parallel(v_0) = 823.3 \; Wm^{-1}K^{-1}$ $\quad K_\parallel(v_{max}) = 710.3 \; Wm^{-1}K^{-1}$
  $\Delta K_\parallel / K_{\parallel(v_0)} = 15.9\%$
- $K_\perp(v_0) = 40.6 \; Wm^{-1}K^{-1}$ $\quad K_\perp(v_{max}) = 35.3 \; Wm^{-1}K^{-1}$
  $\Delta K_\perp / K_{\perp(v_0)} = 15.2\%$
- $c(v_0) = 693.9 \; Jkg^{-1}K^{-1}$ $\quad c(v_{max}) = 800.9 \; Jkg^{-1}K^{-1}$
  $\Delta c / c(v_0) = 13.4\%$

and the intermediate values are:

- $K_z = K_\parallel = \vec{K}_\parallel = \frac{K_\parallel(v_{max} + K_\parallel(v_0)}{2} = 766.8 \, Wm^{-1}K-1$ with a maximum percentage error $\frac{\Delta K_\parallel/2}{\vec{K}_\parallel} = 7.4\%$;
- $K_x = K_y = K_\perp = \vec{K}_\perp = \frac{K_\perp(v_{max}) + K_\perp(v_0)}{2} = 38.0 \, Wm^{-1}K-1$ with a maximum percentage error $\frac{\Delta K_\perp/2}{\vec{K}_\perp} = 7.0\%$;
- $c = \vec{c} = \frac{c(v_{max}) + c(v_0)}{2} = 747.4 \, Jkg^{-1}K^{-1}$ with a maximum percentage error $\frac{\Delta c/2}{\vec{c}} = 7.2\%$;

The variation is small but theoretically significant. It can be still considered negligible in the empirical results: the parallel thermal conductivity and specific heat influence the heat diffusion phenomena with a thermal diffusivity coefficient $D_\parallel = \frac{K_\parallel}{\rho c}$. The errors on the estimates of $K_\parallel$ and ρ propagate in a variation of 15% in the results. The transmission delay from the front to the back of the tile has been measured as about $150 \, ms$, with

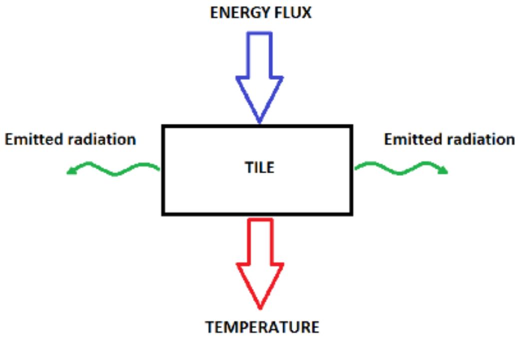

Figure 17: System represented by the CFC tile and boundary conditions

a variation of about 20% or $20ms$. The thermal camera has a sampling frequency of $25\,Hz$, corresponding to a $40ms$ sampling interval. The changes due to a delay variation of $20\,ms$ are then not measurable by the thermal camera, making the diffusivity coefficient variation negligible. The linear approximation of the system is valid for the results obtained.

2.6.3 Boundary conditions

The boundary conditions considered are:

- the energy flux on the front side of the tile is known (one laser or beamlets on one surface, zero on the others)
- the emitted radiative power is given by the black body law
- there is no energy dissipation by convection (the tile is in vacuum) or conduction between the tile and its support

Assuming that the tile is a parallelepiped $[-a, a] \times [-b, b] \times [0, L]$ (with $a, b \gg L > 0$) whose bigger faces are parallel to the xy plane and the thickness L is in direction z, the boundary equations can be expressed as:

$$\pm K_x \frac{\partial v(t, \pm a, y, z)}{\partial x} + H(v(t, \pm a, y, z)^4 - v_0^4) = 0 \text{ for } x = \pm a \tag{2.16}$$

$$\pm K_y \frac{\partial v(t, x, \pm b, z)}{\partial y} + H(v(t, x, \pm b, z)^4 - v_0^4) = 0 \text{ for } y = \pm b \tag{2.17}$$

$$-K_z \frac{\partial v(t, x, y, 0)}{\partial z} + H(v(t, x, y, 0)^4 - v_0^4) - F(t, x, y, 0) = 0 \text{ for } z = 0 \tag{2.18}$$

$$K_z \frac{\partial v(t, x, y, L)}{\partial z} + H(v(t, x, y, L)^4 - v_0^4) = 0 \text{ for } z = L \tag{2.19}$$

with the assumption that the energy flux $F(t, x, y, z)$ hits the tile in $z = 0$ and goes toward $z > 0$.

$R = H(v^4 - v_0^4)$ represents the emitted radiative energy: H is the CFC radiative emission constant, and is equal to $\epsilon\sigma_{SB}$, where $\sigma_{SB} = 5.6707373 \times$

$10^{-8} \frac{W}{m^2 K^4}$ (the Stefan-Boltzmann constant) and $\epsilon = 1$ is the emissivity coefficient of the tile (which was determined empirically, as the tile behaves like a black body). The component v^4 makes the general case a non-linear problem. The problem becomes linear when the black body component is negligible, or at least can be approximated by its linear component $R^{lin} = 4\sigma_{SB} v_0^3 (v - v_0)$.

The maximum measured temperature difference in the laser tests was about 30 K, and 10 K with the negative ion beam. A conservative estimate $\Delta v = 50\ K$ is used to leave a wide safety margin in both cases.

Considering now the ion beam test; the beams impinge on a $196.0 \times 91.5 \times 22\ mm$ tile, whose overall area is $S = 4.45 \cdot 10^{-2}\ m^2$, the biggest available in the laser tests (in BATMAN and LHD use $120 \times 90 \times 20\ mm$ tiles are employed). Setting $v = 350\ K$ and $v_0 = 300\ K$ (environment temperature), the resulting energy flux is $R = 3.92 \cdot 10^2\ \frac{W}{m^2}$ and, assuming a uniform surface temperature of the tile of $350\ K$, it is obtained $P = RS = 17.4\ W$. The negative ion beam is accelerated by a potential difference $\Delta V = (35 \div 65)\ kV$ and a current $I = 0.3 \div 0.7\ A$. The power carried by the beam is $P_{beam} = \Delta V I = (10.5 \div 45.5)\ kW$. Since $\frac{P}{P_{beam}} = 0.0004 \div 0.0017 \ll 1$; the radiant contribution can be neglected in ion beam tests.

The laser tests used a CO_2 laser with power $P_{laser} = (20 \div 100)\ W$. In this case, the temperature variation is concentrated in a small region of the tile, which can be approximated as a circle whose radius is $r \approx 30\ mm$ on both the bigger sides of the tile. The total surface of both sides is $S' = 5.66 \cdot 10^{-3}\ m^2$, and the emitted power with a temperature of $350\ K$ is $P' = 2.21\ W$, small but still in the same order of magnitude as P_{laser}.

Finally, the linearization is considered, obtaining $R^{lin} = 306.2\ \frac{W}{m^2}$. The difference between the real irradiated power and the linearized model is $\Delta P = \Delta R \cdot S' = 0.48\ W$, and $\frac{\Delta P'}{P_{laser}} = 0.004 \div 0.024 \ll 1$. The system can be considered as linear without significant errors in both configurations.

2.7 THE DISCRETE FOURIER TRANSFORM

The temperature profiles of the tiles can be considered as two-variable functions $v(x, y) : \mathbb{R}^2 \to \mathbb{R}$, whose support is compact, as the physical sides of the tiles are bounded. The functions are smooth in the interior of their support. These profiles are measured by samples of these functions taken by the thermal camera; the sample size corresponds to the number of pixels in each frame. A matrix $M \times N$ is obtained, where M is the number of samples on the x axis and N on the y axis; every element contains the measured temperature in that coordinate. Calculating the Continuous Fourier Transform (CFT) of any given continuous two-variable function $f(x, y)$ requires integration in $\mathbb{R}^2$. As the support of $v(x, y)$ is bounded, its CFT will have non-zero values in an unbounded space. Approximating the CFT with the Discrete Fourier Transform (DFT) becomes necessary; the DFT is given by

$$F(k, j) = \frac{1}{MN} \sum_{x=0}^{M-1} \sum_{y=0}^{N-1} f(x, y) e^{-i\left(\frac{kx}{M} + \frac{jy}{N}\right)} \tag{2.20}$$

All the values of the DFT can fit in an $M \times N$ matrix, whose step is $\frac{2\pi}{M}$ on the k axis and $\frac{2\pi}{N}$ on the j axis. Both axis cover the full 2π interval. This notation allows the comparison between transforms of the same profile, sampled on different matrices with the same spatial resolution. In order to compare matrices with different resolutions, they have to be multiplied by the inverse of the resolution, obtaining the Fourier space units $\frac{2\pi}{M\chi_x}$ and $\frac{2\pi}{N\chi_y}$ (in rad/mm). The same holds for the continuous inverse transform, which can be replaced by the discrete inverse transform, whose formula is:

$$f(x,y) = \sum_{x=0}^{M-1}\sum_{y=0}^{N-1} F(k,j)e^{i\left(\frac{kx}{M}+\frac{jy}{N}\right)} \tag{2.21}$$

The result is a complex $M \times N$ matrix, whose complex part is ignored.

The efficient *Fast Fourier Transform*(FFT) algorithm is used to calculate the DFTs, which reduces the computational costs significantly over the longer explicit calculation.

IDEAL CONDITIONS The DFT and CFT of a function $g(x,y) : \mathbb{R}^2 \rightarrow \mathbb{R}$ over a support $D \in \mathbb{R}^2$ are exactly the same if:

- $g(x,y)$ is continuous and derivable in $\mathbb{R}^2$, avoiding leakage (see section 2.8.2;
- $g(x,y)$ is periodic, so the only error in the approximation (provided the sample is a whole multiple of the period) is due to the aliasing effect. Formula 2.20 implicitly requires periodicity.
- $g(x,y)$ is band-limited, so that there is a sampling frequency f that avoids aliasing (Nyquist theorem).

2.8 PROBLEMS LINKED TO SAMPLING AND WINDOWING

When the DFT is used as a numerical approximation to the Fourier transform of an underlying continuous function, some differences can be expected between the two. For example, it is clear that the DFT can only give the Fourier transform values at the N discrete points for which the computation is done. However, even at these points there may appear in some cases quite significant discrepancies. This is not a result of rounding errors in the calculations, which are normally quite insignificant. The main reason for these discrepancies resides in the discrete and finite nature of the DFT, which implies that the underlying continuous function must be sampled, and that it can only be considered within a finite range. Both of these two operations, sampling and finite-range windowing (or truncation), are inherent to DFT. Each of these operations involves some loss of data, and introduces its own discrepancy between the values obtained by DFT and the true values of the CFT. These two types of error, both considered as DFT artifacts, are named respectively *aliasing* and *leakage* [1].

2.8.1 Aliasing

Aliasing is a phenomenon which may occur due to the discretization (sampling) of the underlying input function. In fact, aliasing is not only limited to DFT applications, and it may be encountered wherever sampling is used, whether or not the sampled data is then subjected to DFT. Discretizing an analog signal requires that the signal's value be sampled often enough to define the waveform unambiguously.

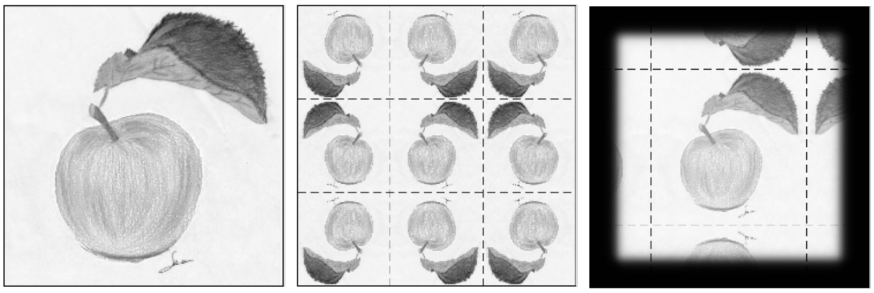

(a) Original image **(b)** Overturning **(c)** Image after overturning and windowing

Figure 18: Overturning and windowing

The Nyquist-Shannon theorem states that given a continuos function $g(x)$, bandlimited with a maximum frequency f_{max}, the original signal can be perfectly reconstructed if sampled with a sampling frequency f_s:

$$f_s \geq 2f_{max} \tag{2.22}$$

f_s is the so called *Nyquist frequency*.

In other words, there must be at least two samples per cycle for any frequency component of the signal. If the sampling points are not taken as densely as required (undersampling), they will fail to follow the high-frequency fine details of the signal, thus leading to aliasing. In the signal domain this is expressed by the existence of a smoother, lower-frequency signal, known as *alias*, which can be traced through all the sampled points and "mimic" or "masquerade" the behavior of the original signal on its sampled values. Only based on these too far-apart sampling points, the original signal is undistinguishable from its lower-frequency aliased signal, since both of them coincide on all of these sampling points.

The aliasing phenomenon can be also interpreted from the viewpoint of the spectral domain. If the condition given by the sampling theorem it is not satisfied, false lower frequencies, known as *aliased frequencies*, will appear.

In the case under analysis, the transfer function method has the aim to reconstruct the energy flux in the real domain, not in the Fourier domain. This permits to ignore the condition to avoid aliasing in the Fourier domain: supposing to measure a gaussian profile without respecting the Nyquist-Shannon condition, the Discrete Fourier Transform obtained is not a good approximation of the continuos transform but, anti-transforming it, the observed and sampled profile can be exactly reconstructed.

2.8.2 Leakage

Leakage is a frequency-smearing artifact that may occur in the DFT spectrum due to the finite-range truncation of the underlying signal. This truncation operation can be viewed as a multiplication of the underlying function $g(x)$ by a rectangular "truncation window" $w(x)$ whose length equals the sampling range length $R = N\Delta x$. From the viewpoint of the signal domain, this truncation may cause a discontinuity between the last and the first elements of the input array (because data is considered by the DFT as cyclical), and thus introduce into the DFT spectrum new high frequencies that do not exist in the original signal.

From the viewpoint of the spectral domain, by virtue of the convolution theorem, the signal-domain multiplication of $g(x)$ with $w(x) = \mathrm{rect}(x/R)$ causes in the frequency domain a convolution of the original Fourier transform $G(u)$ with the Fourier transform of the truncation window $w(x)$. Since the DFT operates on the truncated version of $g(x)$, and thus yields discrete samples of $G(u) * W(u)$ rather than discrete samples of $G(u)$. This is the origin of the leakage artifact in the DFT output.

To avoid this phenomenon, it is necessary that every point at the edge of the domain has the same value.

Windowing and overturning

Taking into account a generic function $g(x,y) : \mathbb{R}^2 \to \mathbb{R}$ continuos on $\mathbb{R}^2$; considering a rectangular domain $D \in \mathbb{R}^2$ and sampling the function on this domain the aim is to obtain the better approximation of CFT with the DFT applied on D.

The DFT considers $g(D)$ as a periodic function in $\mathbb{R}^2$ with period D. If the function is not actually periodic on D some discontinuities may appear. To remove this edge effects, $g(D)$ must have the same value in all points of D edges. This can be obtained applying a window function $w(D)$ that smooth $g(D)$ near the edges.

Using a window function, discontinuities become negligible but the function's characteristics change near the edges. To solve this problem an *overturning* of the image is performed.

This method is showed in Fig. 18.

3 METHOD

3.1 THE ANTI-TRANSFER FUNCTION

As shown in the previous chapter, the linearity of the system represented by the CFC tile in the considered experimental conditions allows the application of transfer function analysis. Using the same notation as above, the essential relation of the analysis is:

$$U_t(k,j) = \frac{V_t(k,j)}{2\pi F_t(k,j)} =: G(k,j)V_t(k,j) \tag{3.1}$$

$G_t(k,j) := (2\pi F_t(k,j))^{-1}$ is the **anti-transfer function** of the tile in the Fourier domain.

To determine $G_t(k,j)$ a program has been developed and run for different two-dimensional temperature profiles to reconstruct the generating energy profiles:

- simulated data: data created with COMSOL whose energy profiles and temperature profiles are known, used to validate the method;
- experimental data: data from the LHD experiment to determine beamlet characteristics.

3.2 THE IMPULSE RESPONSE

To determine the impulse response of the CFC tiles, laser simulations in COMSOL have been employed: a laser impinges on the front side of the tile producing a temperature profile on the rear side. The laser is what better approximates the Dirac delta, since it concentrates all the input energy in a small spot. The temperature output on the rear side of the tile represents the impulse response of the system.

The simulated energy flux profile (F_0) is represented by a gaussian function:

$$F_0 = u^\delta(x,y) = A_u \cdot e^{-\ln 2\left(\left(\frac{x-x_c}{\Gamma_x^u/\chi x}\right)^2+\left(\frac{y-y_c}{\Gamma_y^u/\chi y}\right)^2\right)} \tag{3.2}$$

corresponding to a laser centered in (x_c, y_c), with a power $P = 100\ W$ (this power produces a ΔT on the rear side comparable to the experimental data) and half width at half maximum $\Gamma_x^u = \Gamma_y^u = 1.5\ mm$. χ represents the conversion factor from pixels to millimeters.

The temperature profile on the rear side (T_0) is represented by a modified Hubbert function [21], whose parameters are obtained by fitting the output of the laser simulation:

$$T_0 = v^\delta(x,y) = A_v\left(\cosh\sqrt{(x-x_c)^2b^2+(y-y_c)^2d^2}\right)^{-r} \tag{3.3}$$

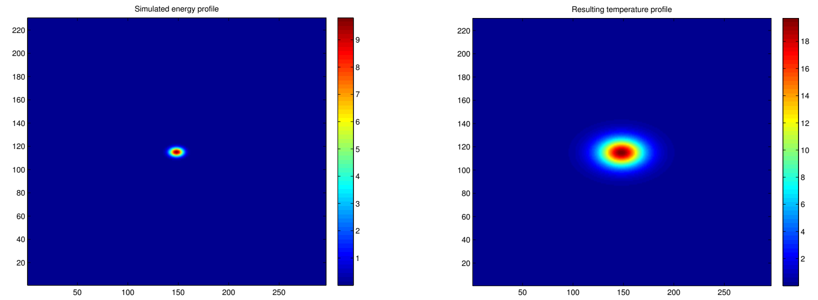

(a) energy flux $[W/mm^2]$ **(b)** Temperature profile [K]

Figure 19: The simulated energy flux profile on the front side and the resulting temperature profile on the rear side

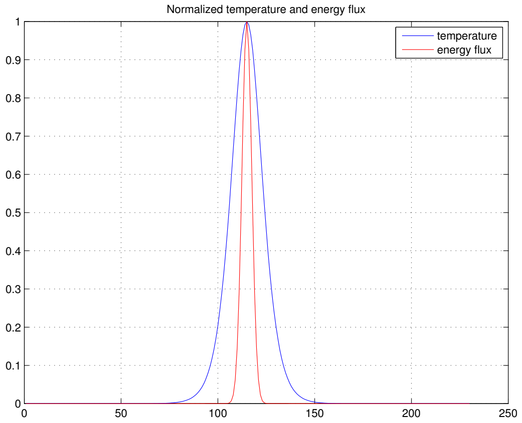

Figure 20: Comparison between the normalized temperature and energy flux profile

b and d depend on the half width at half maximum Γ^v, with the following relations:

$$b = \frac{\operatorname{arccosh}(2^{1/r})}{\Gamma_x^v/\chi_x} \qquad d = \frac{\operatorname{arccosh}(2^{1/r})}{\Gamma_y^v/\chi_y}$$

Fig. 19 shows the input energy flux and the resulting temperature profile on the rear side of the tile.

The anti-transfer function is given by the ratio of the Fourier transforms F_0 and T_0.

For any given temperature profile (T) at instant τ, the energy flux (F) can be calculated as follows:

$$F(\tau) = fft^{-1}\left(\frac{fft(F_0)}{fft(T_0(\tau))} \cdot fft(T(\tau)) \cdot filter\right) \tag{3.4}$$

The choice of the filter will be discussed in a dedicated section later.

3.3 SIMULATED DATA

The method described in the previous section has been tested using simulated data. These data are created with the finite element analysis and

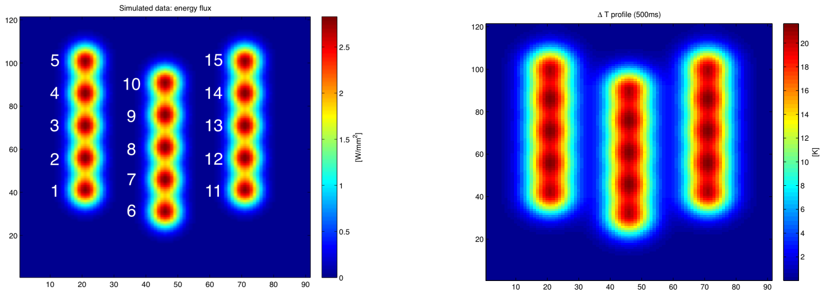

(a) energy flux **(b)** Temperature profile at 500 ms

Figure 21: Simulated energy flux profile on the front side and corresponding temperature profile at 500 ms on the rear side

solver software COMSOL [6] (the thermal properties of the CFC tiles are known) and approximate the real experimental ones: 15 beamlets (represented by gaussian functions) impinge on the front side of the tile, producing a temperature profile on the rear side as shown in Fig. 21. The beamlets are identified by numbers, as the same figure shows. Working with simulated data allows the test of the performance of the method, as both the input and the desired output are known. The simulation parameters, chosen to be as close as possible to the experimental conditions, are:

- input power of each beamlet: $P_{beamlet} = 300\ W$;
- conversion factor: $\chi_x = \chi_y = 1\ mm/pixel$;
- gaussian half width at half maximum: $\Gamma_x^u = 4\ mm$ and $\Gamma_y^u = 6\ mm$;
- pulse duration: 1 s;
- initial temperature of the tile: 300 K;
- vertical distance between the beamlets: $\Delta y = 15\ mm$;
- horizontal distance between the beamlets: $\Delta x = 20\ mm$;

3.3.1 Results

The power and the beamlet amplitude of the reconstructed flux are compared to the real ones to evaluate the method.

The total power impinging on the tile is $P_{tot}^{real} = 15 \cdot 300 = 4500\ W$. Considering beamlet 1, the total amplitude is given by the sum of the amplitude of the gaussian function centered in 1 and the influence of the gaussian function representing beamlet 2:

$$\begin{aligned} A_u^{tot} &= A_u^{real} + A_u^{real} e^{-\frac{\Delta y^2 \cdot \ln 2}{\Gamma_y^2}} \\ &= \frac{P_{beamlet}}{2\pi\Gamma_x^u\Gamma_y^u} 2\ln 2 \left(1 + e^{-\frac{\Delta y^2 \cdot \ln 2}{\Gamma_y^2}}\right) \\ &= 2.7942\ [W/mm^2] \end{aligned} \tag{3.5}$$

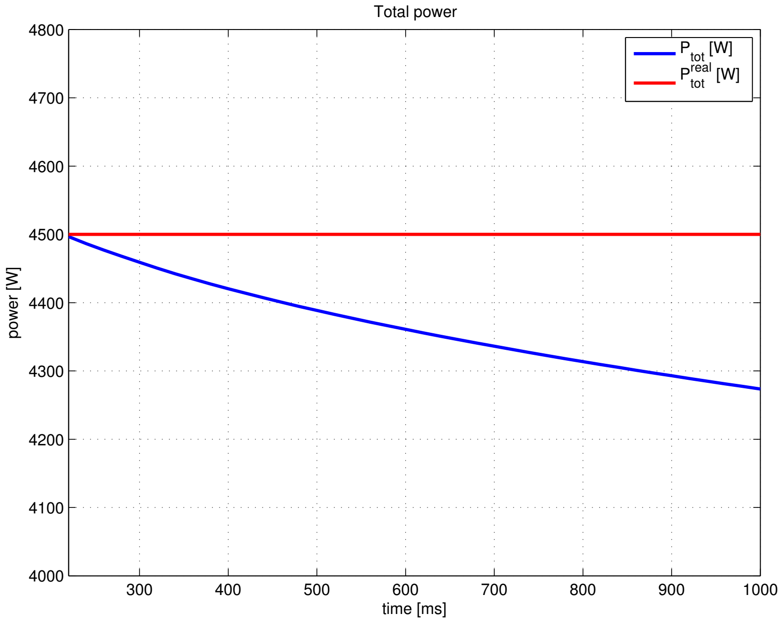

Figure 22: Reconstructed total power compared to the real one as function of time

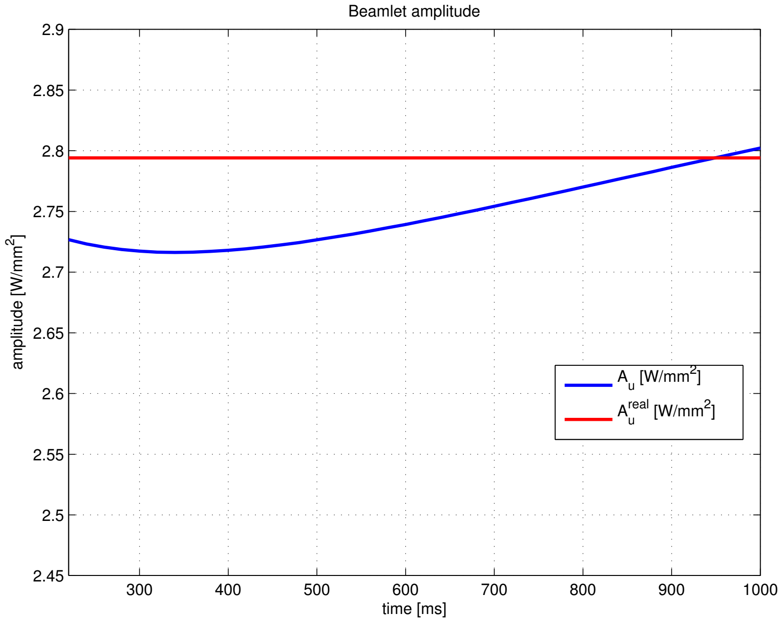

Figure 23: Reconstructed amplitude of beamlet 1 compared to the real one as function of time

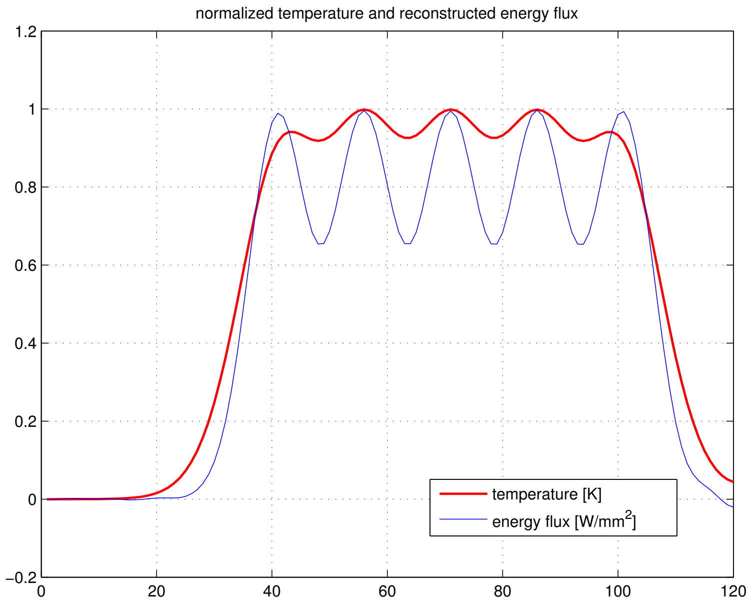

Figure 24: Normalized temperature and energy profiles along the third column

In this case the optimal filter parameter for the inversion from the temperature profile to the energy flux is used, which is a cut off length $cut_f = 4\ mm$ (this filter choice will be discussed in details in section 3.3.3) and the results are shown in Fig. 22 and Fig. 23. The total power reconstruction error is below 10%, and the beamlet 1 amplitude error is below 5%.

The estimate of the flux is smaller than the real value and decreases with time. This phenomenon is caused by the small error in approximating the tile material as linear, as the flux is expected to be constant.

In fact, this method assumes a linear system, and although there is an error, the CFC is close enough to linear for its performance to be well within the acceptable range.

Fig. 24 shows the normalized temperature and energy flux profiles along the third column; note that the number and positions of the beamlets are correctly identified.

The temperature peaks at the extremities are lower than the others because there is a peak on only one of their sides. The flux peaks all have the same value instead, as the contribution of the near peaks are almost insignificant on the front side.

Linear material

It has been verified that the cause of the variability of the flux over time was the non linearity of the material by running another simulation with a perfectly linear material. Both the laser simulation used to calculate the transfer function and the simulated data consider a perfectly linear material.

Results are shown in Fig. 25 and Fig. 26.

In this case, the total power reconstruction error is below 2%, and so is the beamlet 1 amplitude error.

This way, it has been demonstrated that the error, however small, is indeed caused by the non perfect linearity of the tile's material.

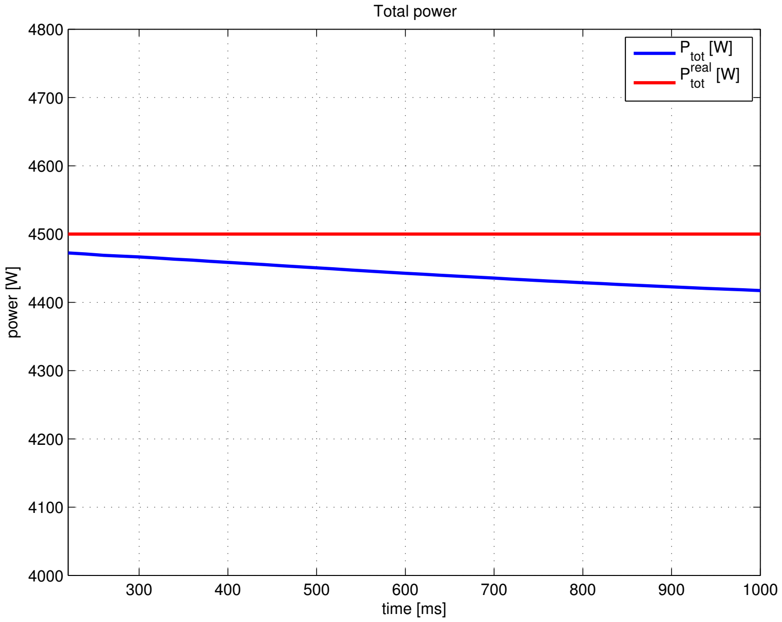

Figure 25: Reconstructed total power compared to the real one as a function of time for linear data

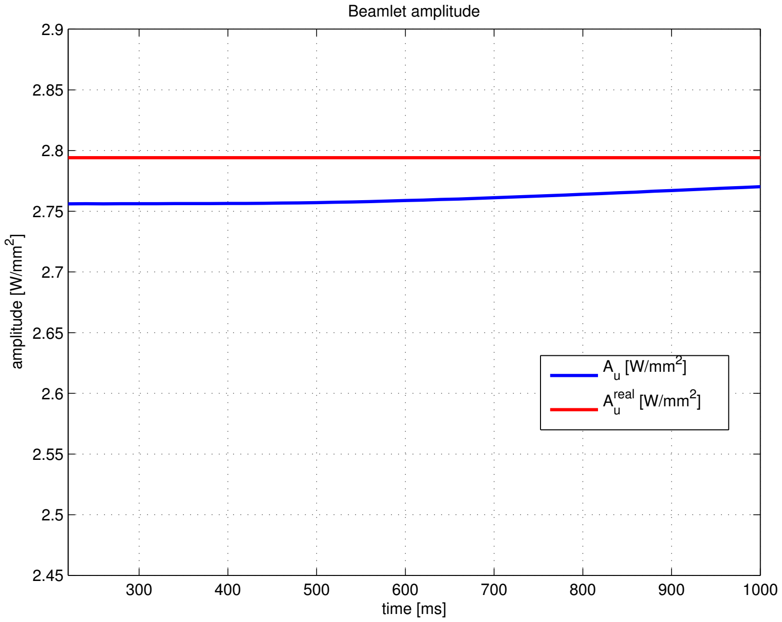

Figure 26: Reconstructed amplitude of beamlet 1 compared to the real one as a function of time for linear data

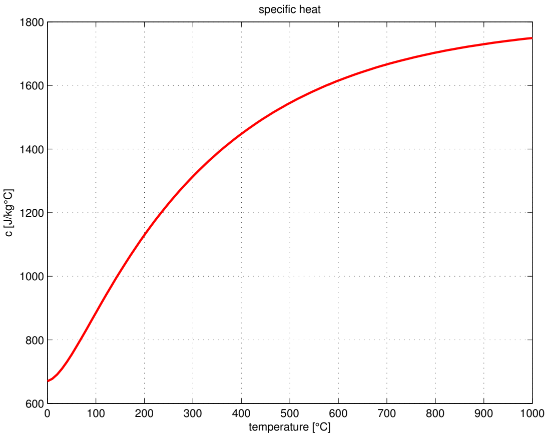

Figure 27: Specific heat

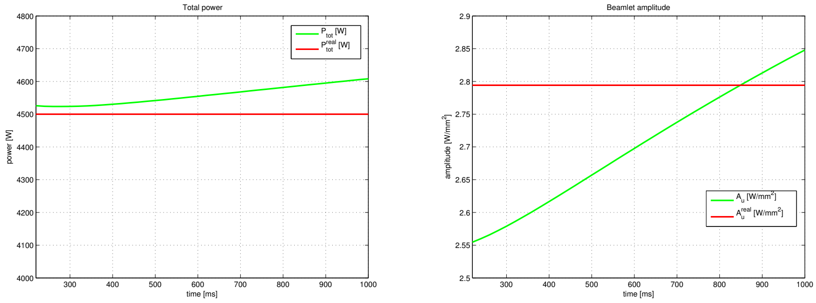

(a) Total power

(b) Beamlet amplitude

Figure 28: Reconstructed total power and beamlet 1 amplitude using specific internal energy compared to the real ones

3.3.2 Internal energy

To reduce the influence of non linearity in the reconstruction, the energy flux is derived from the specific internal energy instead of the temperature.

The specific internal energy of the tile is defined as:

$$e_{int} = c \cdot T \; [\frac{J}{kg}] \tag{3.6}$$

where c is the specific heat of the tile and T is the temperature. The dependence on the temperature of the specific heat, shown in Fig. 27, is given by the empirically derived equation 2.15.

The specific internal energy on the rear side is represented by the same Hubbert functions as temperature, but with different parameters, obtained from the laser simulation (which also used specific internal energy instead of temperature).

The used filter cut off length is $cut_f = 6\ mm$, because, as shown in the next section, this is the optimal parameter for the inversion with specific internal energy.

The reconstructed total power and beamlet 1 amplitude, compared to the real values, are shown respectively in Fig. 28a and Fig. 28b.

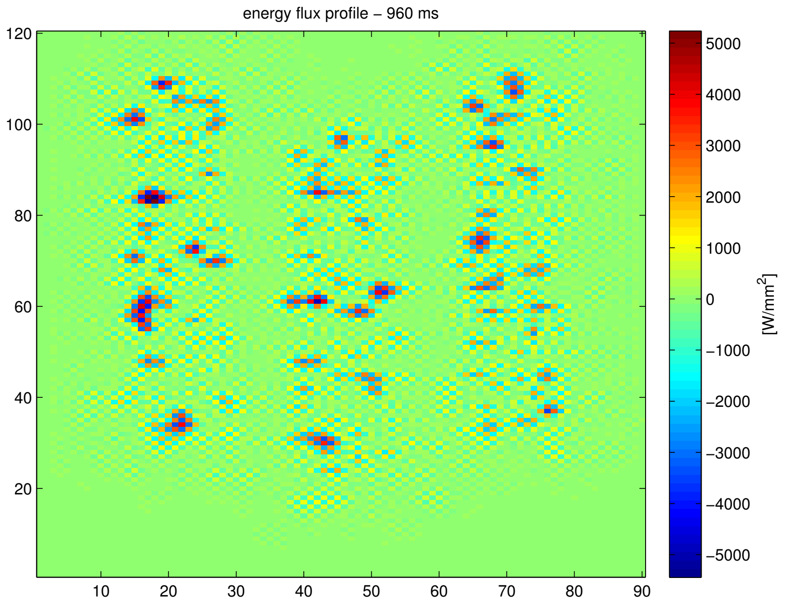

Figure 29: Reconstructed flux without low-pass filter

Comparing the results with the inversion using temperature, the total power is overestimated and increasing with time; however, the maximum error is below 3%. The error in the reconstruction of the beamlet 1 amplitude is higher, with a maximum error is below 10%.

3.3.3 Filtering

Deriving the energy flux from the temperature profile (or specific internal energy) is conceptually equivalent to high pass filtering; the peaks at higher frequencies can hide the relevant phenomena, as Fig. 29 shows.

In order to avoid this, it is needed to filter the flux profile with a low pass filter using a bi-dimensional Fermi filter; this procedure also eliminates high frequency noise. The filter is defined as:

$$D(k,j) = \frac{1}{1+\exp\left(\frac{\sqrt{k^2+j^2}-\eta}{s}\right)} \tag{3.7}$$

where k and j are the projections of the x and y axes on the Fourier domain, η is the cut off frequency of the filter and s is the "speed" of the filter. The Fermi filter was chosen among other alternatives (for example a Butterworth filter) because of its exponential trend, which matches the transfer function.

The cut off length of the filter was optimized both from temperature and specific internal energy by investigating the dependence of the energy flux and comparing results with real data.

It can be noticed from Fig. 30 that the reconstructed power can be considered independent from the filter cut off value for all practical purposes; the beamlet 1 amplitude varies within 30% of the nominal value instead, as Fig. 31 shows.

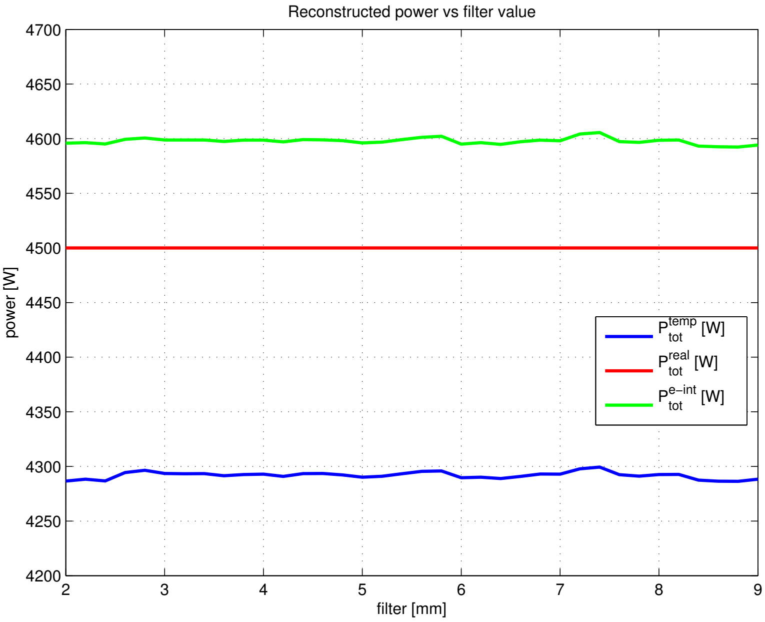

Figure 30: Reconstructed power as a function of the cut off filter value

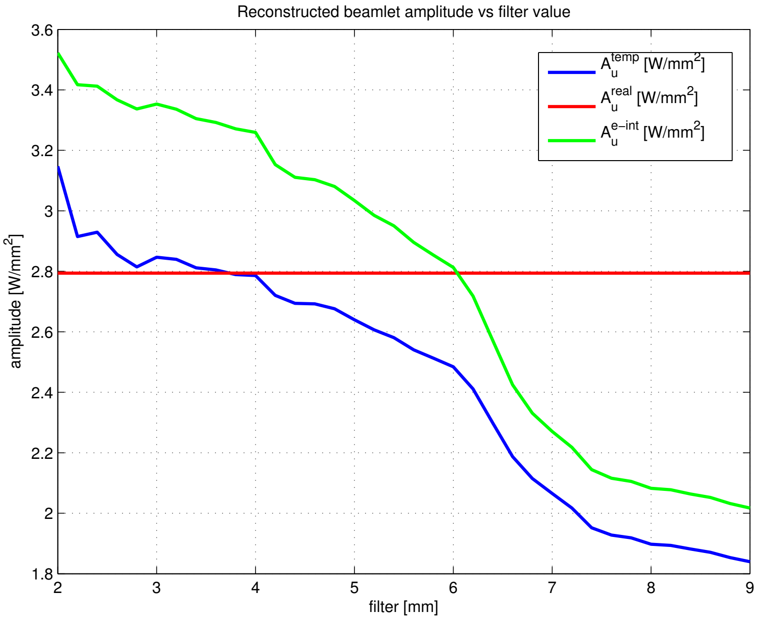

Figure 31: Reconstructed beamlet amplitude as a function of the cut off filter value

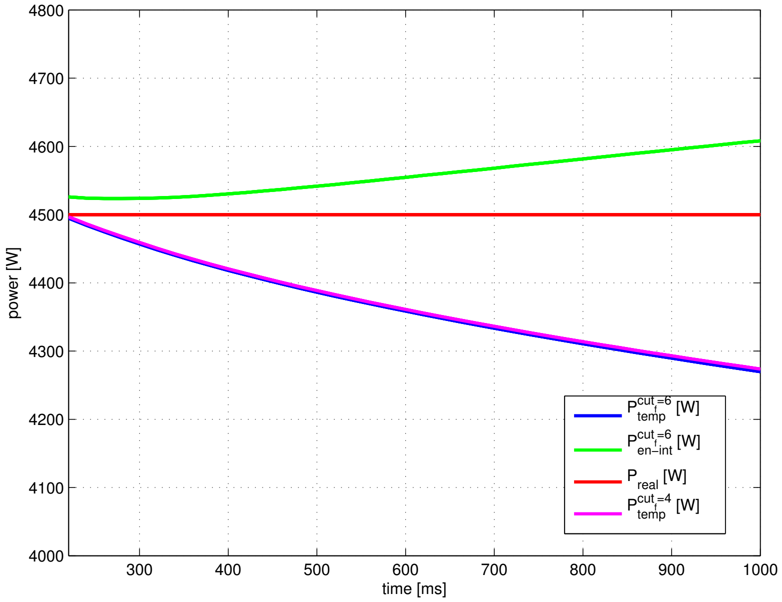

Figure 32: Reconstructed power comparison between temperature and specific internal energy at different filter values

As section 4.1 will explain in detail, the value $cut_f = 4\ mm$, i.e., the optimal value for the inversion with temperature that guarantees the better reconstruction of the beamlets amplitude, can not be used for experimental data, while $cut_f = 6\ mm$ is a reasonable choice.

Fig. 32 shows the reconstructed power with the temperature inversion at the two different cut off filter values ($cut_f = 4\ mm$ and $cut_f = 6\ mm$) and the reconstructed power with the specific internal energy inversion at $cut_f = 6\ mm$. As previously said, the total power does not depend on the cut off length, but the error in reconstruction using specific internal energy is, in any case, smaller than using temperature. Fig. 33 shows the reconstructed beamlet 1 amplitude in the same conditions. In this case, the absolute error is smaller with the inversion of the temperature with $cut_f = 4\ mm$; however, since this value is not applicable to the experimental data, only the results with $cut_f = 6\ mm$ must be considered. When this cut off filter value is used, the error with the temperature inversion (blue line) is always greater than the error with the specific internal energy inversion (green line).

In conclusion, using specific internal energy in the inversion provides better performance than the temperature in the reconstruction of both the total power and beamlet amplitude when the same filter is used as for the experimental data. Fig. 34 shows the final result of the application of the method to simulated data: on the left-hand side (Fig. 34a) is represented the temperature increasing profile on the rear side and on the right-hand (Fig. 34b) the corresponding reconstructed energy flux profile.

Beamlets of greater dimensions

n order to take into consideration the variety of cases that can be encountered throughout the experimental campaign, the study of the optimal cut off filter length has been repeated considering beamlets of greater

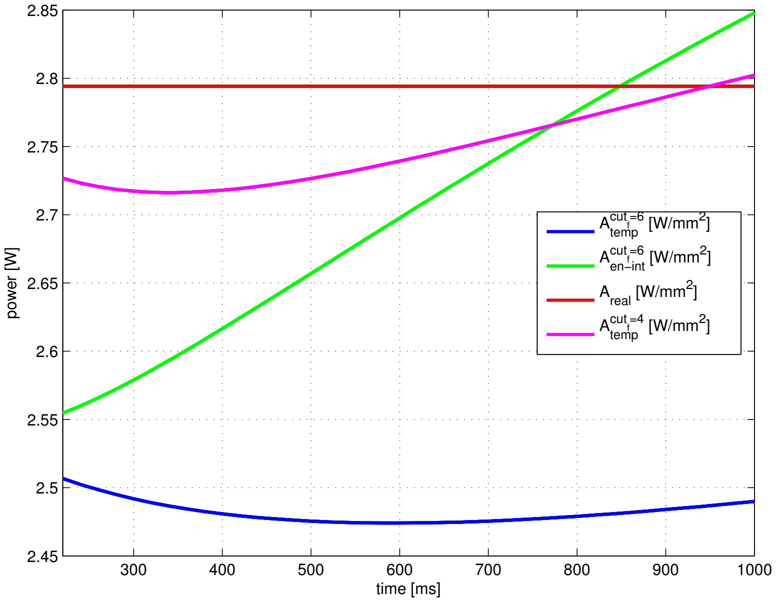

Figure 33: Reconstructed beamlet amplitude comparison between temperature and specific internal energy at different filter values

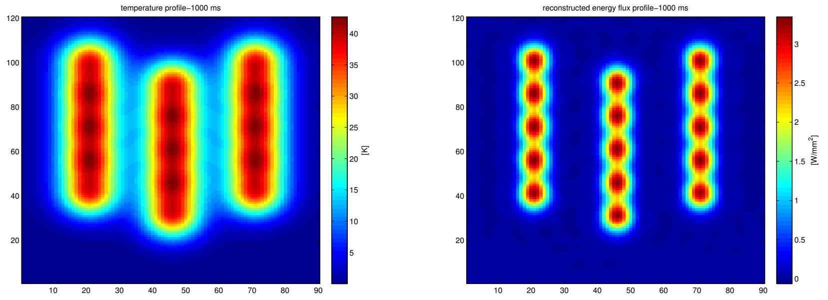

(a) Temperature profile

(b) Reconstructed energy flux profile

Figure 34: Final result of the method applied to simulated data

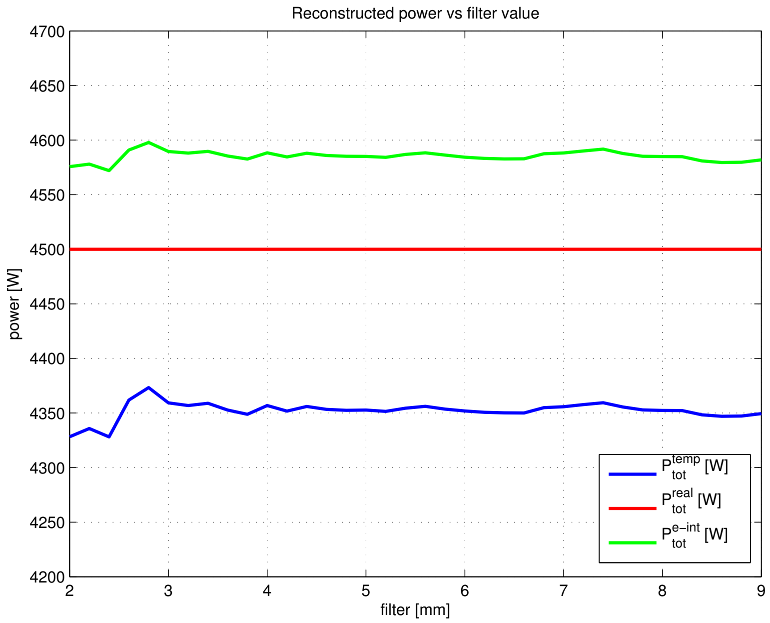

Figure 35: Reconstructed power as a function of the cut off filter value for beamlets $8 \times 6\ mm$

dimensions: $\Gamma_x^u = 8\ mm$ and $\Gamma_y^u = 6\ mm$, while the rest of the parameters have remained unchanged. The beamlet 1 total amplitude is then $A_u^{tot} = 1.4170\ [W/mm^2]$: since the power of the single beamlet is the same as in the case of beamlets with dimensions $4 \times 6\ mm$, if the width increases (and thus so does the beamlet area), the amplitude has to decrease.

Fig. 35 shows the total power as a function of the filter cut off length for the reconstruction both with temperature and specific internal energy. As for the previous case, it is independent of the filter value for both types of anti-transfer function. Using the temperature profile the total power is underestimated of about 3%; on the contrary, using the specific internal energy it is overestimated and the error is about 2%.

The beamlet 1 reconstructed amplitude is shown in Fig. 36. In this case the optimal filter value computing the anti-transfer function with temperature is still around 4, but, as previously said, this value is not applicable to the experimental data since it produces severals spurious peaks. With $cut_f = 6\ mm$ the error introduced is 4%. If the anti-transfer function is computed with the specific internal energy, the optimal value for the filter cut off length is $7\ mm$, however, as it will be explained in detail in section 4.1, for the experimental data this is not a suitable value since it reduces too much the amplitude of the beamlets while enlarging them at the same time. The error using $cut_f = 6\ mm$ is 4.9%.

In conclusion, if the beamlets have a bigger area and the filter has a cut off length $cut_f = 6\ mm$, the inversion using the specific internal energy gives better results than using the temperature in the reconstruction of the total power (see Fig.37a), while the reconstruction of the beamlets amplitude is almost equivalent (see Fig. 37b).

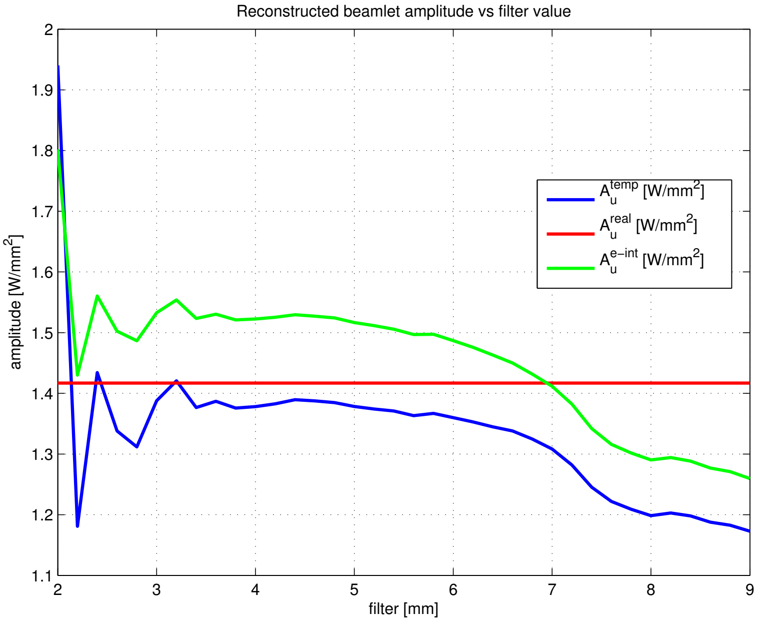

Figure 36: Reconstructed beamlet amplitude as a function of the cut off filter value for beamlets 8 × 6 *mm*

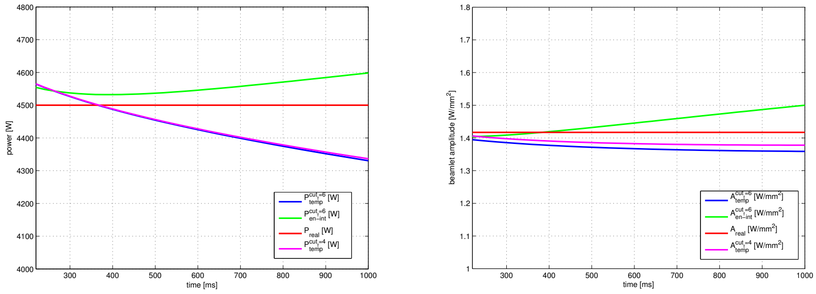

(a) Total power

(b) Beamlet amplitude

Figure 37: Reconstructed total power and beamlet amplitude comparison between temperature and specific internal energy at different filter values for beamlets 8 × 6 *mm*

4 EXPERIMENTAL DATA

In the previous chapter the optimal conditions for the analysis of the experimental data have been examined, however there are some peculiar adjustments necessary when working with real data, which can not be investigated with simulated data; they will be discussed in this chapter.

Experimental data are the thermographic images from mini-STRIKE, the prototype of the SPIDER diagnostic calorimeter, installed inside the test stand of the neutral beam injectors of the LHD experiment at National Institute for Fusion Science (NIFS) in Toki (Japan) [22].

Every image, i.e. Fig. 38, represents the temperature increase profile on the rear side of the 1D-CFC tile since the beginning of the pulse. Every pulse lasts $1\ s$ so, since the infrared camera records with a inter-frame interval of $40\ ms$, 25 frames per pulse are recorded.

The method has been applied to some experimental campaigns of the NIFS experiments to analyze the beamlet characteristics as functions of ion source and beam parameters. The parameters that can vary are:

- the extraction potential V_{ext}
- the acceleration potential V_{acc}
- the extracted current I_{ext} and consequently the arc power P_{arc}.

For each pulse, two parameters are essentially fixed and the third varies, so the dependence on this parameter of the beam characteristics can be investigated.

4.1 FILTERING

As previously said in section 3.3.3, a low pass filter is necessary to prevent high frequencies from hiding relevant information. The filter used for the experimental data is the bi-dimensional Fermi filter already used for the simulated data. To identify the optimal value of the cut off filter length, several anti-transfer functions with different values have been computed in an interval from $cut_f = 3\ mm$ to $cut_f = 9\ mm$ and step of $0.2\ mm$.

A first visual analysis of the images of the reconstructed flux allows to exclude all values in the intervals $cut_f = 3 \div 5\ mm$ and $cut_f = 8 \div 9\ mm$. In the first interval the filter is insufficient and high frequencies, especially in the zone of the thermocouple shadow, hide the relevant information as Fig. 39a shows; in the second interval the filter is too heavy: reconstructed energy flux has a poorer resolution even than the temperature profile and the beamlets are not well distinguishable from each other (see Fig. 39b).

The interval $cut_f = 5 \div 8\ mm$ has been analyzed more in detail as explained.

As for the simulated data, the reconstructed total power turns out to be almost independent from the filter cut off value (see Fig. 40) while the maximum beamlet amplitude decreases as the filter value increases (see Fig.

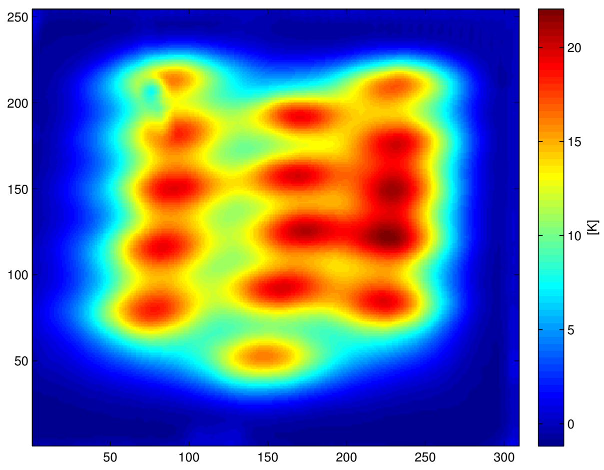

Figure 38: Example of a thermal camera image

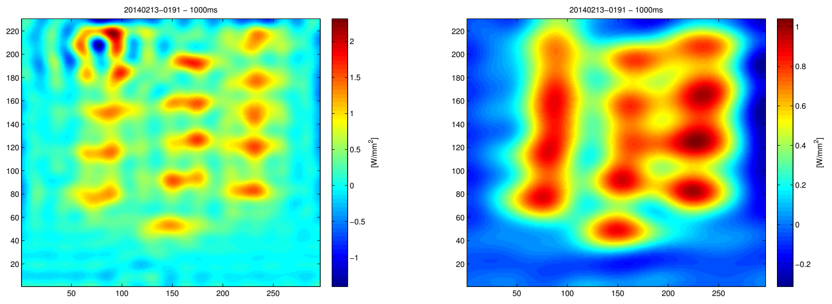

(a) Inversion with $cut_f = 4\ mm$

(b) Inversion with $cut_f = 9\ mm$

Figure 39: Reconstructed energy flux with cut off filter values of 4 mm and 9 mm

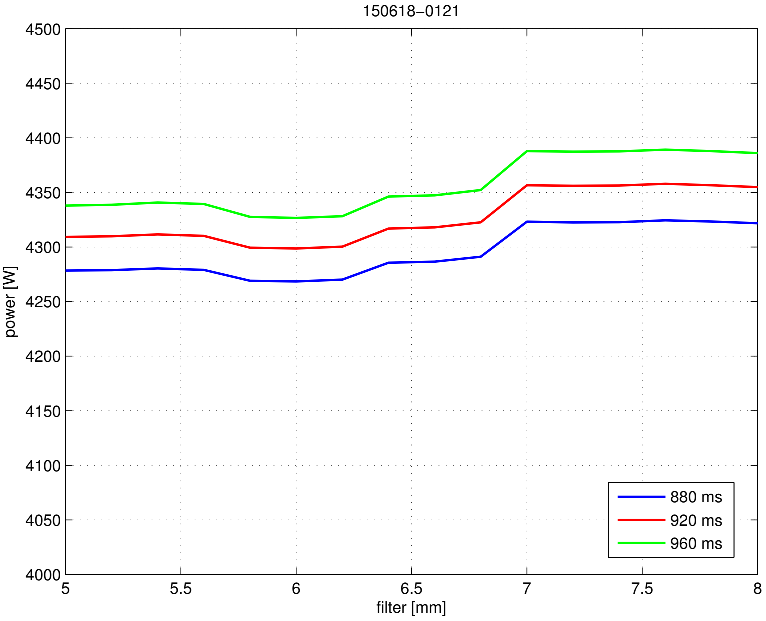

Figure 40: Reconstructed total power vs filter value

41). From these figures it can be also deduced that the reconstructed total power, and consequently the amplitude, is slightly increasing with time. Theoretically the power should be constant in time considering that the anti-transfer function is calculated at each instant with the right parameters, but, since the material is not perfectly linear as the hypothesis would require, this occurs. However, the increase is less than 1% at any frame and so it is totally acceptable.

Since these considerations are not sufficient to find an optimal value for the filter cut off, the fit on the reconstructed flux have been performed for every filter value to analyze the half width at half maximum of the reconstructed beamlets. Beamlet number 6 is considered because it is the most isolated so it is less influenced by its neighbours. Results are showed in Figs. 42a, 42b,42c. It can be noticed that for a cut_f value lower than 6.4 mm the half width at half maximum (both along x and y axes) is almost constant. When increasing the filter value, the half width at half maximum is expected to rise and the amplitude to decrease. This seems in contradiction with the results shown, but, since increasing the cut off filter value lowers the resolving power and the beamlets are not clearly distinguishable anymore, the fitting program fails in clearly recognizing each single beamlet and neighboring beamlets get mixed up. In fact, considering the average values of all the beamlets, the amplitude decreases, as Fig. 43a shows, and the half width at half maximum increases when increasing cut_f. In particular, the half width along the y axis is slightly increasing at the beginning and then the slope sharply rises (see Fig. 43b) while, at the same time, the half width along x axis starts decreasing (see Fig. 43c). In fact, since the distance between a beamlet and another is greater along the x axis than along the y axis, since increasing the filter value lowers the resolving power, the fit program sees the beamlets elongated along the y direction.

Another verification has been carried out with COMSOL simulations by imposing in input the reconstructed flux with the different cut off values

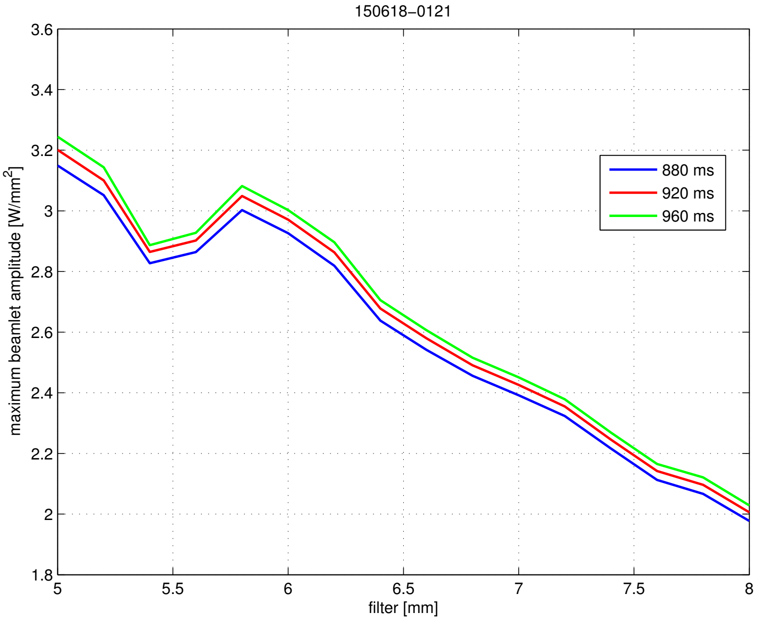

Figure 41: Reconstructed maximum beamlet amplitude vs filter value

and extracting the resulting temperature profile. This temperature profile has been fitted and the fit results are compared with the fit results of the real experimental data.

From all these considerations, the cut off filter length chosen is $cut_f = 6\ mm$, because this value represents the optimal compromise between good resolving power and not too a heavy filter. Fig. 44 represents the temperature profile along the third column of beamlets obtained from the COMSOL simulation with this filter value along with the real experimental one. It can be noticed that the temperature increase resulting from the reconstructed flux is a little bit smaller than the real one, but the two profiles are almost equivalent since the maximum error is below 4%. Moreover, the effect of the filter can be seen: the temperature profile resulting from the simulation is "clean" and it does not have all the little oscillations of the experimental one.

All these analyses were performed with the inversion both both with the inversion using the temperature and using specific internal energy, leading to the same optimal filter cut off length.

4.2 INFLUENCE OF NON LINEARITY

The 1D-CFC, as previously said, is not a perfectly linear material and the specific heat does not exhibit a constant value (see Fig. 27) with respect to the temperature. Moreover, the temperature increase on the front side of the tile is much higher than the one on the rear side. The initial temperature of the tile must be taken into account, so several laser simulations, necessary to calculated the transfer function with the correct parameters, are performed to match in a better way the real initial conditions of the tile for each pulse.

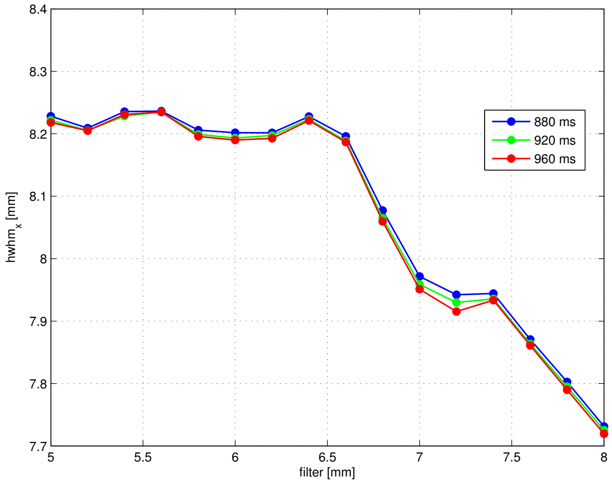

(a) Beamlet 6 half width at half maximum along x axis

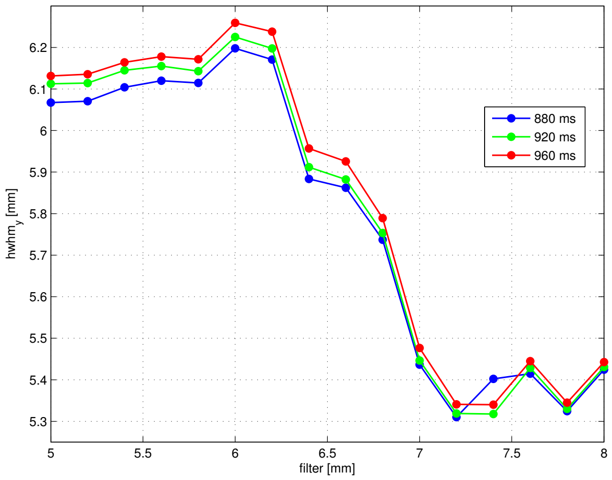

(b) Beamlet 6 half width at half maximum along y axis

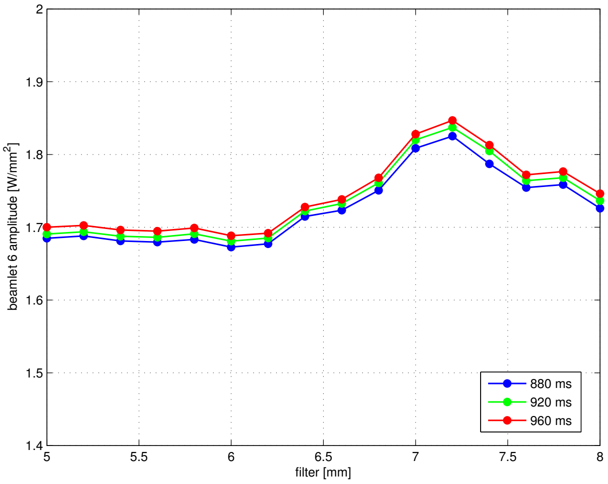

(c) Beamlet 6 amplitude

Figure 42: Amplitude and half width at half maximum of reconstructed beamlet 6 as a function of the filter value

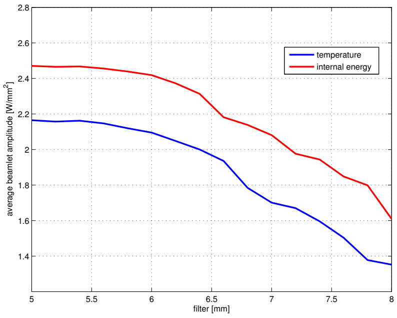

(a) Amplitude

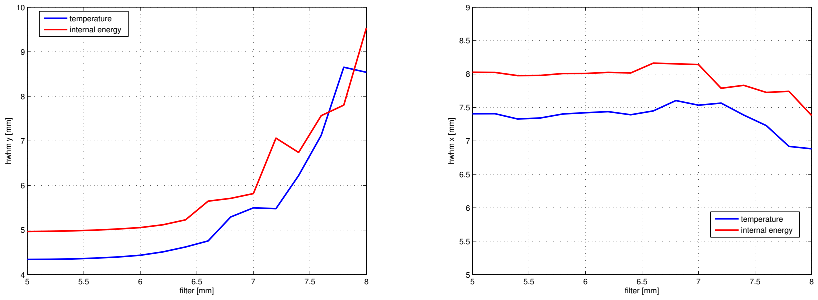

(b) Half width at half maximum along y axis **(c)** Half width at half maximum along y axis

Figure 43: Average reconstructed beamlet amplitude and half width at half maximum as a function of the filter value

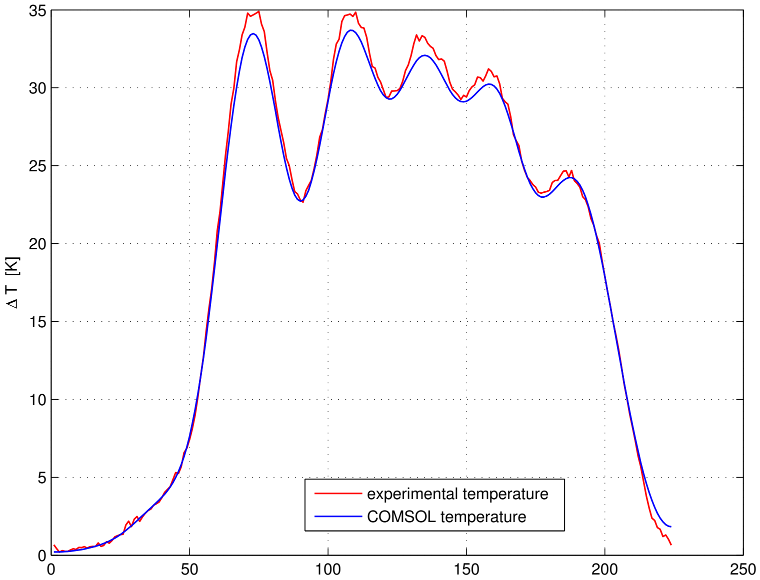

Figure 44: Comparison between the temperature profile obtained with the COMSOL simulation and the experimental one

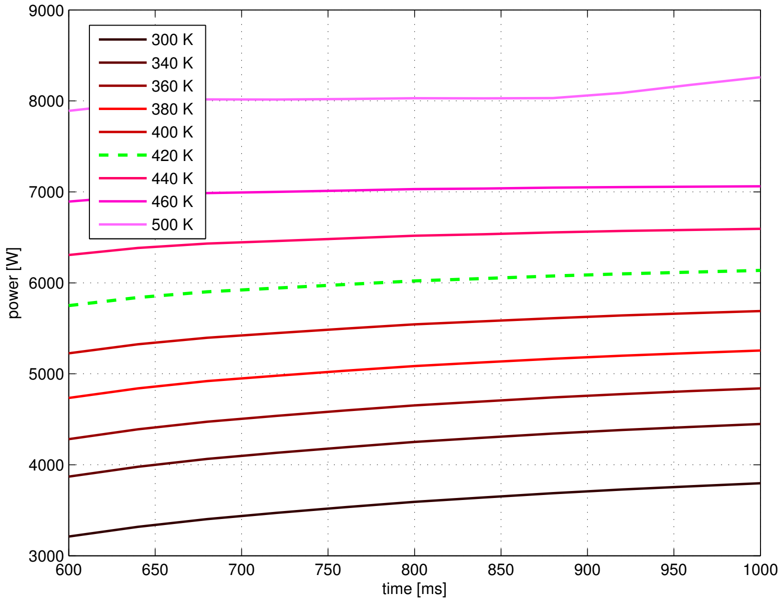

Figure 45: Influence of the initial temperature of the tile in the inversion using the temperature profile

To analyze the influence of the initial temperature, the inversion of each pulse has been performed several times, each time using the parameters of a laser simulation at different initial temperature.

The pulse analyzed is taken from an experimental campaign in which the varying parameter is the extraction potential. The power of the beam impinging on the tile is high, so the temperature substantially increases during the shots. This pulse also has a good optics that allows to clearly recognize each single beamlet and permits a good examination of the beam.

The results by computing the anti-transfer function using the temperature profile are shown in Fig. 45. It is clear that the reconstructed flux is highly dependent on the initial temperature of the tile: knowing that the real initial temperature in the case shown is 419 K, the reconstructed total power varies by about ±40% from the value obtained with the laser simulation at the temperature nearest to the real one (the green dotted line). All the reconstructed power profiles exhibit the same trend as a function of time, but, as the temperature of the simulation increases, the variability of each profile in the same time interval decreases. In fact, in the interval between 600 ms and 1000 ms, the laser simulation at 300 K implies a variation of 18% with the respect to the initial value, whereas at 420 K it is 7% and at 460 K it is 2%.

When computing the anti-transfer function with the specific internal energy, the reconstructed power is less dependent on the initial temperature, as shown in Fig. 46. In this case the reconstructed power deviation from the value obtained with the laser simulation at the nearest temperature is less than ±20%. As for the case with temperature, all the profiles have the same trend and the variability decreases as the temperature of the simulation increases in same measure as in the temperature case.

Since the electrical parameters of the shot are known, a comparison between the reconstructed total power and the electrical power can be done.

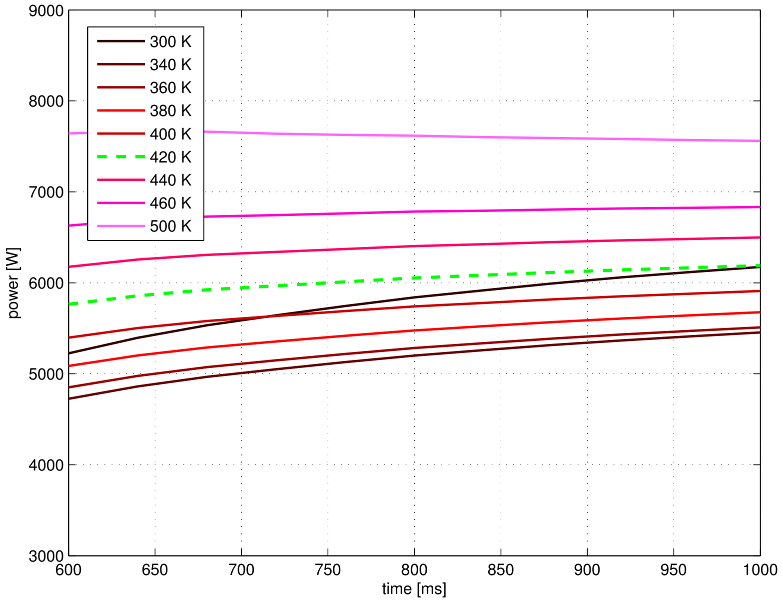

Figure 46: Influence of the initial temperature of the tile in the inversion using the specific internal energy

The extraction potential is $V_{ext} = 4.75\ kV$, the acceleration potential is $49.9\ kV$ and the current measured on mini-STRIKE is $I_{mST} = 0.244\ A$ so the total electrical power impinging on one tile can be calculated as:

$$P_{elec} = \frac{(V_{ext} + V_{acc}) \cdot I_{mST}}{2} = 6667\ [W] \tag{4.1}$$

Comparing this value with the reconstructed total power, yields an error of 8% in the case of the temperature, and of 7.2% in the case of the specific internal energy.

The results once again show that computing the anti-transfer function using the specific internal energy guarantees better performances, because it helps reducing the influence of the non linearity of the material in the reconstruction.

To better investigate the influence of the non linearity of the tile, a pulse in which the maximum temperature increase on the rear side of the tile is less than $12\ K$ is analyzed. Since the ΔT is small, the material can be considered linear and the specific heat varies less than 4% from the beginning to the end of the pulse. In this case the reconstructed total power turns out to be almost constant in time (see Fig. 47): it increases by less than 3% in 280 ms, as expected if the method is applied upon fulfilling all the hypotheses.

The final result of the reconstruction of the energy flux profile using the specific internal energy and the optimal filter value, is shown in Fig. 48.

4.3 EXPERIMENTAL CAMPAIGN

The method, once optimized, has been applied to analyze the data of the experimental campaigns at NIFS. The analysis is performed by computing

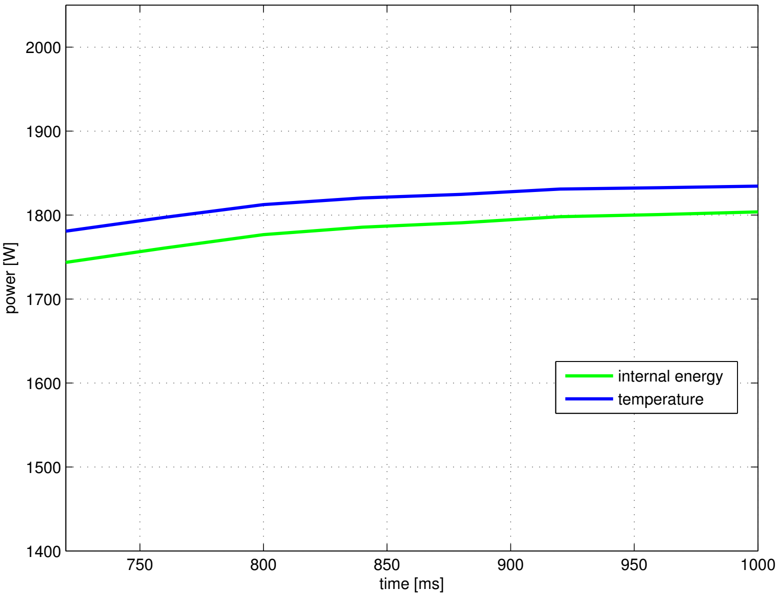

Figure 47: Reconstructed total power in a linear pulse

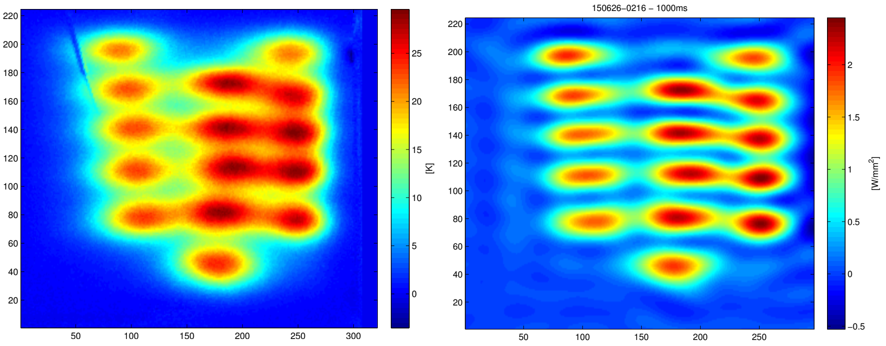

(a) Temperature profile **(b)** Reconstructed energy flux

Figure 48: Final result of the reconstruction of the energy flux profile from a thermographic image

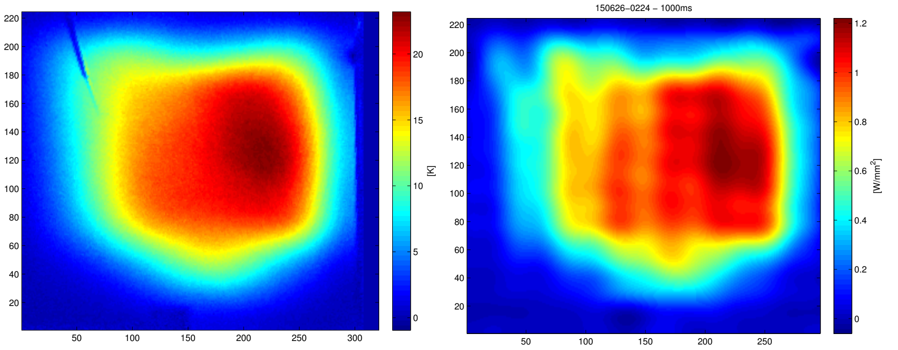

(a) Temperature profile

(b) Reconstructed energy flux

Figure 49: Example of a pulse with bad optics in which the beamlets are not distinguishable from one another

the anti-transfer function to reconstruct the energy flux on the front side for each pulse, fitting the obtained energy flux profile and then comparing the fit results with the fit results of the temperature profile on the rear side.

To guarantee the best results, for the reasons explained in the previous section, the anti-transfer function is computed using the specific internal energy and with a cut off filter length $cut_f = 6\ mm$.

In some pulses, the beamlets are not distinguishable from one another, neither in temperature profile nor in the reconstructed energy flux profile (see Fig. 49), so the fitting program fails in recognizing each single beamlet, even if the beamlets structure is barely distinguishable in the reconstructed energy flux profile. In these cases, the center positions of the beamlets have been kept fixed during the fitting procedure and the area where the program tries to find the center limited, in order to avoid results that do not correspond to the experimental reality.

Every scan studies the dependence of the beam characteristics (amplitude, half width at half maximum and power) on a specific parameter (P_{arc}, V_{acc} or V_{ext}): several shots were done in each of which one parameter changes, while the others remain unchanged.

4.3.1 Arc power scan

The first two scans study the dependence on the arc power. From the theory it is known that increasing the arc power, the number of charge carriers, i.e. I_{ext}, increases and so does the beam power, if the acceleration voltage is held constant. When I_{ext} increases so does the perveance (Eq. 1.6) and consequently, the ratio Π/Π_0 too.

For the first scan the fixed electrical parameters are: $V_{ext} = 4\ kV$, $V_{acc} = 53\ kV$. Fig. 50 shows the normalized average value of the energy flux beamlet amplitude as a function of the arc power. The blue dots (each point corresponds to a pulse) represent the average normalized amplitude of the beamlets of the temperature profile on the rear side of the tile, while the red dots represent the average normalized amplitude of the beamlets of the reconstructed energy flux profile on the front side. It can be noticed that the two almost coincide, with the exception of the first point that can be considered an outlier, since it corresponds to a bad shot in which the beamlets are all mixed up. The beamlet amplitude is directly proportional to the beam power so, the dependence on the arc power is expected to be

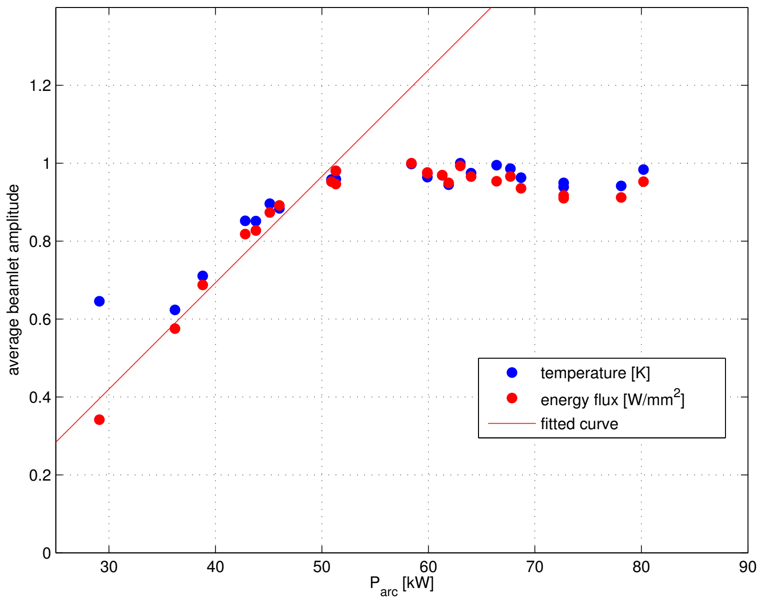

Figure 50: Average beamlet amplitude as a function of the arc power (1^{st} scan)

linear. The points have been fitted with a linear fit of the type $y = ax + b$. In the first part, for $P_{arc} < 55\ kW$, they follow the linear trend but then, for $P_{arc} > 55\ kW$, the amplitude ceases to increase. This is most likely due to the fact that the divergence of the beam increases with the arc power so, when the beam becomes bigger than the extraction grid (EG) apertures, part of the beam hits the EG losing a certain amount of energy. So, even if the arc power increases and also beam power, not all of this power reaches the calorimeter because part of it is lost on the EG. For this reason, the points corresponding to $P_{arc} > 55\ kW$ have been excluded from the fit procedure.

Fig. 51 and Fig. 52 represent the half width at half maximum respectively along the x and y axes, both of the temperature profile (blue dots) and of the reconstructed energy flux (red dots). As previously said in section 1.4.2 the divergence of the beam is expected to have a parabolic trend as a function of the arc power (see Fig. 6), but it is difficult to reach the region beyond the optimum value for technical reasons.

In both figures, the data set have been fitted with a parabolic function, excluding only the outlier point corresponding to $P_{arc} = 29.1\ kW$. It can be observed that the points follow the parabolic trend but it is not possible to clearly see the region where the divergence starts increasing again. This may be due either to the fact that the beam is hitting the EG so the particles with higher divergence are blocked, or to an insufficient maximum arc power. In the first case, the points corresponding to $P_{arc} > 55\ kW$ should be excluded from the fit, but, since the answer is not completely definite yet, they have not been excluded.

The electrical parameters of each shot are known so the beam power can be calculated by Eq. 4.1 and compared to the one resulting from the reconstruction. The results of this comparison are shown in Fig. 53. It can be observed that the two values are very close to each other and this implies that the method based on the anti-transfer function provides a good estimation of the beam power, with an error of about 5%. Moreover it can be

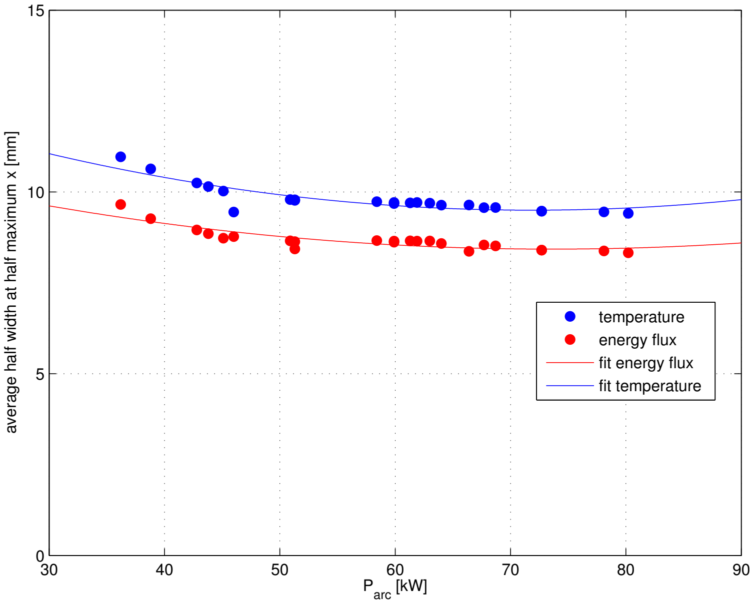

Figure 51: Average beamlet half width at half maximum x as a function of the arc power (1^{st} scan)

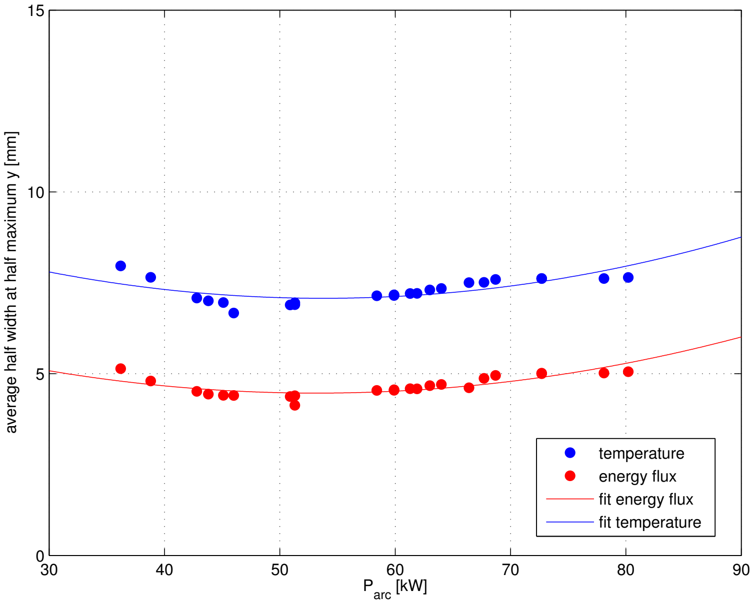

Figure 52: Average beamlet half width at half maximum y as a function of the arc power (1^{st} scan)

noticed that, when $P_{arc} > 55\ kW$, both the electrical and the reconstructed power, are not increasing anymore, even if the arc power continues to increase. This implies that the beam particles did not reach the grounded grid (GG), otherwise the corresponding current would have returned back to the acceleration power supply, but they have been intercepted, most likely by the EG. Furthermore, when $P_{arc} > 60\ kW$, the error in the reconstruction of the beam power increases. A possible explication of this phenomenon is that when the beam power raises, the tile temperature increases and so the material become less and less linear, contrary to the hypothesis of the method. Another possibility is that some particles, once they have passed the EG are intercepted by the GG.

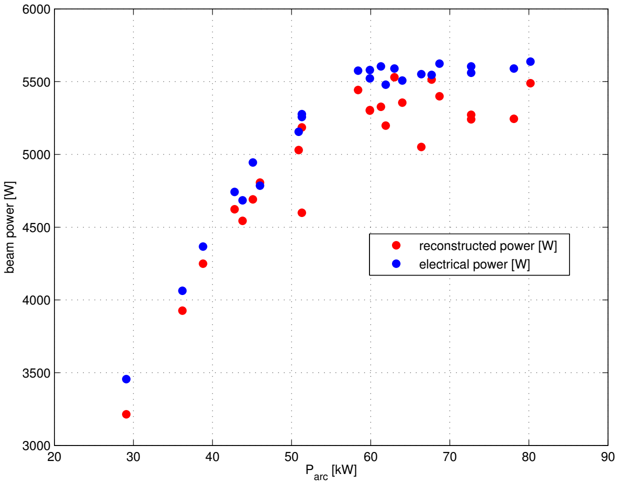

Figure 53: Comparison between the electrical power and the reconstructed power (1^{st} scan)

A second scan of the arc power has been analyzed. In this case the extraction potential is the same as the previous scan, while the acceleration voltage is $V_{acc} = 47.7$.

The value of the normalized average amplitude as a function of the arc power is shown in Fig. 54. The same considerations as for the previous scan can be proposed. In this case, the points corresponding to $P_{arc} = 35\ kW$ and $P_{arc} > 75\ kW$ have been excluded from the fit, the first one because it corresponds to a bad optics shot, the others for the reasons explained in the first scan.

Fig. 55 and Fig. 56 represent the half width at half maximum respectively along the x and y axes. The trends are the same as the previous scan and the same considerations are valid.

The comparison between the reconstructed and the electrical power is shown in Fig. 57. In this case the error in the reconstruction of the power is slightly larger than the previous case, but is still below 10%.

Another verification on the pertinence of the method results has been done by plotting the reconstructed power as a function of the electrical power for both scan. Ideally the two values coincide and they lie on the bisector of the first quadrant; in reality, it is important that the reconstructed power is not higher than the electrical one, since this would be physically impossible. Results are shown in Fig. 58. For both scans, the reconstructed

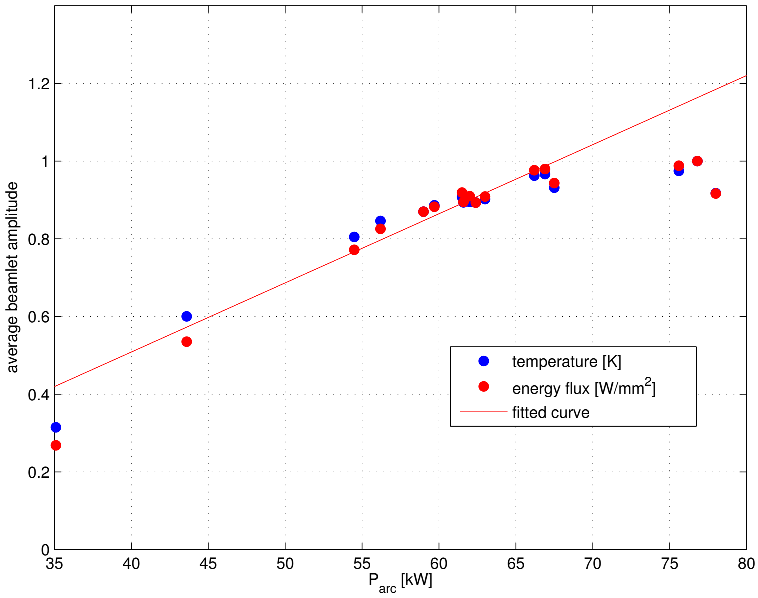

Figure 54: Average beamlet amplitude as a function of the arc power (2^{nd} scan)

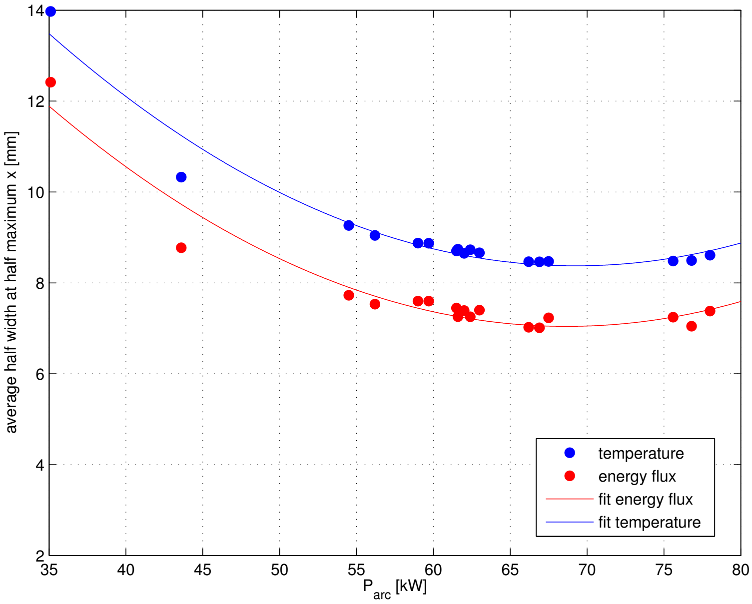

Figure 55: Average beamlet half width at half maximum x as a function of the arc power (2^{nd} scan)

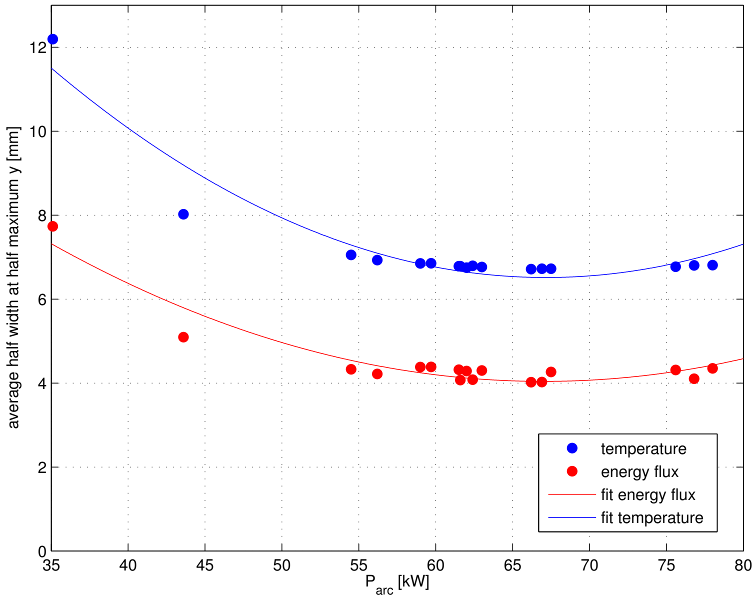

Figure 56: Average beamlet half width at half maximum y as a function of the arc power (2^{nd} scan)

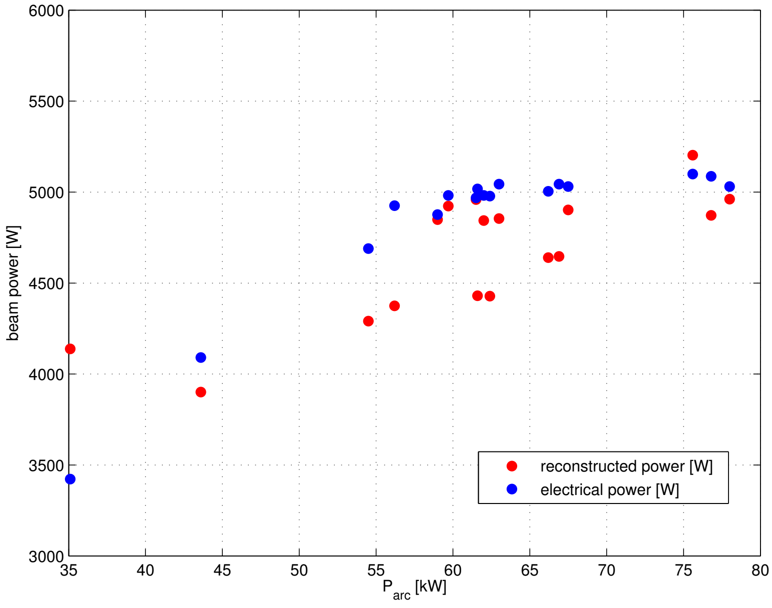

Figure 57: Comparison between the electrical power and the reconstructed power (2^{nd} scan)

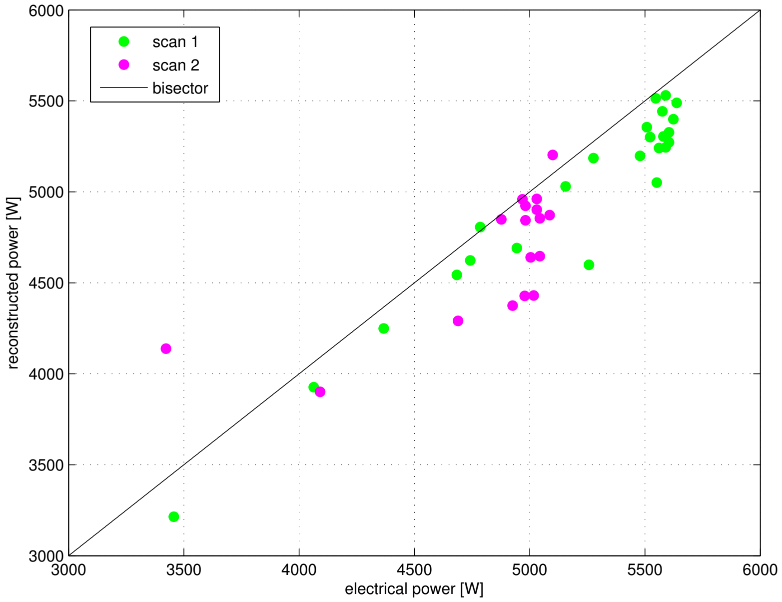

Figure 58: Reconstructed power as a function of the electrical power

power is always smaller that the electrical one, except for two points that are isolated from the others and so considered outliers.

4.3.2 Acceleration potential scan

The third and the fourth scans study the dependence of the beam characteristics on the acceleration voltage.

For the first scan, the normalized average value of the beamlet amplitude is shown in Fig. 59. The amplitude, both of the temperature and energy flux profiles, increases as long as $V_{acc} < 53\ kV$ and then it decreases. This phenomenon, as for the arc power scan, can be explained by the fact that when the acceleration voltage increases, the divergence of the beam increases too and part of the beam energy is lost on a grid.

The divergence, represented by the half width at half maximum of the beamlets, is shown in Fig. 60 and Fig. 61, respectively along x and y axes. The data set are fitted with a parabolic function, but the points corresponding to $V_{acc} > 65\ kV$ have been excluded. In fact, it can be observed from the figures that, when the acceleration potential is above this value, there is a saturation: the divergence stops increasing because the beam is hitting on one of the grids (at this point it is impossible to say which one). Contrary to the arc power scan, in this case it is possible to see the region where the divergence increases (over-perveant region), whereas, as already said, it is difficult to increase the arc power over a certain limit for technical reasons. These figures along with the amplitude one, show that the beam is first focusing (the divergence decreases while the amplitude increases) and then, as the acceleration potential increases, defocusing (the divergence rises again and the amplitude decreases).

Considering the comparison between the reconstructed and the electrical power shown in Fig. 62 it can be deduced that, for $V_{acc} > 65\ kV$, the

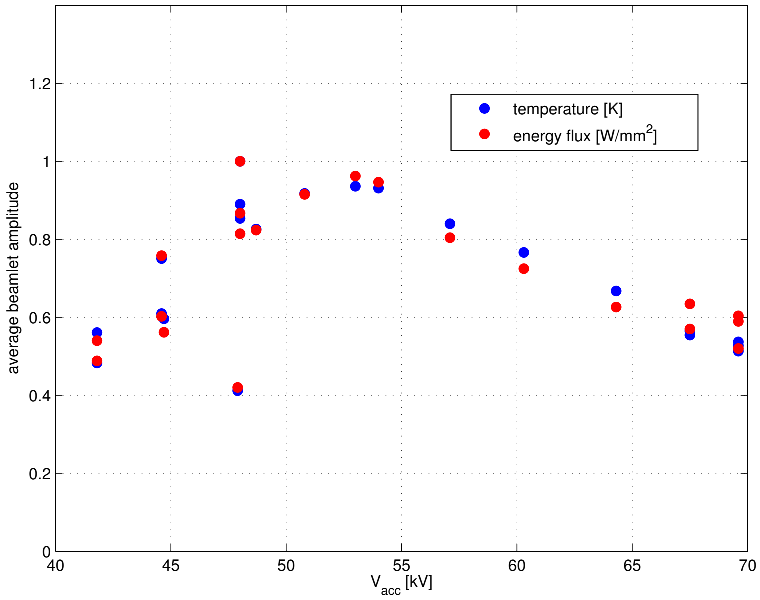

Figure 59: Average beamlet amplitude as a function of the acceleration voltage (1^{st} scan)

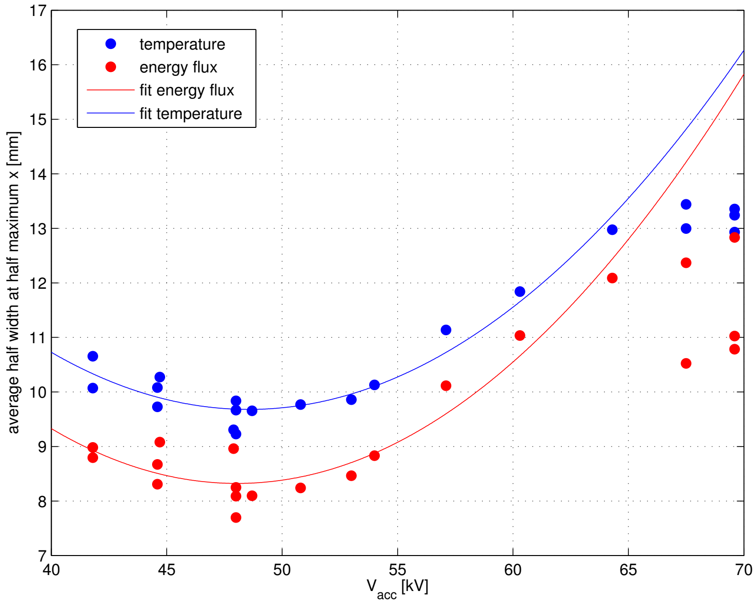

Figure 60: Average beamlet half width at half maximum x as a function of the acceleration voltage (1^{st} scan)

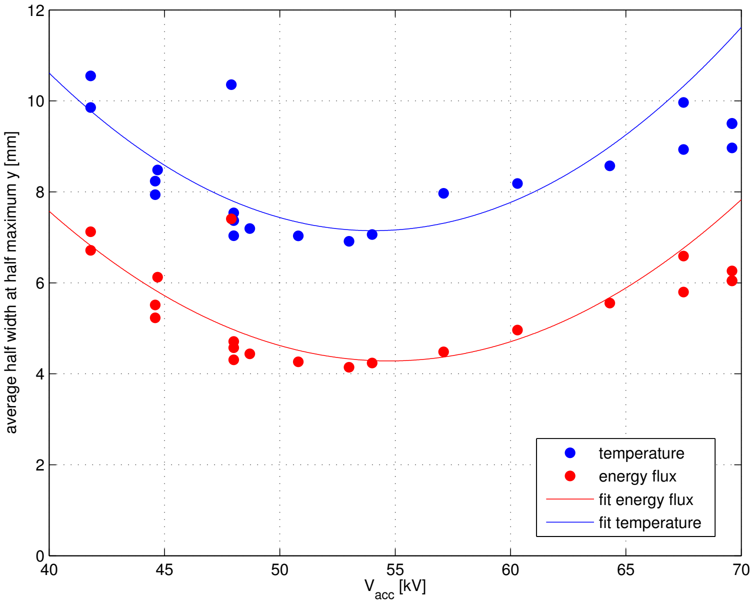

Figure 61: Average beamlet half width at half maximum y as a function of the acceleration voltage (1^{st} scan)

beam is hitting the grounded grid, in fact the power on mini-STRIKE is reaching a saturation value, while, at the same time, the electrical power is still increasing (the electrical current is going back to the power supply).

A second scan of the acceleration voltage has been analyzed. The value of the normalized average amplitude as a function of the arc power is shown in Fig. 63. The same considerations as for the previous scan can be done.

The half widths at half maximum of the beamlets are represented in Fig. 64 and Fig. 65. As for the previous scan, the values corresponding to $V_{acc} > 65\ kV$ have been excluded from the parabolic fit since, in this region, part of the beam power is lost on the GG. Again, it is possible to see the divergence increasing.

As for the previous acceleration voltage scan, from Fig. 66, it can be deduced that when $V_{acc} > 65\ kV$ the beam is intercepted by the GG, since the electrical power increase while the power that impinges on the mini-STRIKE tiles is reaching a saturation value.

As already explained for the arc power scan, the reconstructed power must be smaller that the electrical power since the contrary would be physically impossible. Fig. 67 shows that there are only two pulses for which this conditions is not verified, however they correspond to bad pulses so they can be considered as outliers.

4.3.3 Extraction potential scan

While all the previous scans were collected during the 2015 experimental campaigns, the scan of the dependence of the beam characteristics on the the extraction potential is taken from a 2014 experimental campaign.

Fig. 68 shows the average beamlet amplitude as a function of the extraction voltage. In this case, as for the acceleration voltage scans, a linear fit is not justified.

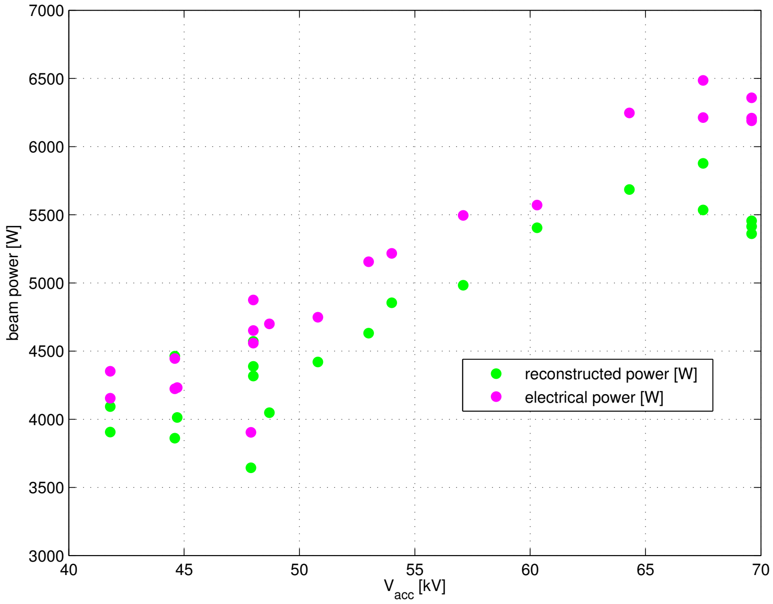

Figure 62: Comparison between the electrical power and the reconstructed power (1^{st} scan)

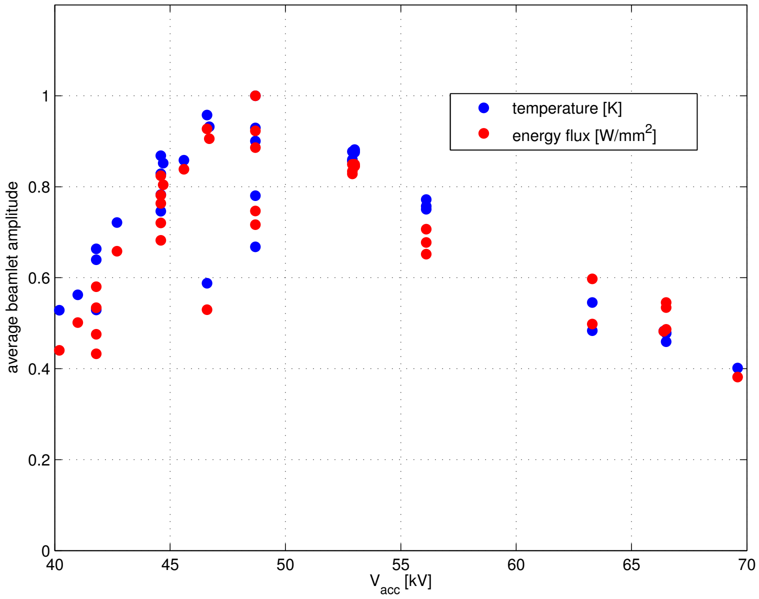

Figure 63: Average beamlet amplitude as a function of the acceleration voltage (2^{nd} scan)

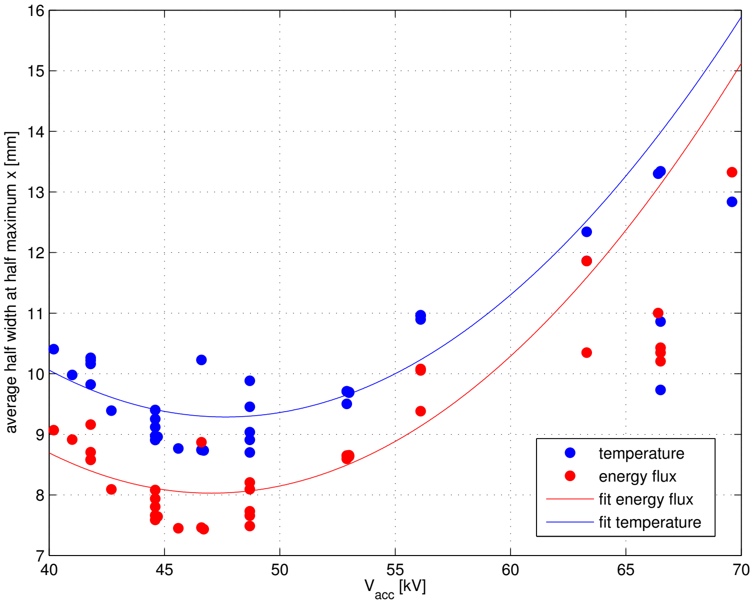

Figure 64: Average beamlet half width at half maximum x as a function of the acceleration voltage (2^{nd} scan)

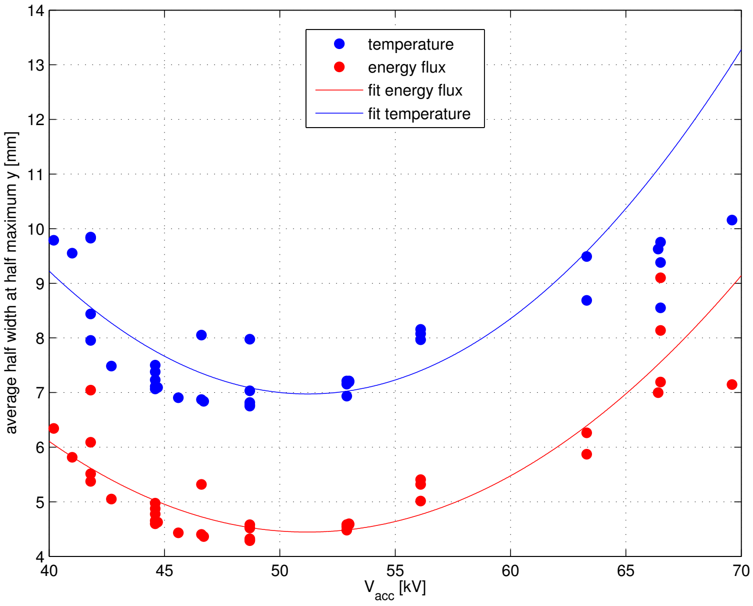

Figure 65: Average beamlet half width at half maximum y as a function of the acceleration voltage (2^{nd} scan)

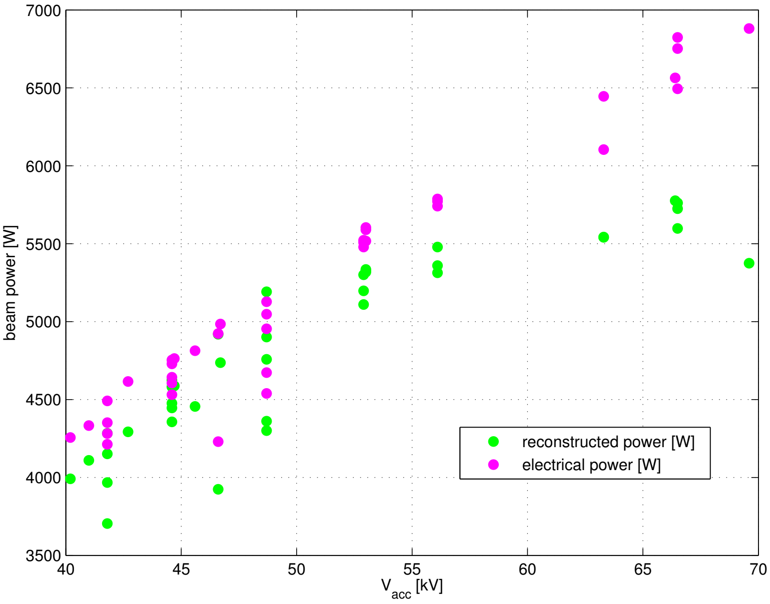

Figure 66: Comparison between the electrical power and the reconstructed power (2^{nd} scan)

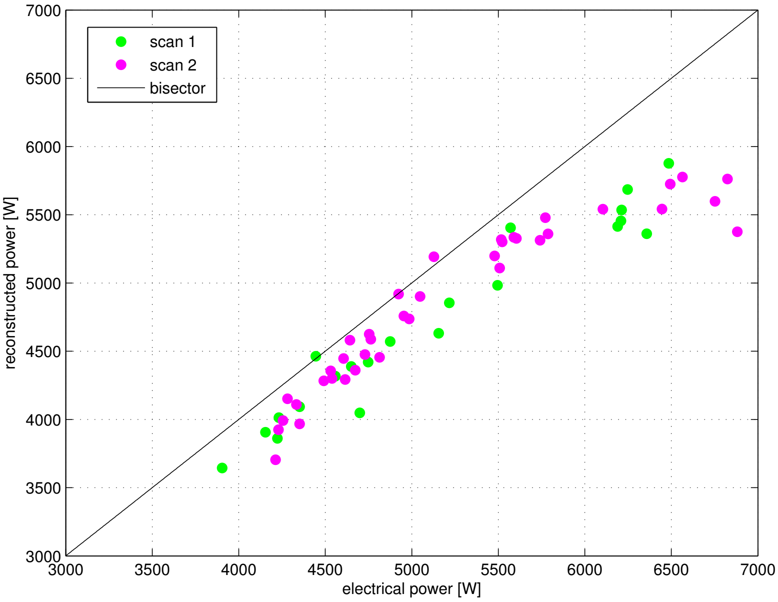

Figure 67: Reconstructed power as a function of the electrical power

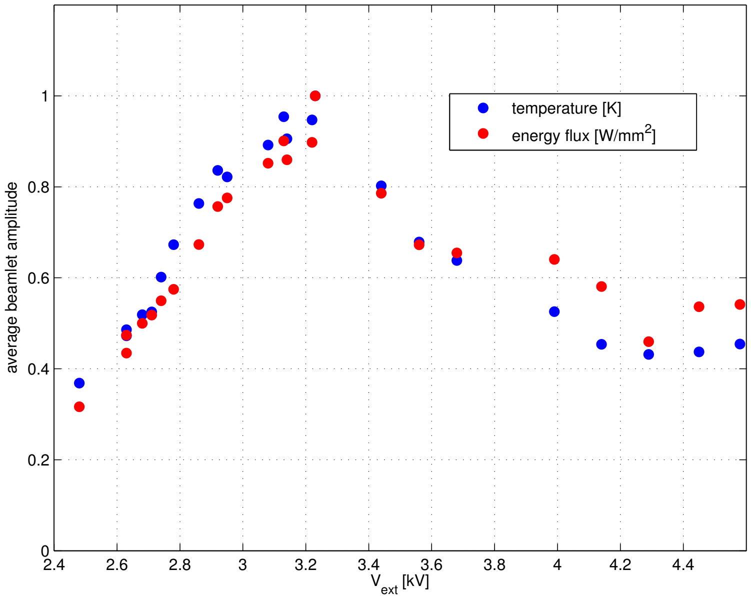

Figure 68: Average beamlet amplitude as a function of the extraction voltage

The half widths at half maximum of the beamlets are represented in Fig. 69 and Fig. 70. All the points have been retained for the parabolic fit. It can be observed that when $V_{ext} > 4.3\ kV$ the divergence stops increasing and reaches a saturation value. As for acceleration potential scan, this can be explained by the fact the beam is hitting on one of the grids, but in this case it is impossible to tell for sure which one, since for 2014 experimental campaign the current on mini-STRIKE is not known and so the comparison between the reconstructed and the electrical power can not be done. However, since the extraction potential acts on the first part of the beam trajectory it is most likely to be the EG. Contrary to the arc power scan, it is possible to see the over-perveant region.

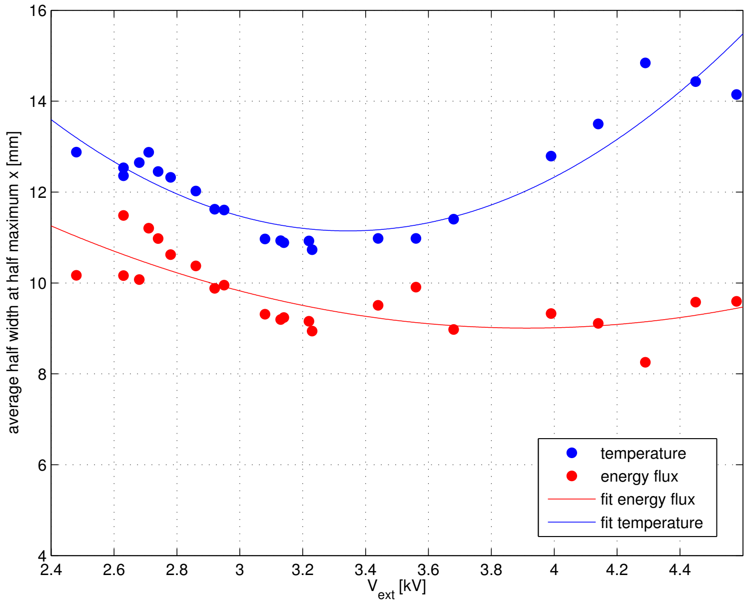

Figure 69: Average beamlet half width at half maximum x as a function of the extraction voltage

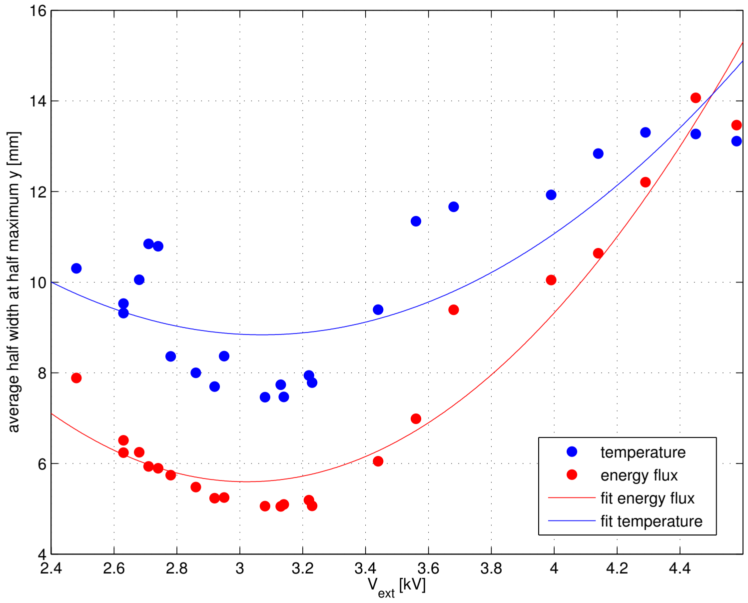

Figure 70: Average beamlet half width at half maximum y as a function of the extraction voltage

5 CONCLUSIONS

The ITER tokamak is an international project, with the aim of proving the possibility to produce energy by nuclear fusion of deuterium and tritium nuclei in a reactor scale. In order to reach the necessary temperature for fusion, additional heating systems are required, like the injection of a neutral beam.

To verify the ITER NBI reliability, the PRIMA test facility is under construction at Consorzio RFX (Padova) in the CNR research area; it includes the full power injector MITICA and the negative ion source SPIDER. To study the ion beam characteristics, the movable diagnostic calorimeter STRIKE has been developed. It is composed by 2 panels of 8 tiles each, made of one-directional Carbon Fibre Composite (CFC). The heat produced by the beam impinging perpendicularly on the front side is promptly transmitted to the other side of the tile and the thermal emission is captured by two thermal cameras.

A small scale version of STRIKE (mini-STRIKE) has been employed to investigate the properties of the negative ion beam test stand of the neutral beam injectors of the LHD experiment (NIFS). The thermal camera images of the tiles temperature profiles represent the experimental data analyzed in this thesis.

The aim of the method presented is to reconstruct the energy flux profile impinging on the front side of the tile that produced the given temperature profile recorded by the thermal camera. This method is based on the transfer function and lies on the assumptions that the material is linear and the effect of radiation can be neglected. The impulse response of the tile is obtained from laser simulations.

The method has been tested using simulated data and it demonstrated to be able to reconstruct the energy flux profile with an error less than 10%. Subsequently, it has been optimized for the experimental data. One of the major issues concerned the choice of the optimal low-pass filter; the latter is necessary to limit the high frequencies and noise that would have hidden the relevant information. The reduction of the influence of the non linearity of the material represented the other major issue and finally led to compute the anti-transfer function using the specific internal energy instead of the temperature.

The experimental campaign of the NIFS experiment has then been analyzed to investigate the beam characteristics as a function of the ion source electrical parameters, such as the arc power P_{arc}, the acceleration potential V_{acc} and the extraction power V_{ext}.

The results are consistent with what is expected from the beam physic theory, in terms of amplitude and divergence of the beamlets.

Finally, it can be said that the method represents a good analysis tool, capable of reconstructing the energy flux profile impinging on the front side of the tile with an error of about 10%.

5.1 FUTURE DEVELOPMENTS

The method based on the transfer function using via Fourier Transform assumes the linearity of the system; it is not a causal model and considering only the impulsive response. One of the major goal is to remove this restrictions to take into account the non linearity of the system and to include time into the analysis.

An attempt has been carried out using the Hilbert-Huang transform (see Appendix A), a new method that can handle nonstationary and nonlinear signals, however it need to be investigated deeply since it has not led to a final conclusion.

A HILBERT-HUANG METHOD

An attempt to go beyond the hypothesis of linearity and stationarity at the basis of the method of the Fourier transfer function has been made considering the Hilbert-Huang transform (HHT).

HHT is truly a time-frequency analysis, but it does not require an a priori functional basis and, therefore, the convolution computation of frequency. It is capable of extracting the frequency components from possibly nonlinear and nonstationary intermittent signals.

A.1 INTRODUCTION TO THE METHOD

Traditional data-analysis methods are all based on linear and stationary assumptions. Unfortunately, in most real systems, either natural or even man-made ones, the data are most likely to be both nonlinear and nonstationary. A necessary condition to represent nonlinear and nonstationary data is to have an adaptive basis. An a priori defined function cannot be relied on as a basis, no matter how sophisticated the basis function might be. For nonstationary and nonlinear data, where adaptation is absolutely necessary, no available methods can be found.

The HHT consists of two parts: empirical mode decomposition (EMD) and Hilbert spectral analysis (HSA). This method is potentially viable for nonlinear and nonstationary data analysis, especially for time-frequency-energy representations. It has been tested and validated exhaustively, but only empirically [15].

A.2 THE HILBERT-HUANG TRANSFORM

The development of the HHT was motivated by the need to describe nonlinear distorted waves in detail, along with the variations of these signals that naturally occur in nonstationary processes. The available methods are either for linear but nonstationary, or nonlinear but stationary and statistically deterministic processes and imposing a linear structure on a nonlinear system is just not adequate. Other than periodicity, the detailed dynamics in the processes needs to be determined from the data because one of the typical characteristics of nonlinear processes is their intra-wave frequency modulation, which indicates the instantaneous frequency changes within one oscillation cycle [15]. This intra-frequency frequency variation is the hallmark of nonlinear systems. When the analysis is based on the linear Fourier analysis, this intra-wave frequency variation could not be depicted, except by resorting to harmonics. Thus, any nonlinear distorted waveform has been referred to as "harmonic distortions". Harmonic distortions are a mathematical artifact resulting from imposing a linear structure on a nonlinear system. They may have mathematical meaning, but not a physical meaning. For example, in the case of water waves, such harmonic components do not have any of the real physical characteristics of a real wave. The physically meaningful way to describe the system is in terms of the instantaneous frequency, which will reveal the intra-wave frequency modulations [15].

The easiest way to compute the instantaneous frequency is by using the Hilbert transform, through which the complex conjugate $y(t)$ of any real valued function $x(t)$ of L^p class can be determined by [15]:

$$\mathcal{H}[x(t)] = \frac{1}{\pi}\mathrm{PV}\int_{-\infty}^{+\infty}\frac{x(\tau)}{t-\tau}\mathrm{d}\tau \qquad \text{(A.1)}$$

in which the PV indicates the principal value of the singular integral. With the Hilbert transform, the analytic signal is defined as:

$$z(t) = x(t) + iy(t) = a(t)e^{i\theta(t)} \ , \qquad \text{(A.2)}$$

where

$$a(t) = \sqrt{x^2 + y^2} \ , \qquad \theta(t) = \arctan\left(\frac{y}{x}\right) \ . \qquad \text{(A.3)}$$

Here, $a(t)$ is the instantaneous amplitude, and θ is the phase function, and the instantaneous frequency is simply

$$\omega = \frac{d\theta}{dt} \qquad \text{(A.4)}$$

A.3 THE EMPIRICAL MODE DECOMPOSITION

The empirical mode decomposition method is necessary to deal with data from nonstationary and nonlinear processes. In contrast to almost all of the previous methods, this new method is adaptive, with an *a posteriori*-defined basis, from the decomposition methods, based on and derived from the data. The decomposition is based on simple assumption that any data consists of different simple intrinsic modes of oscillations. Each intrinsic mode, linear or nonlinear, represents a simple oscillation, which will have the same number of extrema and zero-crossings. Furthermore, the oscillation will also be symmetric with respect to the "local mean". At any given time, the data may have many different coexisting modes of oscillation, one superimposing on the others. The result is the final complicated data. Each of these oscillatory modes is represented by an intrinsic mode function (IMF) with the following definition:

1. in the whole dataset, the number of extrema and the number of zero-crossings must either equal or differ at most by one, and
2. at any point, the mean value of the envelope defined by the local maxima and the envelope defined by the local minima is zero.

An IMF represents a simple oscillatory mode as a counterpart to the simple harmonic function, but it is much more general: instead of constant amplitude and frequency, as in a simple harmonic component, the IMF can have a variable amplitude and frequency as functions of time. With the above definition for the IMF, one can then decompose any function as follows: take the test data as given in Fig. 71; identify all the local extrema, then connect all the local maxima by a cubic spline line as shown in the upper envelope. Repeat the procedure for the local minima to produce the

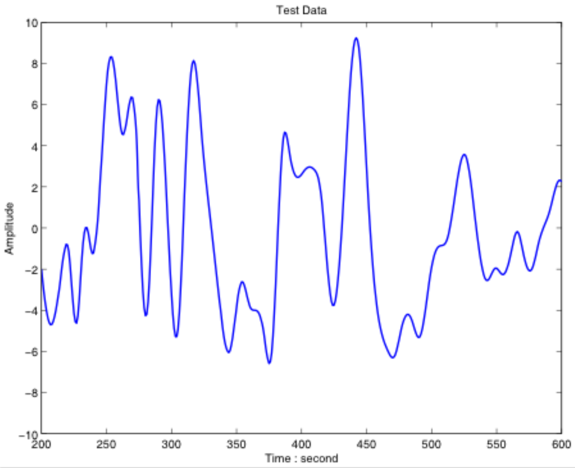

Figure 71: The test data

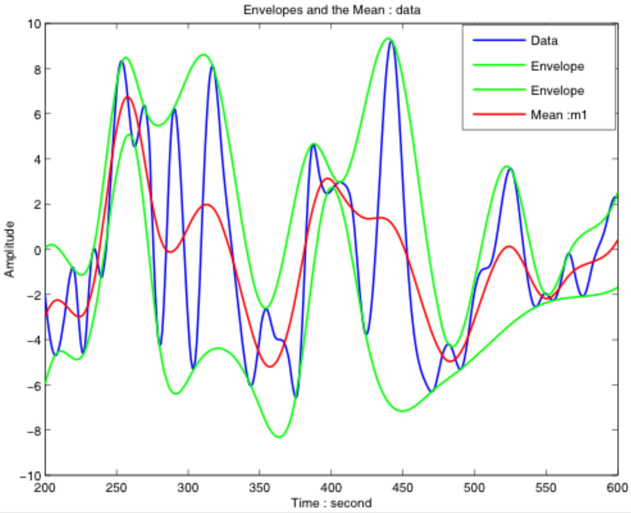

Figure 72: The data (blue) upper and lower envelopes (green) defined by the local maxima and minima, respectively, and the mean value of the upper and lower envelopes given in red

lower envelope. The upper and lower envelopes should cover all the data between them, as shown in Fig. 72. Their mean is designated as m_1, also shown in Fig. 72, and the difference between the data and m_1 is the first component h_1 shown in Fig. 73, i. e.,

$$h_1 = x(t) - m_1 \ . \tag{A.5}$$

Ideally, h_1 should satisfy the definition of an IMF, for the construction of h_1 described above should have made it symmetric and have all maxima positive and all minima negative. However, even if the fitting is perfect, a gentle hump on a slope can be amplified to become a local extremum in changing the local zero from a rectangular to a curvilinear coordinate system. After the first round of sifting, the hump may become a local maximum. New extrema generated in this way actually reveal the proper modes lost in the initial examination. In fact, with repeated siftings, the sifting process can recover signals representing low-amplitude riding waves [15].

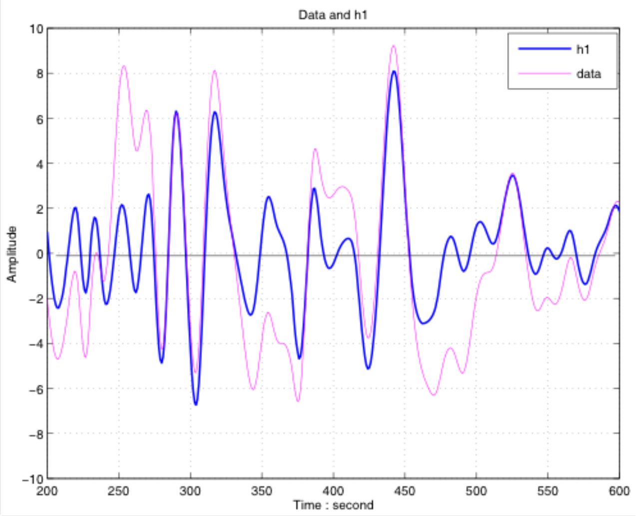

Figure 73: The data (magenta) and h_1 (blue)

The sifting process serves two purposes: to eliminate riding waves, and to make the wave profiles more symmetric. While the first purpose must be achieved for the Hilbert transform to give a meaningful instantaneous frequency, the second purpose must also be achieved in case the neighboring wave amplitudes have too large a disparity. Toward these ends, the sifting process has to be repeated as many times as is required to reduce the extracted signal to an IMF. In the subsequent sifting processes, h_1 can be treated only as a proto-IMF. In the next step, it is treated as the data; then,

$$h_{11} = h_1 - m_{11} \ . \tag{A.6}$$

After repeated siftings in this manner, shown in Fig. 74a and 74b, up to k times, h_{1k} becomes an IMF; that is,

$$h_{1k} = h_{1(k-1)} - m_{1k} \ ; \tag{A.7}$$

then, it is designated as

$$c_1 = h_{1k} \ , \tag{A.8}$$

the first IMF component from the data shown in Fig. 75. Here, a critical decision must be made: the stoppage criterion. Historically, two different criteria have been used [15]. The first one is determined by using a Cauchy type of convergence test. Specifically, the test requires the normalized squared difference between two successive sifting operations defined as

$$SD_k = \frac{\sum_{t=0}^{T} \|h_{k-1}(t) - h_k(t)\|^2}{\sum_{t=0}^{T} h_{k-1}^2} \tag{A.9}$$

to be small. If this squared difference SD_k is smaller than a predetermined value, the sifting process will be stopped. This definition seems to be rigorous, but is is very difficult to implement in practice. There are two critical issues: first, the question of how small is small enough needs an answer. Second, this criterion does not depend on the definition of the IMFs. The squared difference might be small, but nothing guarantees that the function will have the same numbers of zero-crossings and extrema, for example. For these reasons, the second criterion has been proposed. It is based on the

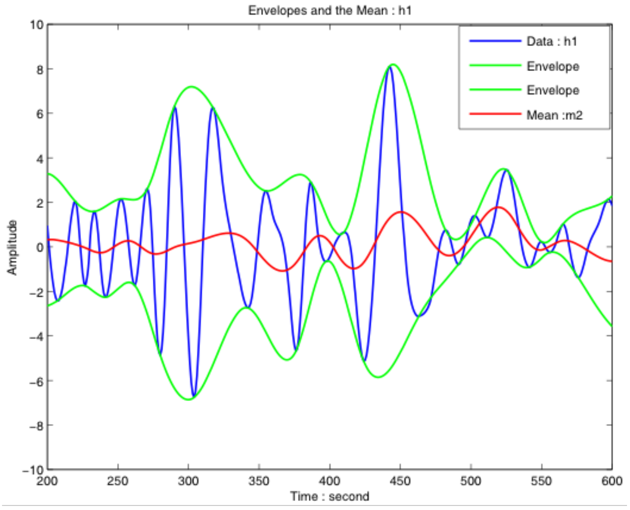

(a) Repeated sifting steps with h_1 and m_2

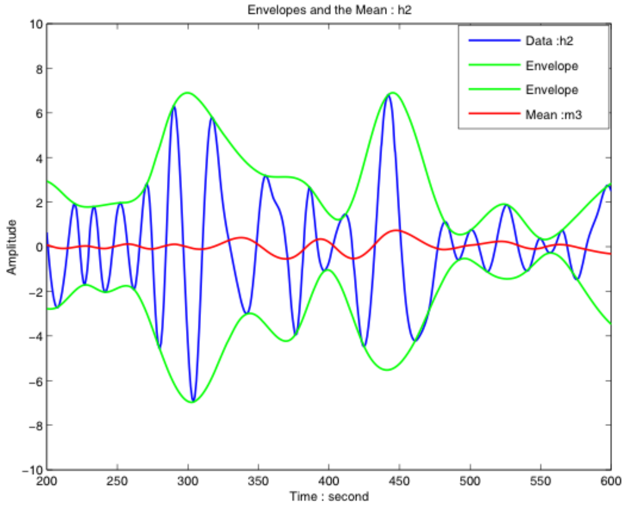

(b) Repeated sifting steps with h_2 and m_3

Figure 74: Repeated sifting steps

agreement of the number of zero-crossings and extrema. The sifting process will stop only when the number of zero-crossing and extrema stay the same and are equal or differ at most by one [15].

Now assume that a stoppage criterion was selected, and that the first IMF c_1 was found. Overall, c_1 should contain the finest scale or the shortest period component of the signal. It follows that c_1 can be separated from the rest of the data by

$$r_1 = x(t) - c_1 \tag{A.10}$$

Since the residue r1 still contains longer period variations in the data, as shown in Fig. 76, it is treated as the new data and subjected to the same sifting process as described above. This procedure can be repeated with all the subsequent r_j's. The sifting process can be stopped finally by any of the following predetermined criteria: either when the component c_n or the residue r_n becomes so small that it is less than the predetermined value of substantial consequence, or when the residue r_n becomes a monotonic function from which no more IMFs can be extracted. Even for data with

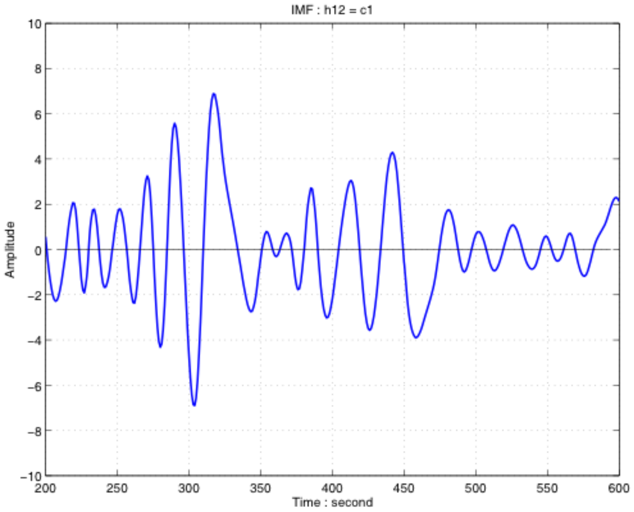

Figure 75: The first IMF component c_1 after 12 steps

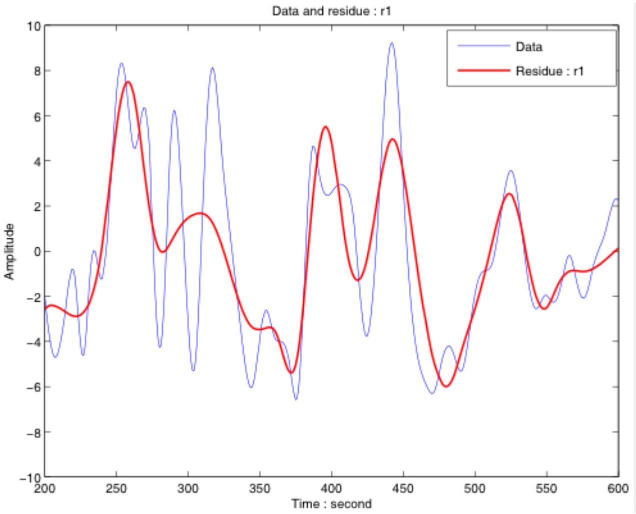

Figure 76: The original data (blue) and the residue r_1

zero mean, the final residue still can be different from zero. It is finally obtained:

$$x(t) = \sum_{j=1}^{n} c_j + r_n \; . \tag{A.11}$$

Thus, a decomposition of the data into n-empirical modes is achieved, and a residue r_n obtained which can be either the mean trend or a constant. The EMD technique needs only the locations of the local extrema. The zero reference for each component will be generated by the sifting process.

The components of the EMD are usually physically meaningful, for the characteristic scales are defined by the physical data [15].

A.4 APPLICATION TO THE EXPERIMENTAL DATA

In order to overcome the problems dues to the non linearity and non stationarity of the particle beam, an attempt to apply the HHT method to the experimental data has been done with an approach similar to the FFT. However, several problems have been encountered.

First of all, there are several types of decomposition (see [15] for details), most of which are for mono-dimensional signals. Dealing with images (the thermal camera images) requires a 2D sifting process on. Among the 2D decomposition algorithms the majority are pseudo-2D: they perform the decomposition by row or by column and not on the whole image. Finally a pure Bi-dimensional Empirical Mode Decomposition (BEMD) has been applied. This decomposes the image in 4 components, the first one corresponding the the highest frequencies (in most of the cases noise). This implies that the BEMD can be used as a filter or for removing the thermocouple shadow on the images. Consider Fig. 77: in Fig.77a there is the original image with the thermocouple shadow on the upper left part; Figs. 77c,77d,77e,77f show the 4 components of the decomposition (it can be noticed how the first component is constituted mostly by the points of the thermocouple), Fig. 77b shows the resulting image after removing the first decomposition component. It can be noticed that the thermocouple, even if non perfectly, has been removed. This could be an easy and fast way to prepare the images before the analysis.

Secondly, an approach like the one used for the FFT requires that the signals involved have the same basis system and, as explained in section A.1, this is not the case of HHT since it creates a different basis system for every signal, based on the signal itself. An attempt to overcome this problem has been done trying to project the basis systems of the signals on a common system, but the BEMD fails in decomposing the two signals of the impulse response (F_0 and T_0). In fact, since F_0 and T_0 are composed, respectively, by a single gaussian function and a single hubbert function, the upper envelope coincide with the lower one and so they cancel each other.

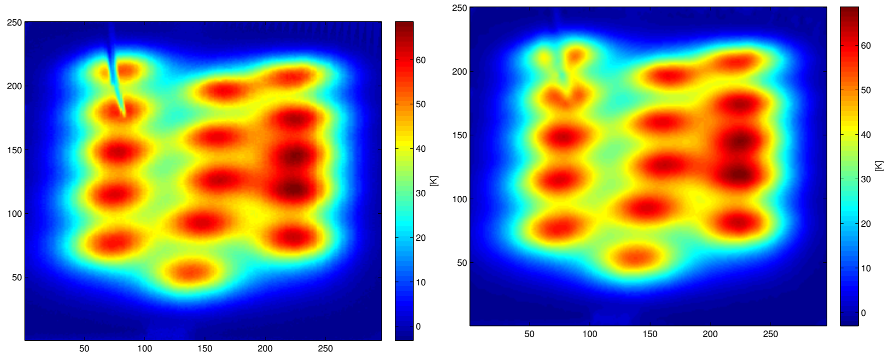

(a) Original image

(b) Resulting image after removing the first component

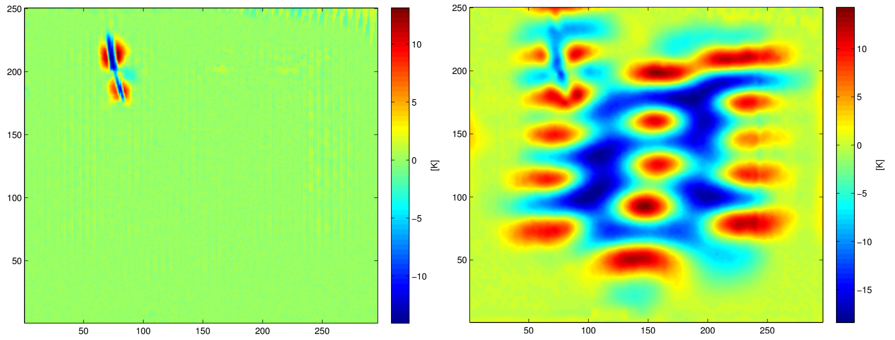

(c) BEMD 1^{st} component

(d) RBEMD 2^{nd} component

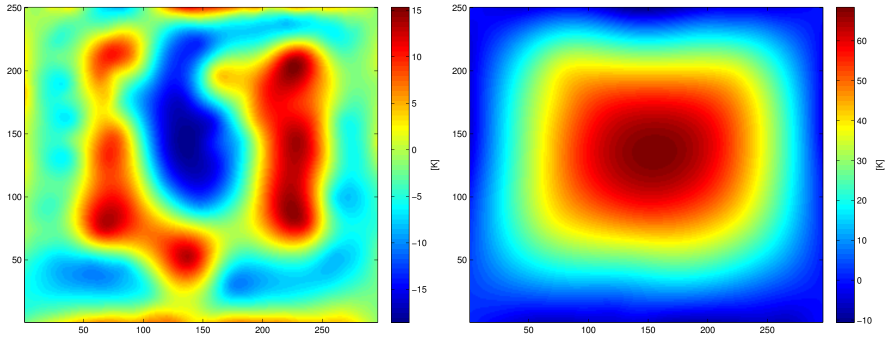

(e) BEMD 3^{rd} component

(f) RBEMD 4^{th} component

Figure 77: Bi-dimensional Empirical Mode Decomposition

BIBLIOGRAPHY

[1] Isaac Amidror. *Mastering the Discrete Fourier Transform in One, Two or Several Dimensions*. Springer, 2013.

[2] V. Antoni et al. "Design, installation, commissioning and operation of a beamlet monitor in the negative ion beam test stand at NIFS". In: *AIP Conf. Proc.* 1655 (2015).

[3] I. G. Brown. *The Physics and Technology of Ion Sources, Second Edition*. Verlag GmbH, 2003.

[4] H. S. Carslaw and J. C. Jaeger. *Conduction of heat in solids (second edition)*. Clarendon Press, 1959.

[5] D. Ciric et al. "Beam profiles measurements using a unidirectional CFC-target and infrared imaging". In: *Fusion Technology* (1994), pp. 827–830.

[6] *COMSOL official website*. URL: www.comsol.it.

[7] Sofia Cristofaro. "Characterization of the BATMAN beam properties by H_α-Doppler shift spectroscopy and mini-STRIKE calorimeter". MA thesis. Università degli Studi di Padova, 2014.

[8] M. Dalla Palma et al. "Numerical assessment of the diagnostic capabilities of the instrumented calorimeter for SPIDER (STRIKE)". In: *AIP Conf. Proc.* Vol. 1390. 2011, pp. 584–593.

[9] Michela De Muri et al. "Prototype of a Diagnostic Calorimeter for BATMAN: Design and Preliminary Measurements". In: *IEEE Transactions on Plasma Science* 42 (2014), pp. 1032–1035.

[10] M. De Muri et al. "Characterization, test and interpretative simulations of one-dimensional Carbon Fiber Composite prototype for SPIDER experiment". In: *Fusion Engineering and DesignDesign* 88 (2013), pp. 1758–1763.

[11] M. De Muri et al. "Design and specifications of the diagnostics for the instrumented calorimeter of Source for the Production of Ions of Deuterium Extracted from Radio frequency plasmaa)". In: *Review of Scientific Instruments* 83 (2012).

[12] H.P.L. de Esch et al. "The optimization of neutral beams for ignition and burn control on next-step reactors". In: *Fusion Engineering and Design* 26 (1995).

[13] Jeffrey P. Freidberg. *Plasma Physics and Fusion Energy*. Cambridge University Press, 2007.

[14] R.S. Hemsworth and Takashi Inoue. "Positive and negative ion sources for magnetic fusion". In: *IEEE Transactions on Plasma Science* 33 (2005), pp. 1799–1813.

[15] N.E. Huang and S.S. Shen. *Hilbert-Huang Transform and Its Applications*. World Scientific, 2005.

[16] *ITER official website*. URL: www.iter.org.

[17] *Japan Atomic Energy Agency official website*. URL: www.jaea.go.jp.

[18] M. Kikuchi, K. Lackner, and M. Q. Tran. *Fusion Physics*. International Atomic Energy Agency, 2012.

[19] J. D. Lawson. "Perveance and the Bennett Pinch Relation in Partially-Neutralized Electron Beams". In: *Journal of Electronics and Control* 5 (1958), pp. 146–151.

[20] Andrea Rizzolo et al. "Design and analyses of a one-dimensional CFC calorimeter for SPIDER beam characterisation". In: *Fusion Engineering and Design* 85 (2010), p. 2268.

[21] Gianluigi Serianni et al. "Thermal simulations of STRIKE tiles for the assessment of the CFC prototypes and of the configuration for SPIDER". In: *American Institute of Physics Conference Series*. Vol. 1515. 579-586. 2013.

[22] G. Serianni et al. *Mini-STRIKE test in LHD NBI test stand: installation and operating instructions*. Tech. rep. RFX SPIDER TN 333, 2014.

[23] G. Serianni et al. "Thermal and electrostatic simulations of the diagnostic calorimeter for the Source for Production of Ion of Deuterium Extracted from RF plasma beama)". In: *Review of Scientific Instruments* (2012).

[24] P. Sonato et al. "The {ITER} full size plasma source device design". In: *Fusion Engineering and Design* (2009). Proceeding of the 25th Symposium on Fusion Technology(SOFT-25), pp. 269–274.

[25] L. Svensson et al. *SRD-53-PR, -MI, -MP, -SI, -SP (NEUTRAL BEAM TEST FACILITY)*. Tech. rep. Iter, 2009.

[26] V. Toigo et al. "Progress in the realization of the PRIMA neutral beam test facility". In: *Nuclear Fusion* (2015).

[27] Katsuyoshi Tsumori et al. "Correction of Beam Distortion in Negative Hydrogen Ion Source with Multi-Slot Grounded Grid". In: *AIP Conf. Proc.* 763 (2005), pp. 35–46.

[28] K Tsumori et al. "Beamlet characteristics in the accelerator with multislot grounded grid." In: *Rev Sci Instrum* 81 (2010).

[29] K. Tsumori et al. "High power beam injection using an improved negative ion source for the large helical device". In: *Review of Scientific Instruments* 75 (2004), pp. 1847–1850.